

# **The Dynamics and Kinematics of Coronal Mass Ejections and Shock Waves**

A dissertation submitted to the University of Dublin  
for the degree of *Philosophiae Doctor (PhD)*

**Eoin P. Carley**  
**Trinity College Dublin, September 2013**

---

SCHOOL OF PHYSICS  
UNIVERSITY OF DUBLIN  
TRINITY COLLEGE



## **Declaration**

I declare that this thesis has not been submitted as an exercise for a degree at this or any other university and it is entirely my own work.

I agree to deposit this thesis in the University's open access institutional repository or allow the library to do so on my behalf, subject to Irish Copyright Legislation and Trinity College Library conditions of use and acknowledgement.

**Name:** Eoin Carley

**Signature:** ..... **Date:** .....



## Summary

Coronal mass ejections (CMEs) are large-scale eruptions of magnetized plasma from the low solar atmosphere into interplanetary space. With energies of up to  $10^{25}$  J, they are the most energetic eruptive phenomena in the solar system and are also the driver of plasma shocks from the corona into the heliosphere. Despite many years of study, the nature of the forces governing their eruption, and the kinematical behavior of the resulting shock, remain poorly understood. In this thesis I will present the first accurate calculation of the magnitude of the total force on a CME. I will also present previously unobserved plasma shock behavior that sheds new light into the kinematical nature of CME-driven shocks in the corona.

In the past, measurement of the forces governing the propagation of CMEs have been hindered by highly uncertain estimates of the total mass of the ejection. The primary source of uncertainty is the unknown position and geometry of the CME, leading to an erroneous treatment of the Thomson scattering equations which are used to estimate the mass. Geometrical uncertainty on the CMEs position and size has primarily been due to observations of the eruption from a single vantage point. However, with the launch of the *Solar Terrestrial Relations Observatory (STEREO)*, the two viewpoints can be exploited to derive the CMEs position and size, ultimately resulting in mass uncertainty that is both reliably quantified and much reduced. Using the *STEREO* spacecraft, a CME on the 12 December 2008 was found to have a mass of  $3.4 \pm 1.0 \times 10^{12}$  kg, meaning the mass uncertainty was less than 30%. This is a substantial improvement on

previous uncertainties which were well above 50%, or entirely unquantifiable. The much better mass estimates can then be combined with kinematical results that are also more reliable and hence lead to the first reliable quantification of the total force acting on the CME. The dynamics are described by an early phase of strong acceleration, dominated by a force of peak magnitude of  $3.4 \pm 2.2 \times 10^{14}$  N at  $\sim 3 R_\odot$ . Using the magnetohydrodynamics (MHD) equation of motion, the relative sizes of the forces at each stage in the CME propagation are estimated, revealing the Lorentz force is the largest source of CME acceleration early in its propagation. Quantification of the Lorentz force magnitude from observations has never been achieved in the past.

The second part of this thesis will involve an investigation into the behaviour of radio-bright plasma shocks occurring in the corona. CMEs often erupt at speeds in excess of the local magnetosonic wave speeds in the corona. Traveling in excess of Alfvén Mach 1, they often drive shocks which can have a variety of observational manifestations, such as type II and III radio bursts, coronal bright fronts (CBFs), white-light enhancements, and the eventual in-situ detection of solar energetic particles. Despite such a variety of shock phenomena being observed for decades, the unifying physical mechanism between these phenomena remains unknown. This thesis will provide an analysis that uses extreme ultraviolet, radio, and white-light imaging of a solar eruptive event on 22 September 2011 to determine the properties of a CME-driven shock in the corona. The results show that a plasma shock with an Alfvén Mach number of  $2.4_{-0.8}^{+0.7}$  was coincident with a coronal bright front and an intense decametric radio burst generated by electrons with kinetic energies of 2-46 keV (0.1-0.4 c). This work provides new observational evidence to show that the relationship between CMEs, CBFs, and type II and III radio bursts is a coronal plasma shock.

*For my parents.*

## Acknowledgements

A huge thank you to Peter Gallagher. Your guidance, advice and support have never steered me wrong, and your enthusiasm for this subject has been a huge source of inspiration. It has been a pleasure working with you over the last four years.

Secondly, I would like to thank James McAteer for his help at the beginning of my research and getting me off to a great start. To Shaun Bloomfield and David Pérez-Suárez, thank you for all your useful discussions and help from the beginning.

Thank you to Pietro Zucca and Joe McCauley. Those dedicated days in rainy Birr got us a long way.

Most importantly, Peadar, Bridget and Lisa. I couldn't have done this without your love and support. I'd be nowhere without you. To Mags and all my friends, thank you all for such good times throughout the years.

Of course, to all the people of the Astrophysics Research Group, past and present. Thank you for all the laughs and being friends from the start. And finally, shout out to Pythagoras, changed the game.

# List of Publications

1. **Carley, E. P.**, Long, D. M., Byrne P. J., Zucca, P., Bloomfield D. S., McCauley J., & Gallagher, P. T.  
“Quasiperiodic Acceleration of Electrons by a Plasmoid Driven Shock in the Solar Atmosphere”,  
*Nature Physics*, in press, (2013).
2. **Carley, E. P.**, MacAteer, R. T. J., & Gallagher, P. T.  
“Coronal Mass Ejection Masses, Energies, and Force Estimates Using STEREO”,  
*The Astrophysical Journal*, Volume 752, Issue 1, article id. 36, 8 pp. (2012).
3. Zucca, P., **Carley, E. P.**, McCauley, J., Gallagher, P. T., Monstein, C., & MacAteer, R. T. J.,  
“Observations of Low Frequency Solar Radio Bursts from the Rosse Solar-Terrestrial Observatory”,  
*Solar Physics*, Volume 280, Issue 2, pp.591-602. (2012).
4. Zucca, P., **Carley, E. P.**, Bloomfield, S. D., & Gallagher, P. T.  
“The formation heights of coronal shocks from 2D density and Alfvén speed maps”,  
*Astronomy & Astrophysics*, submitted.
5. Bloomfield, S. D., **Carley, E. P.**, et al.  
“A Comprehensive Overview of the 2011 June 7 Solar Storm”,  
*Astronomy & Astrophysics*, in review.
6. Morosan, D. E., Zucca, P., Fallows, R., **Carley, E. P.**, & Gallagher, P. T.  
“The Non-flaring Sun at Low Frequencies with LOFAR”,  
*Astronomy & Astrophysics*, in prep.

- 
7. Bisi, M. M., Hardwick, S. A., Fallows, R. A., Davies, J. A., Harrison, R. A., Jensen, E. A., Morgan, H., Wu, C. C., Asgekar, A., Xiong, M., **Carley, E. P.**

“The first coronal mass ejection observed with the Low Frequency Array (LOFAR)”,

*The Astrophysical Journal Supplements*, in review.

# Contents

<b>List of Publications</b>	vii
<b>List of Figures</b>	xiii
<b>1 Introduction</b>	1
1.1 The Sun . . . . .	2
1.1.1 Solar Interior . . . . .	3
1.1.2 Solar Magnetic Field and Dynamo . . . . .	7
1.1.3 Solar Atmosphere . . . . .	10
1.1.3.1 Photosphere . . . . .	10
1.1.3.2 Chromosphere . . . . .	12
1.1.3.3 Transition Region . . . . .	14
1.1.3.4 Corona . . . . .	14
1.2 Coronal Mass Ejections . . . . .	18
1.2.1 A Brief History . . . . .	19
1.2.2 Morphology and Kinematics . . . . .	21
1.2.3 Masses and Dynamics . . . . .	26
1.3 Coronal Shocks . . . . .	36
1.3.1 Type II Radio Bursts . . . . .	36
1.3.2 Herringbones and Type IIIIs . . . . .	43
1.3.3 Coronal Bright Fronts . . . . .	45
1.3.4 White-light Shocks . . . . .	49
1.4 Thesis Outline . . . . .	51

---

## CONTENTS

<b>2 Coronal Mass Ejection and Plasma Shock Theory</b>	<b>53</b>
2.1 Plasma Physics and Magnetohydrodynamics . . . . .	54
2.1.1 Maxwell's Equations . . . . .	54
2.1.2 Plasma Kinetic Theory . . . . .	55
2.1.3 Magnetohydrodynamics . . . . .	58
2.1.4 Magnetic Reconnection . . . . .	61
2.2 Coronal Mass Ejections . . . . .	65
2.2.1 Catastrophe Model . . . . .	66
2.2.2 Magnetic Breakout Model . . . . .	69
2.2.3 Toroidal Instability . . . . .	71
2.3 Coronal Shocks and Plasma Emission . . . . .	74
2.3.1 Alfvén Speed in the Corona . . . . .	74
2.3.2 MHD Shocks . . . . .	76
2.3.3 Shock Drift Acceleration . . . . .	81
2.3.4 Wave-Particle Interaction . . . . .	85
2.3.5 Three-Wave Interaction and Plasma Emission . . . . .	89
2.3.6 Frequency Drift of Radio Bursts . . . . .	94
<b>3 Observation and Instrumentation</b>	<b>98</b>
3.1 White-Light Observations . . . . .	99
3.1.1 Lyot Coronagraph . . . . .	101
3.1.1.1 SOHO LASCO . . . . .	102
3.1.1.2 STEREO COR1 and COR2 . . . . .	106
3.1.1.3 Whilte-light Image Data Reduction . . . . .	111
3.2 Ultraviolet Observations . . . . .	114
3.2.1 The Atmospheric Imaging Assembly . . . . .	114
3.3 Radio Observations . . . . .	117
3.3.1 Nançay Radioheliograph . . . . .	118
3.3.2 Nançay Decametric Array . . . . .	124
3.3.3 STEREO WAVES . . . . .	126
3.3.4 Rosse Solar Terrestrial Observatory . . . . .	128
3.3.4.1 Antennas and Spectrometers . . . . .	128

---

## CONTENTS

3.3.4.2	Nominal Operations . . . . .	132
3.3.4.3	eCallisto Network . . . . .	132
3.3.4.4	Dynamic spectra from RSTO . . . . .	134
3.3.5	Dynamic Spectra Data Reduction . . . . .	135
<b>4</b>	<b>Coronal Mass Ejection Masses, Energetics, and Forces</b>	<b>139</b>
4.1	Introduction . . . . .	140
4.2	Observations . . . . .	142
4.3	Data Analysis . . . . .	146
4.3.1	Thomson Scattering in the Corona . . . . .	146
4.3.2	Mass Measurement and Geometrical Uncertainties . . . . .	152
4.3.3	Evaluation of uncertainties . . . . .	157
4.4	Results . . . . .	159
4.4.1	Mass vs. Time and Height . . . . .	159
4.4.2	Kinematics and Dynamics . . . . .	162
4.4.3	Evaluation of the Drag and Lorentz Forces . . . . .	165
4.5	Conclusion . . . . .	168
<b>5</b>	<b>Coronal Mass Ejection Shocks and Particle Acceleration</b>	<b>170</b>
5.1	Introduction . . . . .	171
5.2	Coronal Bright Front and Radio Source . . . . .	173
5.2.1	Observations . . . . .	173
5.2.2	Radio Source Height and Speed . . . . .	175
5.2.3	Radio Source Alfvén Mach . . . . .	179
5.2.4	CBF Speeds . . . . .	182
5.2.5	CBF Thermal Properties . . . . .	183
5.3	Radio Dynamic Spectra . . . . .	185
5.3.1	Observations . . . . .	185
5.3.2	Particle speeds and in-situ detection . . . . .	186
5.4	White-light CME and Shock . . . . .	191
5.5	Discussion . . . . .	193
5.5.1	Relationship Between CME, CBF, and Radio bursts . . . . .	193
5.5.2	Bursty Particle Acceleration . . . . .	194

---

**CONTENTS**

<b>6 Conclusions and Future Work</b>	<b>198</b>
6.1 CME Masses and Energies . . . . .	199
6.1.1 Principle results . . . . .	199
6.1.2 Future Work . . . . .	201
6.1.2.1 CME Mass and Forces Catalogue . . . . .	201
6.1.2.2 Mass Estimates with AIA . . . . .	210
6.2 Coronal Shocks and Radio Bursts . . . . .	215
6.2.1 Principle results . . . . .	215
6.2.2 Future Work . . . . .	217
6.2.2.1 Hough Transform and Herringbone Statistics . .	217
<b>A Appendix</b>	<b>228</b>
A.1 Radio Burst Emissivity . . . . .	228
A.2 EUV and pB Density Measurements . . . . .	229
A.3 June 7th 2011 Radio Burst from RSTO . . . . .	231
<b>References</b>	<b>233</b>

# List of Figures

1.1	The solar interior and atmosphere . . . . .	6
1.2	Differential rotation rate as a function of latitude and depth . . . . .	7
1.3	The solar butterfly diagram . . . . .	8
1.4	The Babcock model of magnetic field evolution in the Sun . . . . .	9
1.5	The temperature and density as a function of height above the photosphere . . . . .	13
1.6	AIA image of the corona . . . . .	15
1.7	Comparison of soft X-ray and low frequency radio observations of the corona . . . . .	17
1.8	LASCO C3 image of a CME . . . . .	21
1.9	Distribution of CME speeds . . . . .	23
1.10	CME height, speed, and acceleration as function of time . . . . .	25
1.11	CME acceleration as a function of acceleration duration . . . . .	26
1.12	CME speed profile along side flare X-ray light curve . . . . .	27
1.13	CME energies and masses as a function of height . . . . .	29
1.14	Distribution of CME masses, kinetic and total mechanical energies	31
1.15	Acceleration due to all forces acting on CME . . . . .	33
1.16	Nonthermal synchrotron emission in a CME . . . . .	34
1.17	Energy components of an eruptive event. . . . .	35
1.18	Type II radio burst . . . . .	37
1.19	Low frequency image of a radio shock . . . . .	38
1.20	Comparison of CME and type II height-time kinematics . . . . .	40
1.21	Statistical comparison of CME and type II height-time kinematics	41
1.22	CME flank shock observed by the UVCS spectrometer . . . . .	42

---

## LIST OF FIGURES

1.23	Herringbone radio bursts . . . . .	45
1.24	First observation of an ‘EIT wave’ . . . . .	46
1.25	Comparison of EUV wave and type II height-time . . . . .	47
1.26	Model of EUV wave and coronal shock . . . . .	48
1.27	White-light image of shocks . . . . .	49
2.1	Sweet-Parker and Petscheck reconnection models . . . . .	63
2.2	The catastrophe CME model . . . . .	67
2.3	The breakout CME model . . . . .	70
2.4	The toroidal instability CME model . . . . .	72
2.5	The toroidal instability forces . . . . .	74
2.6	Model of the Alfvén speed as a function of height in the corona . . . . .	75
2.7	MHD shock framework . . . . .	77
2.8	Normal incidence and de Hoffman-Teller reference frames . . . . .	82
2.9	Shock drift acceleration . . . . .	83
2.10	Shock drift acceleration . . . . .	89
2.11	Theoretically predicted radio burst fluxes . . . . .	93
2.12	Model of radio burst driven by expanding CME flanks . . . . .	94
2.13	Solar radio burst morphologies . . . . .	95
2.14	Various models for electron number density in the corona . . . . .	96
3.1	White-light corona during an eclipse . . . . .	99
3.2	Radial variation of the K and F corona . . . . .	100
3.3	The Lyot coronagraph . . . . .	102
3.4	The LASCO C2 coronagraph optics . . . . .	103
3.5	The LASCO C2 coronagraph detail . . . . .	104
3.6	LASCO C2 Observations . . . . .	106
3.7	STEREO spacecraft positions . . . . .	107
3.8	The COR1 coronagraph . . . . .	108
3.9	The COR2 coronagraph . . . . .	109
3.10	COR1 and COR2 observations . . . . .	110
3.11	The AIA telescope design . . . . .	115
3.12	The four telescopes of AIA . . . . .	117
3.13	AIA temperature response . . . . .	118

---

## LIST OF FIGURES

3.14	The Nançay Radioheliograph layout . . . . .	119
3.15	Sky brightness, visibility, beam, and sampling function . . . . .	123
3.16	NRH observations . . . . .	124
3.17	Nançay Decametric Array observations . . . . .	125
3.18	The SWAVES antennas . . . . .	127
3.19	STEREO WAVES observations . . . . .	129
3.20	RSTO Instrumental Setup . . . . .	131
3.21	Callisto Worldwide . . . . .	133
3.22	RSTO RFI Survey . . . . .	134
3.23	Callisto observations type II and herringbones . . . . .	135
3.24	Callisto observations type II and herringbones . . . . .	136
3.25	Callisto observations type II and herringbones . . . . .	137
4.1	2008-December-12 CME observed by COR1 . . . . .	144
4.2	2008-December-12 CMe observed by COR2 . . . . .	145
4.3	Thomson scattering schematic. . . . .	148
4.4	Thomson scattering geometry in the solar corona . . . . .	150
4.5	Line-of-sight and plane-of-sky orientations . . . . .	151
4.6	Electron brightness as function of angle . . . . .	153
4.7	Electron brightness on and away the POS . . . . .	154
4.8	Uncertainty due to CME angular width . . . . .	155
4.9	Uncertainty due to unknown POS angle and angular width . . . . .	156
4.10	CME mass as a function of height and time . . . . .	160
4.11	CME kinematics and energetics as a function of height . . . . .	163
5.1	Propagation of CBF and radio burst . . . . .	174
5.2	Radio source and CBF position angle versus time . . . . .	176
5.3	2D density map of the corona . . . . .	178
5.4	A potential field source surface extrapolation of the corona magnetic field . . . . .	180
5.5	Alfvén speed map of the solar corona. . . . .	181
5.6	Tri-colour running ratio images of a CBF. . . . .	184
5.7	Radio dynamic spectra of 22-September-2011 event . . . . .	187
5.8	Type III speeds . . . . .	189

---

## LIST OF FIGURES

5.9	Herringbone wavelet analysis . . . . .	190
5.10	3D reconstruction of CME and white-light shock . . . . .	192
5.11	CBF and shock orientation . . . . .	195
6.1	CORIMP masks . . . . .	202
6.2	CME Mass automatic detection . . . . .	203
6.3	Inverse masks . . . . .	205
6.4	Inverse mass time series . . . . .	206
6.5	Mass time series error check . . . . .	208
6.6	EUVI dimming region . . . . .	210
6.7	Mass-temperature distribution . . . . .	211
6.8	Mass evacuation with time . . . . .	213
6.9	Line in polar coordinates . . . . .	218
6.10	Relationship between image space and Hough space . . . . .	219
6.11	Example Hough Transform . . . . .	220
6.12	Herringbone observations . . . . .	221
6.13	Hough transform . . . . .	222
6.14	Hough transform herringbones . . . . .	223
6.15	Herringbone statistics 1 . . . . .	224
6.16	Herringbone statistics 2 . . . . .	225
6.17	Herringbone intensity vs drift . . . . .	226
A.1	The geometry for the emitting solar atmosphere . . . . .	230
A.2	The June 7th 2011 radio burst . . . . .	232

# 1

## Observation and Instrumentation

In this chapter the instruments used to make observations of coronal mass ejections and the signatures of their shocks are outlined. The primary technique for observing CMEs is via white-light observations of the corona. The general coronal observing techniques used by coronagraphs are firstly described, followed by specific details of coronagraphs used in this study. This is followed by a description of the instrument used to observe CMEs and shocks, including extreme ultraviolet (EUV) instrumentation, and radio imaging and spectroscopy instrumentation. Part of the radio spectroscopy work includes an overview of the Rosse Solar Terrestrial Observatory (RSTO), installed at Birr Castle, Co. Offaly, Ireland in September 2011. The RSTO work was published in Zucca & Carley *et al.* *Solar Physics*, 2012.



**Figure 1.1:** The white-light corona during a solar eclipse. Occultation of the bright solar disk by the moon reveals the faint outer atmosphere of the Sun, known as the corona. It is highly structured, showing features such as streamers and plumes. *Eclipse photograph courtesy of Miloslav Druckmüller <http://www.zam.fme.vutbr.cz>*

## 1.1 White-Light Observations

The first evidence for the existence of the corona was through observations during solar eclipses. The occultation of the solar disk by the moon revealed a visible outer atmosphere structured into streamers and plumes and extending far from the solar surface (Figure 3.1). This is known as the white-light corona and is due to scattering of photospheric light by coronal particles. Of particular interest here is the K-corona (as first introduced in Section 1.1.3.4); this is the corona that is visible because of Thomson scattering of photospheric light by free electrons. As described in Chapter 1, a component of the scattered white-light is the F-

## 1.1 White-Light Observations

---

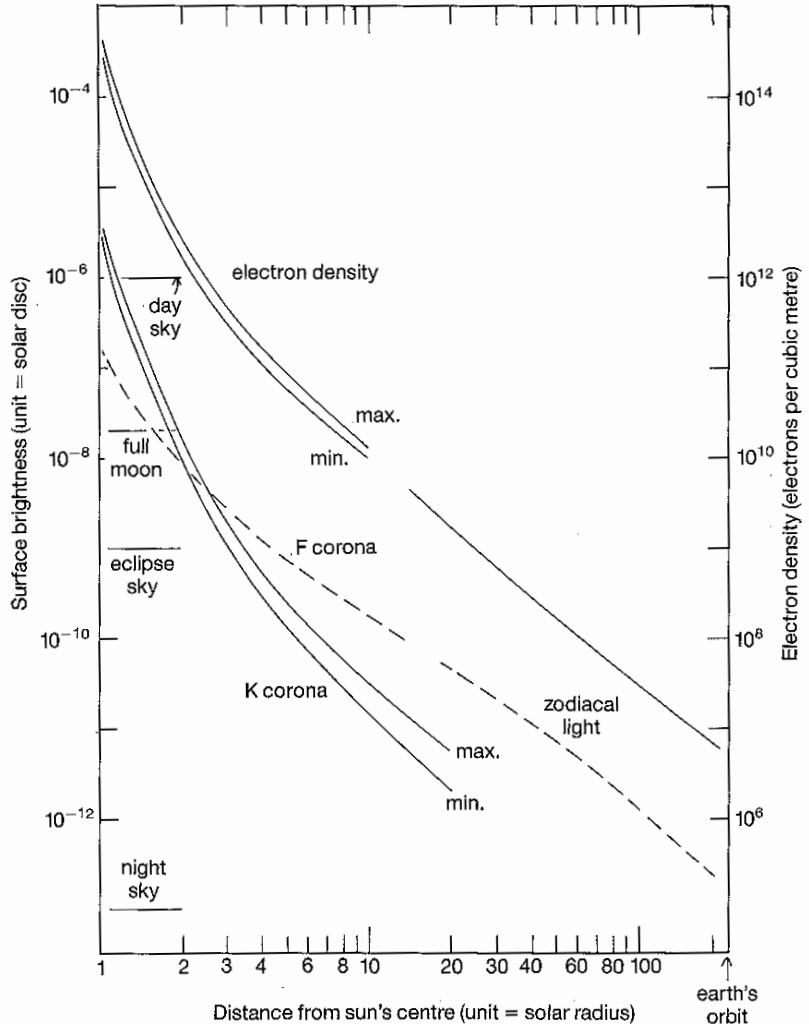


**Figure 1.2:** The K and F coronal brightness and the number density of electrons as a function of height. Units are in mean solar brightness ( $1 \text{ MSB} = 2.01 \times 10^{10} \text{ ergs s}^{-1} \text{ cm}^{-2} \text{ sr}^{-1}$ ), (Phillips, 1995).

corona, which is formed by scattering of light off of dust grains. The F-corona is unpolarized and becomes a significant contributor to the white-light after  $\sim 4R_\odot$ . Figure 3.2 shows the radial variation of the K and F corona, along with coronal densities. Both of these components of the corona are over 1 million times fainter than the solar disk, so they may only be observed when the solar disk is obscured. Before the early 20th century the only way to view the corona was for a short

## **1.1 White-Light Observations**

---

period during a solar eclipse when the moon provides the necessary obscuration of the disk. In 1939 the French astronomer Bernard Lyot developed a telescope, known as a coronagraph, which allowed observation of the corona at any time (Lyot, 1939). A coronagraph is an optical system that blocks direct photospheric light so the much fainter corona can be imaged. A description of Lyot's original design, and the space based instruments based on this design, are given here.

### **1.1.1 Lyot Coronagraph**

A basic schematic of the Lyot coronagraph is given in Figure 3.3. The objective lens O1 forms an image of the solar disk onto to the internal occulting disk D1 (a metal cone), where the light is reflected away from the field lens O2. Lyot's key invention was the Lyot stop (A1) and Lyot spot (D2). The field lens O2 images the aperture A0 and its diffraction pattern onto the Lyot stop. If the Lyot stop were not there, this light would reach the focal plane and contaminate the image. The Lyot spot (D2) blocks spurious light caused by multiple reflections in the field lens O2. It also blocks any light diffracted by the occulter D1. In theory, the only light that is transmitted through the system is that coming from beyond the solar disk. This light is focused onto the image plane F by O3. In practice there may be undesired and excess light that is transmitted through the system and great care is taken to reduce this as much as possible. The Lyot coronagraph is described as internally occulting due to the placement of the occulting disk behind the first objective lens. This is to distinguish it from a externally occulted system in which an extra disk is placed in front of the objective lens. The externally occulted coronagraph prevents photospheric light from entering the optical system in the first place, thus allowing much fainter objects to be imaged. However, the external occulter prevents imaging of the

## 1.1 White-Light Observations

---

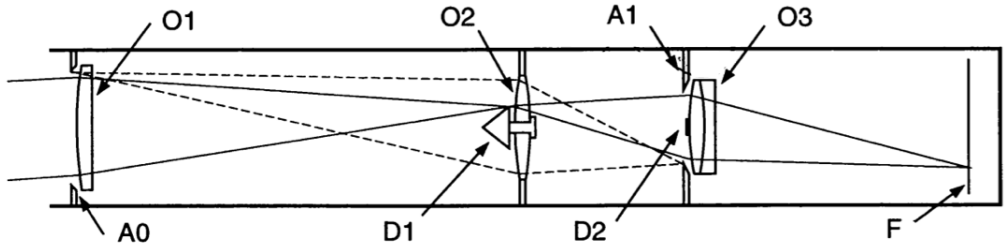


**Figure 1.3:** A schematic of the basic optical design of the Lyot coronagraph. Lyot's key inventions were the placement of a Lyot stop (A1) and Lyot spot (D2) at the positions where diffracted light would contaminate the image and obscure the faint corona (Brueckner *et al.*, 1995).

very low corona. Hence there is a choice between very low contaminant light levels in the telescope or imaging of the low corona.

All coronagraphs inherit their basic design from Lyot's original, and a number of these are space based instruments providing observation of the corona over many height ranges.

### 1.1.1.1 SOHO LASCO

The *Solar and Heliospheric Observatory* (*SOHO*; Domingo *et al.*, 1995) is located at Lagrangian point 1 and carries a suite of in-situ and remote sensing instruments, including three coronagraphs collectively known as the Large Angle Spectrometric Coronagraph (LASCO; Brueckner *et al.*, 1995). LASCO comprises three different coronagraphs, C1, C2, and C3, that were built to observe the corona over heliocentric distance range of  $1.1\text{--}30 R_{\odot}$ .

C1 is a reflector version of the internally occulted Lyot coronagraph that images the corona over a distance range of  $1.1\text{--}3 R_{\odot}$ . A tunable Fabrey-Perot interferometer is placed after the Lyot stop to allow narrow passband images of the solar corona at the lines of Fe XIV, Ca XV, Na I, Fe X, and H $\alpha$ . C1 operates a  $1024 \times 1024$  CCD with a pixel size of  $5.6''$ , giving a spatial resolution of  $\sim 11''$ . The Rayleigh diffraction limited resolution of the telescope is  $3.3''$  at 530.3 nm.

## 1.1 White-Light Observations

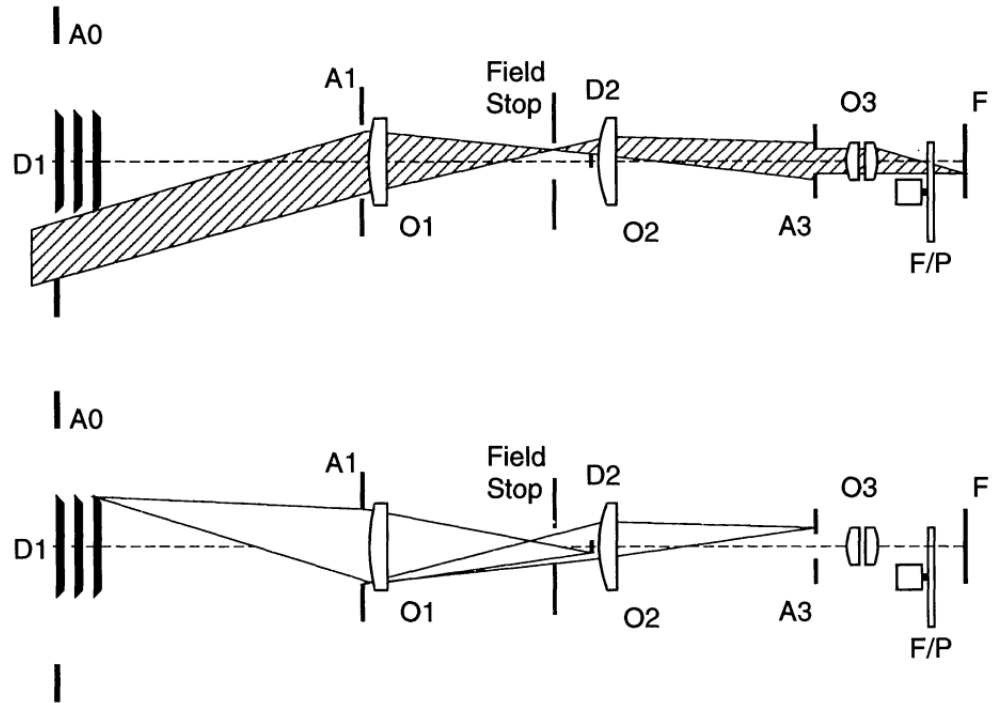


**Figure 1.4:** Conceptual optical layout of the LASCO C2 coronograph. The top ray-tracing diagram shows the image formation, while the bottom diagram demonstrates the stray light suppression and occultation (Brueckner *et al.*, 1995).

Unfortunately C1 failed in 1997 and is no longer in operation.

C2 is an externally occulted, broadband, refractor coronagraph that images the corona from  $1.5\text{--}6 R_{\odot}$  (see footnote<sup>1</sup>). The conceptual diagram for its optical layout is shown in Figure 3.4. The front aperture A0 is on the left of the diagram and includes the external occulter D1, consisting of three consecutive circular disks on a common spindle, these disks completely shadow the entrance aperture A1 from direct sunlight. The disks also successively intercept diffracted sunlight from the one before to minimize the total diffracted light from the solar disk falling on the object lens O1. The disks have fine threads on their edges that have been diamond machined, and have a cone opening angle that is slightly

<sup>1</sup>The levels of stray-light just beyond the occulter mean that in practice the C2 inner field of view limit is  $2.2 R_{\odot}$

## 1.1 White-Light Observations

---

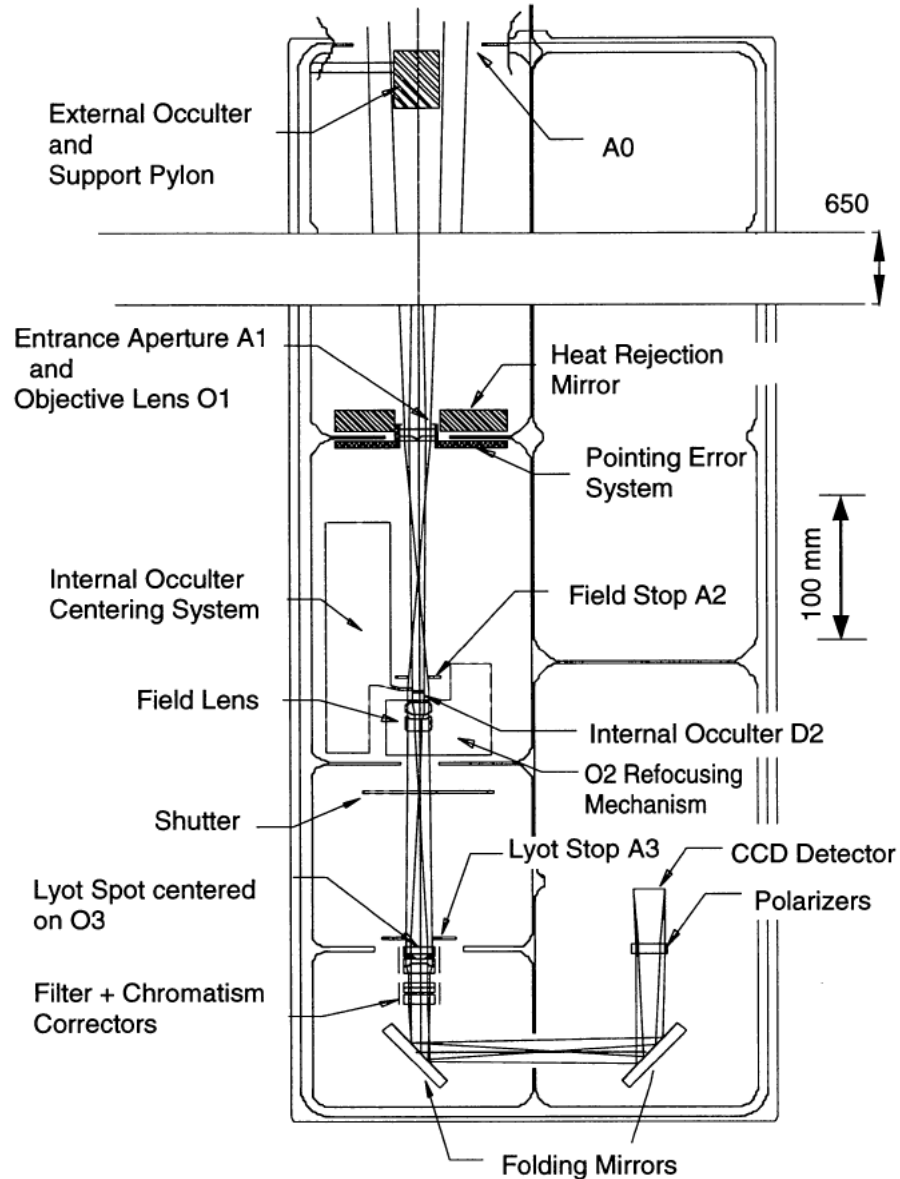


**Figure 1.5:** A detailed layout of the C2 coronagraph optics and mechanical construct (Brueckner *et al.*, 1995).

bigger than the solar disk at L1 ( $32.31'$ ). This ensures a very high level of light rejection at the external occulter. The objective lens O1 images the corona at the field stop, which sets the outer limit to the field of view of the telescope ( $5 R_{\odot}$  for C2). O1 also images D1 onto the D2 internal occulter, which also serves to

## **1.1 White-Light Observations**

---

intercept any residual stray light diffracted at D1. The lens O2 collimates the coronal image and also images the entrance aperture A1 onto the Lyot stop A3. Finally the lens O3 images the corona onto the focal plane F. The combination of the internal and external occulters, the aperture stops, and a heat rejection mirror at the entrance aperture (Figure 3.5), mean that the the coronagraph has stray light levels that are an order of magnitude improvement over previous space based coronagraphs e.g., stray light levels are typically an order of magnitude or more lower than the coronal brightness, allowing the detection of features in the range of  $2 \times 10^{-7}$ – $15 \times 10^{-10} B_{\odot}$  where  $B_{\odot}$  is mean solar brightness (MSB) unit (Brueckner *et al.*, 1995).

The light focused onto the focal plane by the O3 lens first passes through a colour filter and polarizer wheel, which selects the band pass and takes three polarization images at  $0^\circ$ ,  $-60^\circ$  and  $+60^\circ$  such that total or polarized brightness images of the corona may be taken. Mounted at the focal plane is a front-side illuminated  $1024 \times 1024$  CCD, with  $21\mu$  square pixels (equivalent angular size if  $11.4''$ ), operating in a nominal spectral range of  $500 - 700$  nm, at a temperature of  $-80^\circ$  C. CCD readout takes approximately 22 seconds, after which the image may be compressed by a number of algorithms before being sent to the ground station. Among the observing nominal modes are routine flat-field exposures and dark current exposures to be used in calibration. At current operations the C2 coronagraph offers a total brightness image of the corona every 15 minutes.

Finally, C3 is an externally occulted broadband lens coronagraph that images the corona from  $3.7$ – $30 R_{\odot}$ , with a pixel size of  $56''$  and brightness range of  $3 \times 10^{-9}$ – $1 \times 10^{-11} B_{\odot}$ . It has the same optical design as C2 (Figure 3.4).

The C1, C2 and C3 coronagraph data is processed on-board using a number of steps that may compress the data before transmission to an Earth ground

## 1.1 White-Light Observations

---

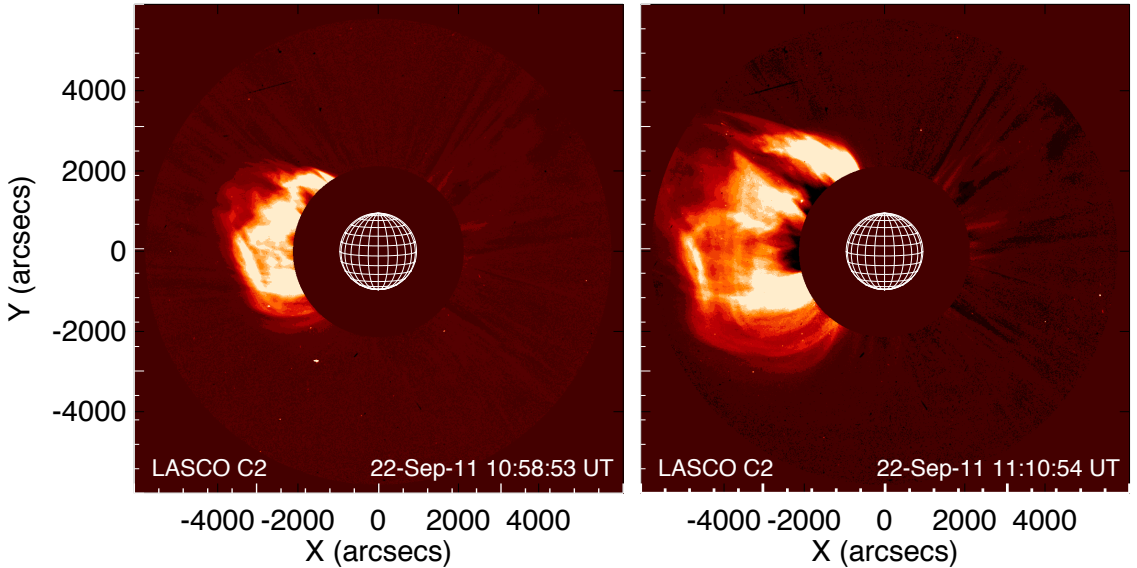


**Figure 1.6:** LASCO C2 Observations of a CME occurring on 22 September 2011. The central disk is from the occulter. A heliographic grid is over-layed to show the size of the sun.

station via the Deep Space Network (DPS). Only the C2 coronagraph is used in this thesis, and some sample level-2 data for C2 is shown in Figure 3.6

### 1.1.1.2 STEREO COR1 and COR2

The *Solar Terrestrial Relations Observatory* (STEREO; Kaiser *et al.*, 2008) Ahead and Behind are two nearly identical spacecraft traveling ahead and behind Earth in its orbit. Each spacecraft is receding from Earth at a rate of  $\pm 22^\circ$  per year, such that they are effectively traveling around the Sun in opposite directions. For the spacecraft locations at three different times see Figure 3.7. They carry an identical set of instruments known as the Sun Earth Coronal Connection and Heliospheric Investigation (SECCHI) suite, including in situ detectors and a variety of imagers. On each spacecraft there are two coronagraphs, COR1 and COR2 (Howard *et al.*, 2008). The Ahead COR1 and COR2 combined with Behind COR1 and COR2 offer a stereoscopic view of the corona and any transient event taking

## 1.1 White-Light Observations

---

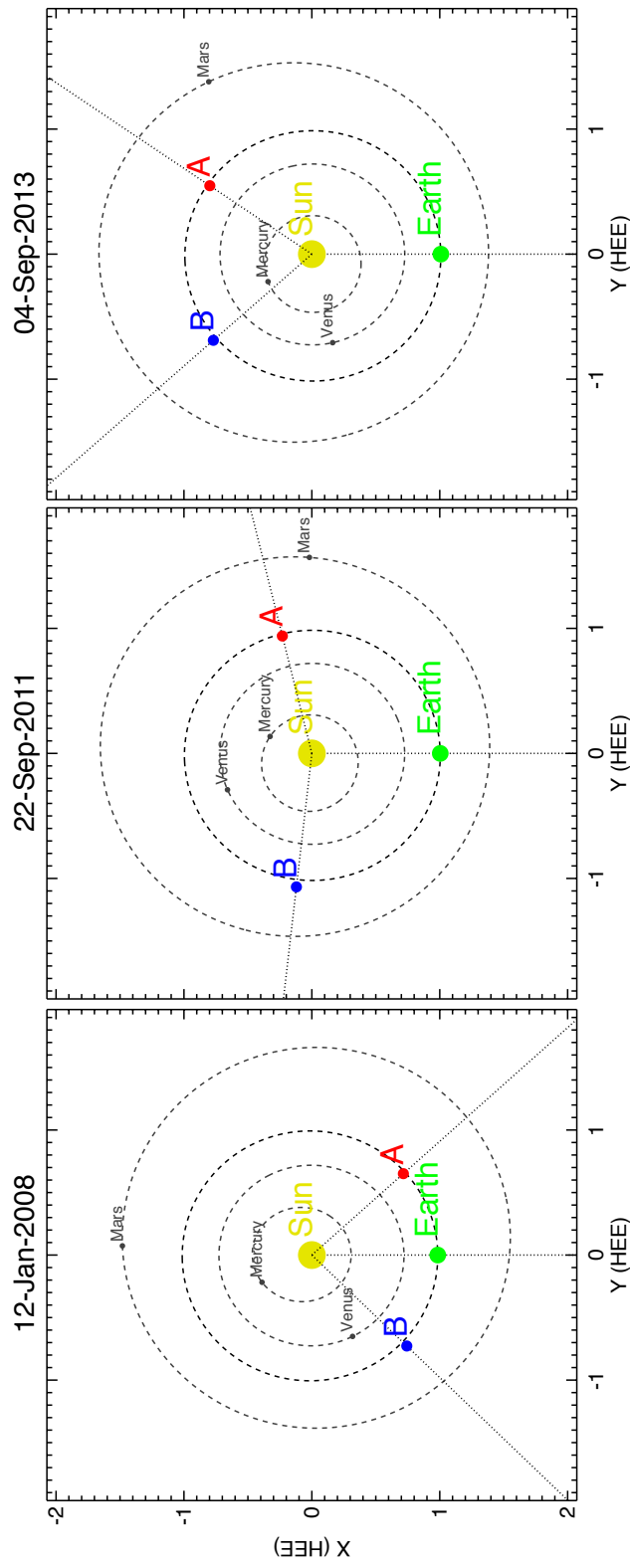
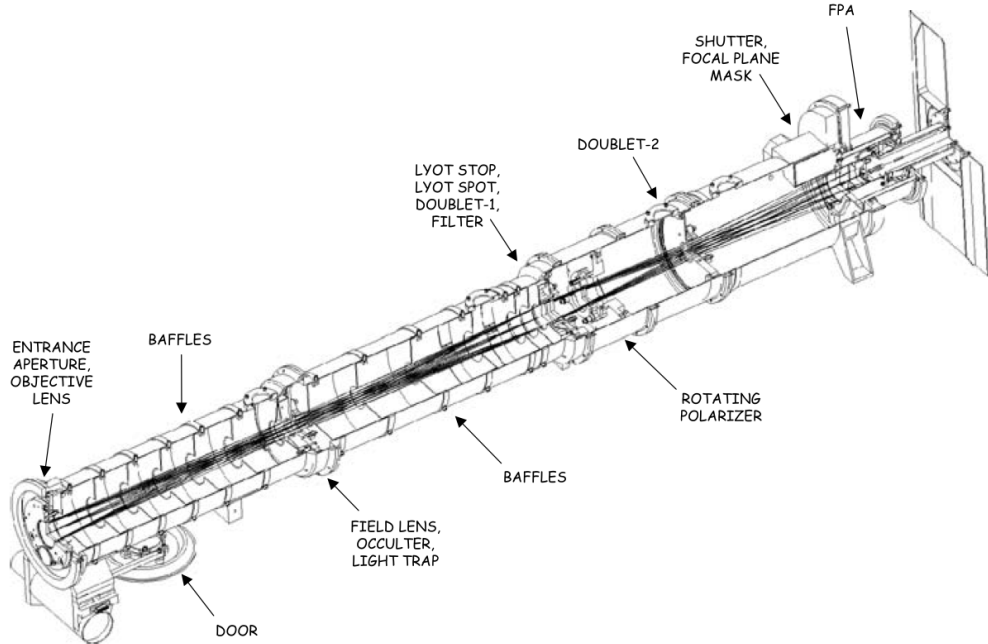


Figure 1.7: The STEREO A and B spacecraft positions with respect to Sun, Earth and inner planets on 12 January 2008, 22 September 2011 and 04 September 2013

## 1.1 White-Light Observations

---



**Figure 1.8:** A schematic of the basic optical design of the COR1 coronagraph. There are two such identical instruments, one on the Ahead and one on the Behind spacecraft. It is the same basic design as the Lyot coronagraph with the addition of baffles to prevent scattered light and a polarizer behind the Lyot stop (Thompson & Reginald, 2008).

place, such as a CME, in a heliocentric distance range of  $1.4 - 15 R_{\odot}$ .

COR1 is an internally occulted Lyot refractive coronagraph (Figure 3.8) and derives its basic design from Figure 3.3. It images the inner corona with a field of view from  $1.4 - 4.5 R_{\odot}$ , centered on the H $\alpha$  line at 656 nm with a 22.5 nm wide passband. It has an internal polarizer located after the first doublet lens in the optical system (Figure 3.8) and takes three images at  $0^\circ$ ,  $\pm 60^\circ$ , so that polarized or total brightness images of the inner corona may be produced. Stray light levels of both COR1 A and B lie between  $0.1 - 1 \times 10^{-6} B_{\odot}$ , and some defects in the field lens can cause ring shaped features with  $1.4 \times 10^{-6} B_{\odot}$  (Howard *et al.*, 2008). The focal plane of the instrument has a  $1024 \times 1024$  pixel CCD, with a platescale of  $3.75''$  per pixel (Thompson & Reginald, 2008). To improve the signal to noise, a

## 1.1 White-Light Observations

---

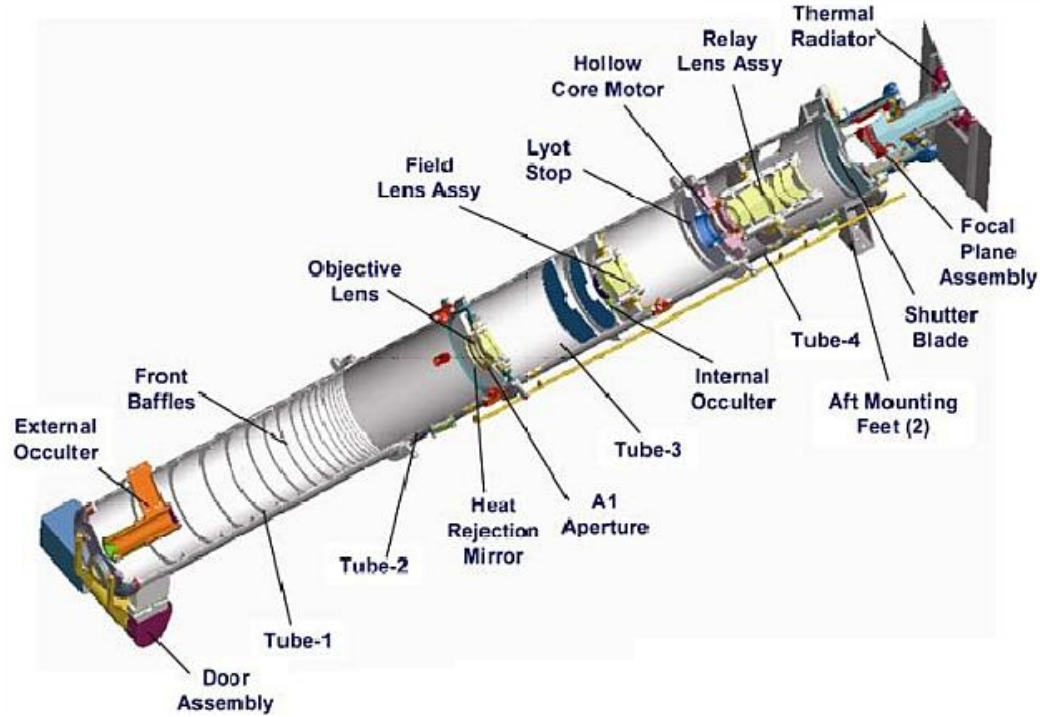


**Figure 1.9:** A schematic of the basic optical design of the COR2 coronagraph. This is an externally occulted coronagraph, meaning it has an extra occultation disk in front of the objective lens. This results in less internally scattered light, but also results in an obscuration of the inner corona. As with COR1, there are two such identical instruments, one on the Ahead and one on the Behind spacecraft (Howard *et al.*, 2008).

$2 \times 2$  pixel binning may be performed. A typical observing sequence will perform three 1 second exposures (one for each polarization state at  $0^\circ$ ,  $-60^\circ$ , and  $+60^\circ$ ), in total taking 11 seconds. Typical CCD read-out times result in an image sequence cadence of 8 minutes (time between a three image set and the next three image set).

COR2 is an externally occulted Lyot coronagraph and derives much of its design from the LASCO C2 and C3 coronagraphs. Externally occulted coronagraphs have an extra occulting disk in front of the objective lens, see Figure 3.9 or Figure 3.4. As described, a downside to this design is that the external occulter does not allow the inner corona to be imaged, hence such coronagraphs are

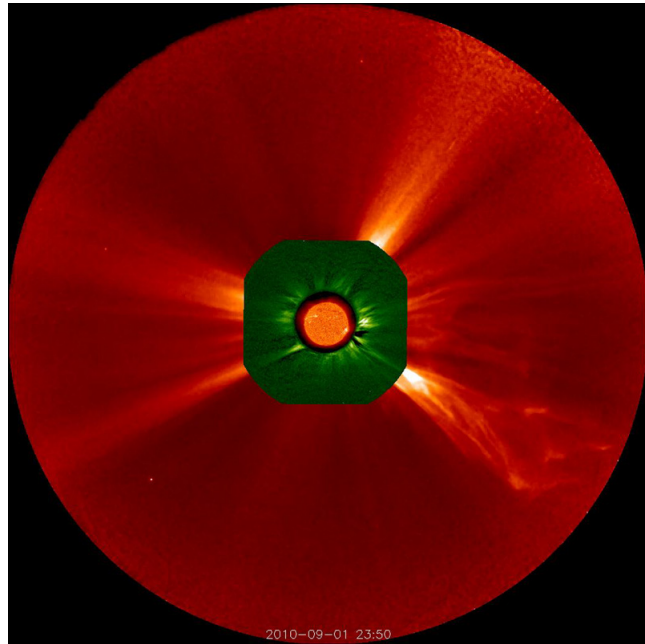


**Figure 1.10:** Observation of the corona from the COR1 (green), and COR2 (red) coronagraphs on board the STEREO Ahead spacecraft, 01 Sep 2009 23:50 UT. An Extreme Ultraviolet Imaging (EUVI) 304 Å image of the sun is shown at the center. A CME was observed, erupting to the south-west. *Image Courtesy of Alex Young, <http://www.thesuntoday.org/>.*

usually used to observe the extended corona to larger heights. The COR2 inner edge field of view limit is defined by the external occulter, while the outer edge is determined by the field stop, resulting in a field of view from  $2.5\text{--}15 R_{\odot}$ . The filter used in the assembly has a bandpass of 650–750 nm at FWHM. The focal plane contains a back-lit CCD that nominally produces  $2048 \times 2048$  images, with  $14.7''$  per pixel. Like COR1 it has an internal polarizer producing three linearly polarized images per observing sequence (30 minutes).

These white light imagers of the corona allow for a stereoscopic view of CMEs in a total field of view covering  $1.4\text{--}15 R_{\odot}$ . The two viewpoint capabilities of these telescopes offer a more accurate observational estimation of both CME kinematics and CME mass, resulting in a better understanding of CME dynamics. A sample observation using COR1 and COR2 from the Ahead spacecraft is shown

## 1.1 White-Light Observations

---

in Figure 3.10

### 1.1.1.3 Whilte-light Image Data Reduction

All coronagraph images, including those produced by COR1, COR2, and the LASCO coronagraphs, have a number of basic image processing steps in common. The amount by which the data has been processed is described in terms of ‘levels’, with the most basic raw data product of the telescope being level-0. Level-0 usually comprises the compressed data that comes directly from the spacecraft telemetry stream via the DPS. The data is processed from level-0 to level-0.5 by decompressing the spacecraft data and re-packaged into flexible image transport system (FITS) files, which is an open standard format for all astronomical images.

Calibration of the data into a scientifically usable format results in level-1 data. The steps to produce level-1 data are as follows:

- Darks current image subtraction. Each CCD will carry some level of residual voltage even when the camera shutter is closed. This residual voltage is due to the thermal energy of the electrons in each well of the CCD. The voltage (thermal energy) must be removed from the image since it is not due to light from an observed source. The ‘dark image’ is taken with the camera shutter closed and an exposure performed as normal (exposure time the same as the raw image). The dark image is simply subtracted from the raw image
- Bias image subtraction. Similar to dark current the CCD will have some charge due systematic defects. These are usually exposed by taking an image with the shutter closed and for the shortest possible exposure times. The bias image is also subtracted from the raw image.

## 1.1 White-Light Observations

---

- Flat field correction. Every CCD will have a non-uniform response across its photon collecting area. One side of the CCD, or any arbitrary grouping of pixels, may naturally be more sensitive than the other pixels. As well as this, the optical system itself may produce some brightness variation across the focal plane. To account for this, the raw image must be divided by a ‘flat-field’ in order to normalize the spatially non-uniform response detected by the CCD. The ‘flat-field’ is an image taken of a uniformly illuminated surface. For space based telescopes this uniformly illuminated image is usually taken by closing the telescope front aperture and lighting a lamp placed near the aperture cover, or the telescope front door may contain a ‘diffuser’ that scatters sun light to provide uniform illumination. The LASCO system uses a quartz filter on the telescope cover that diffuses exterior light, allowing a uniform illumination of the CCD (Brueckner *et al.*, 1995). It is important that the dark current and bias images be subtracted from the flat-field before the raw images (which are also dark and bias image subtracted) is divided by the flat field.

Accounting for dark current, bias, and flat-fielding are the most fundamental of all CCD imaging calibration routines. They can be summarised as

$$I_{cal}(x_i, y_i) = \frac{I_{raw}(x_i, y_i) - I_{dark}(x_i, y_i) - I_{bias}(x_i, y_i)}{|I_{flat}(x_i, y_i) - I_{dark}(x_i, y_i) - I_{bias}(x_i, y_i)|} \quad (1.1)$$

where  $I$  are the images,  $(x_i, y_i)$  are pixel coordinates, and the  $| |$  in the denominator mean that the dark and bias subtracted flat-field is normalized (divided by itself). Other standard techniques beyond the most basic ones include

- Vignetting. All camera imaging systems suffer from vignetting, a reduction in brightness at the edge of the field of view. In coronagraph systems this

## 1.1 White-Light Observations

---

is particularly important since a vignette can occur at the inner field of view, due to the occulting disk and also due to the pylon supports of the disk. Special vignetting calibration images are performed to account for this effect; they are used to normalise the image in the same way as the flat-field is performed.

- De-warping. The image may suffer some geometric distortions due to a deformity in any one of the numerous optical components of the telescope. This may result in the image being warped. Pre-flight experiments completely characterize any optical distortion so that all raw image may be ‘de-warped’.
- Brightness calibration. This is the conversion from CCD data numbers per second ( $\text{DN s}^{-1}$ ) to physical measures of intensity e.g., mean solar brightness (MSB) units ( $1 \text{ MSB} = 2.01 \times 10^{10} \text{ ergs s}^{-1} \text{ cm}^{-2} \text{ sr}^{-1}$ ). The conversion factors may be calculated in a pre-flight lab, or during inflight observations of objects with known intensities. Mercury, Venus, or Jupiter have served as calibrators for COR 1 and 2 (Thompson & Reginald, 2008).

The above steps are the most frequently taken to ensure clean and calibrated astronomical images. They apply to every telescope using a CCD imaging system and every telescope type, including ground and spaced-based systems. For the coronagraphs mentioned above, the steps are performed on each polarization image separately before summing to total or polarized brightness using the following equations

$$B = \frac{2}{3}(I_0 + I_{+60} + I_{-60}) \quad (1.2)$$

$$pB = \frac{4}{3}\sqrt{(I_0 + I_{+60} + I_{-60})^2 - 3(I_0I_{+60} + I_0I_{-60} + I_{-60}I_{+60})} \quad (1.3)$$

## 1.2 Ultraviolet Observations

---

adapted from Billings (1966a).  $I$  are the intensity values in each pixel and the  $0^\circ$ ,  $+60^\circ$ , and  $-60^\circ$  represent the three polarizations states e.g., the polarizations states of COR 1 and 2.

Anything beyond the above calibration steps is termed level-2 and is usually instrument specific or specific to the scientific goal. Chapter 4 will discuss the production of ‘mass images’ where the pixel values have units of grams, this may also be termed level-2 processing.

## 1.2 Ultraviolet Observations

Ultraviolet imaging can provide observations of the high temperature, low corona corona. Quiet coronal plasma temperatures of  $\sim 1 \times 10^6$  K, up to flaring temperatures on the order of  $\sim 10^7$  K, can produce a variety of ionization species of heavy elements such as Fe, O, Mg, or Si, for example. These ionization species are strong emitters in the ultraviolet and extreme ultraviolet wavelengths. Any imagers that have bandpasses centered on such wavelengths can therefore allow us to observe a variety of quiet and active coronal processes such as flares and large scale coronal bright fronts. All ultraviolet imagers of the corona are space-based, the latest of this fleet of telescopes is the Atmospheric Imaging Assembly (AIA) on board the *Solar Dynamics Observatory* (*SDO*; Lemen *et al.*, 2012), launched in 2010.

### 1.2.1 The Atmospheric Imaging Assembly

*SDO* is in a geosynchronous orbit at  $102^\circ$  W longitude, inclined at  $28.5^\circ$ . The on-board ultraviolet imager, AIA, consists of four Cassegrain telescopes (Figure 3.11) that provide visible, ultraviolet (UV), and extreme ultraviolet (EUV) full-disk

## 1.2 Ultraviolet Observations

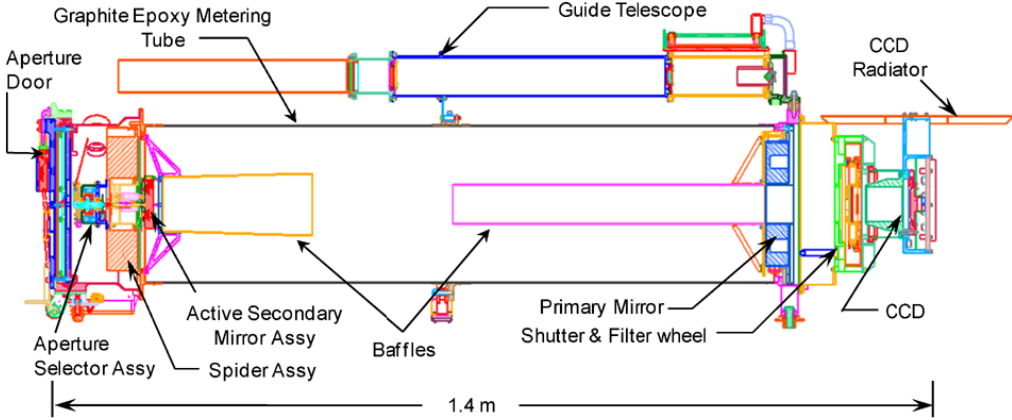


**Figure 1.11:** The Atmospheric Imaging Assembly (AIA) telescope design. AIA employs four Cassegrain type telescopes, with telescope 1, 2 and 4 serving as dual channel passbands, and telescope 3 permitting imaging at three separate passbands (Lemen *et al.*, 2012).

images of the transition region and corona up to  $0.5 R_{\odot}$  above the photosphere with  $0.6''$  spatial resolution and 12-second temporal resolution (Lemen *et al.*, 2012). The telescopes provide imaging in seven extreme ultraviolet passbands centered on the lines of Fe XVIII (94 Å), Fe VIII, XXI (131 Å), Fe IX (171 Å), Fe XII, XXIV (193 Å), Fe XIV (211 Å), He II (304 Å), Fe XVI (335 Å). One of the telescopes observes longer wavelengths at C IV (1600 Å), the nearby continuum at (1700 Å) and a broadband visible filter centered on (4500 Å) giving a full temperature coverage of  $5 \times 10^3$  K to  $2 \times 10^7$  K.

Each telescope has a field of view of  $41'$  circular diameter, a 20 cm primary mirror and an active secondary mirror that is pointed in response to signals from a guide telescope. Each mirror is polished to a roughness of  $< 5 \text{ \AA}$  rms in the spatial frequency range  $10^{-3}$ – $5 \times 10^{-1} \text{ nm}^{-1}$ . The telescopes are dual channel i.e., the mirrors in each telescope have two different multi-layer coatings on either half so as to be reflective at a single desired central wavelength on one half. For example, half of mirror 2 has a peak reflectance at 195.5 Å with the other half reflects at 211.3 Å. These two-channel combinations for each mirror in all four

## 1.2 Ultraviolet Observations

---

telescopes is shown in Figure 3.12. Half of mirror 3 provides the broadband UV and visible channel, with a coating that gives the ability to reflect at 1600, 1700, and 4500 Å, while the other half of the mirror provides the primary optics for the 171 Å channel. Hence telescope 3 provides the optics for four different bandpasses. The coronal plasma temperature response of each telescope channel is shown in Figure 3.13

Metal entrance filters at the aperture of each telescope, combined with a filter wheel located in front of each focal plane, suppress unwanted UV, visible, and infrared radiation. The filters are either made of aluminium, used for wavelengths of 171 Å or longer, and zirconium used for the shorter 94 Å and 131 Å wavelengths. Telescope 3 has an aluminium (for 171 Å) and MgF–2 (for the UV broadband) entrance window and 3 different filters on the filter wheel that cater for observation in 171 Å (aluminium), 1600 Å (MgF–2), 1700 Å and 4500 Å (fused silica). A mechanical shutter regulates exposure time to nominal short exposure of 5 ms and nominal long exposure of 80 ms. Flight software can also select any custom exposure time. The focal plane of each telescope contains a back-illuminated  $4096 \times 4096$  pixel CCD, with each square pixel having a  $12\text{ }\mu\text{m}$  size. Each CCD is read out in 4 quadrants, via an amplifier, into a camera box with four interfaces (one for each quadrant). Each quadrant is read out at a rate of  $2\text{ Mpixels s}^{-1}$  and data transmission to the on-board computer occurs at a rate of  $100\text{ Mb s}^{-1}$ . All of the steps above described for white-light calibration are relevant for ultraviolet CCD imaging also. The AIA calibration procedure to bring the data from level-0.5 to level-1 include de-biasing, dark subtraction, flat-fielding, de-vignetting, de-warping, and brightness calibration, as described in the white-light calibration section. Some example images of AIA are shown in Figure 1.6.

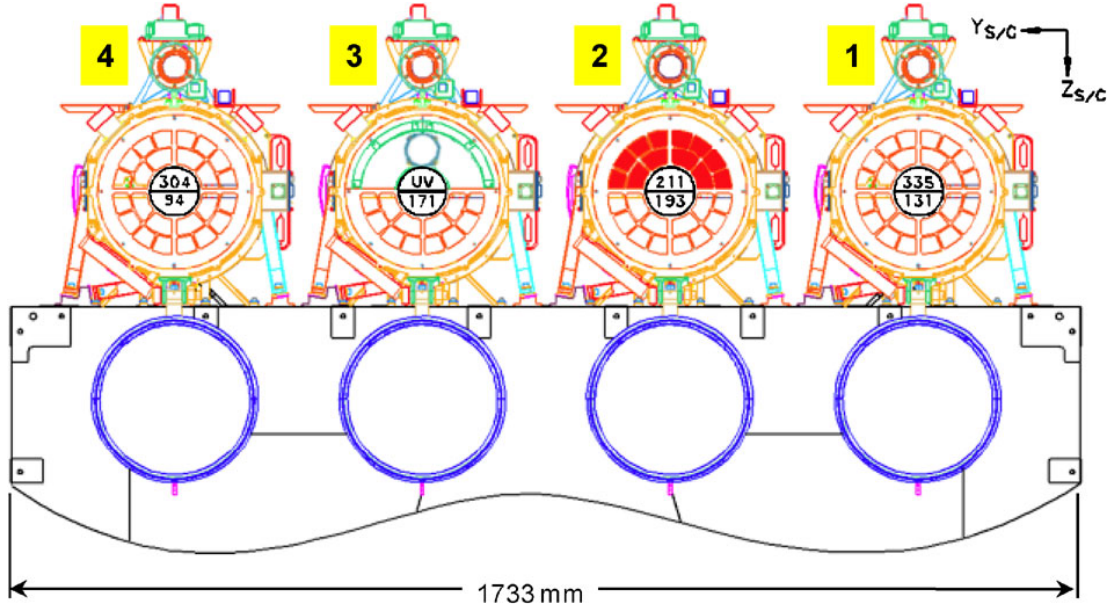


**Figure 1.12:** The four telescopes making up the Atmospheric Imaging Assembly (AIA) (Lemen *et al.*, 2012). Each telescope is dual channel.

### 1.3 Radio Observations

Radio observations provide insight into the thermal process on the quiet sun as well as the high-energy non-thermal processes occurring during solar flares or coronal mass ejections. Radio emission mechanisms are varied and sometimes extremely complex, including thermal and non-thermal bremsstrahlung, cyclotron, gyrosynchrotron, and synchrotron radiation, and coherent free particle emissions such as electron-cyclotron masers and plasma emission. On the Sun, these emission mechanisms cover the entire radio band from microwave to low frequency. The observations in this thesis mainly include the low frequency bands covering kHz–MHz ranges. These ranges allow observations of the quiet sun (thermal bremsstrahlung), as well as the non-thermal radio burst plasma emission outlined in Sections 2.3.4–2.3.6. Some imaging and spectroscopy instruments for these observations are outlined below.

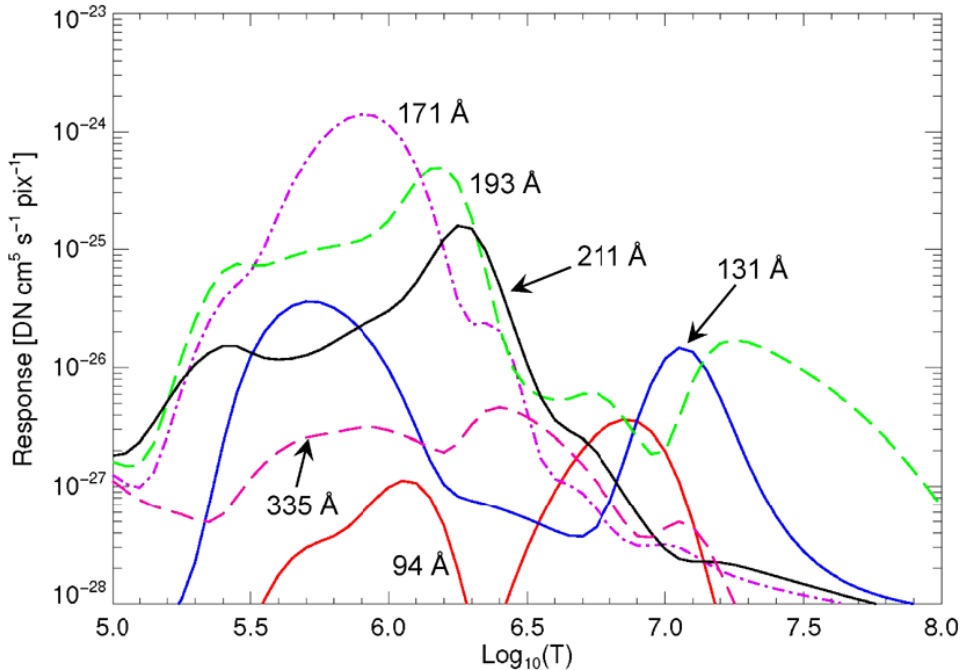


**Figure 1.13:** The Atmospheric Imaging Assembly temperature responses for each of its passbands. The passbands cover temperatures that include the transition region, to quiet corona, to flaring corona. The 4500 Å passband is not shown here, it's temperature coverage results in photospheric imaging (Lemen *et al.*, 2012).

### 1.3.1 Nançay Radioheliograph

The Nançay Radioheliograph is a solar-dedicated radio interferometer located at Nançay, central France ( $47^{\circ}\text{N}$   $2^{\circ}\text{E}$ ), that observes at ten frequencies between 150 and 450 MHz (Kerdraon & Delouis, 1997). As shown in Figure 3.14, the array antennas are arranged in a perpendicular ‘T’ shape. The east west array consists of 19 antennas providing baselines in the range of 50 m to 3200 m. Four of these antennas have parabolic collectors with four orthogonal thick dipole feeds at the focus providing two orthogonal polarizations in the 150-450 MHz band. The remaining 15 have no collectors (no dishes) and consist only of thick dipole antennas providing linear polarization only. The north-south array consists of 24 five meter dishes with wide band feeds, covering baselines between 54 to 1248 m.

### 1.3 Radio Observations

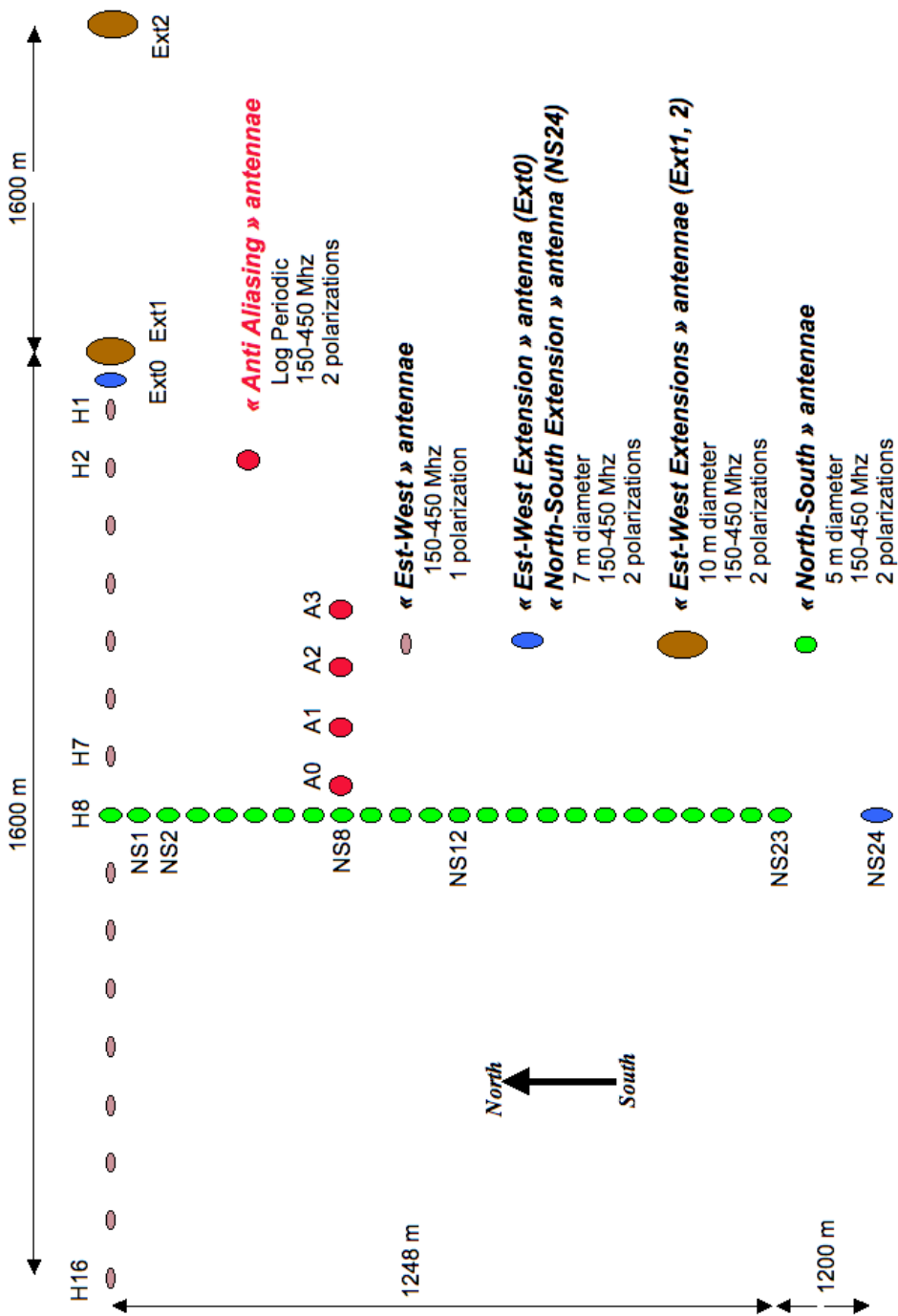


Figure 1.14: The Nançay Radioheliograph layout, showing the east-west baselines and north-south baselines. The antenna types are also shown. *Image courtesy of Alain Kerdraon.*

### 1.3 Radio Observations

---

The antenna front end electronics include low-noise, high dynamic range (45 dB) pre-amplifiers, band filters for frequency switching and a local oscillator which mixes the signal 113 MHz before it is sent to the receiver (Avignon *et al.*, 1989). At the receiver the signal is further mixed down to 10.7 MHz and fed through a bandpass filter of 700 kHz width (final bandwidth of each observed frequency), digitized by 5 ms sampling and sent to the correlator.

The original array consisted of only the east-west baselines, with the north-south being added later in the early 1980s (Bonmartin *et al.*, 1983); originally the two separate arrays operated off different correlators. Nowadays a single digital correlator processes data from all antenna pairs (576 correlations, excluding redundant antenna pairs). The correlator produces 1D images, offering projected intensity profiles along two axes. Full 2D maps may be created by Earth rotation synthesis using the standard 1D observations over one entire day (The Radio-heliograph Group, 1993). Since 1997 the digital correlator has provided fast 2D images using the most westerly 17 antennas of the east-west baseline (Kerdraon & Delouis, 1997), resulting in a spatial resolution that is 4 times lower than the 1D east-west images. Systematic daily observations of 2D images are usually performed at 1 image per second, with quick-look data provided at one image every 10 seconds.

All radio interferometers measure a property known as visibility, which is the Fourier transform of the observed sky brightness distribution

$$V(u, v) = \int I(l, m) \exp(i2\pi[ul + vm]) dl dm \quad (1.4)$$

where  $V$  is the visibility,  $(u, v)$  are the spatial frequency of fringes on the sky, corresponding to the angular sky coordinates  $(l, m)$ .  $I(l, m)$  is the brightness distribution across the sky. This means that the output of an interferometer may

### 1.3 Radio Observations

---

be inverse Fourier transformed to obtain the sky brightness distribution

$$I(l, m) = \int V(u, v) \exp(-i2\pi[ul + vm]) dudv \quad (1.5)$$

This equation applies to the ideal case. In reality the visibility function is initially uncalibrated  $V'(u, v)$ , and sampling of the visibility is discrete in  $(u, v)$  space i.e., if an interferometer has  $n$  telescopes in the array, then it will have  $n(n - 1)/2$  baselines (telescope pairs). This means that there is only  $n(n - 1)/2$  samples of visibility  $V$ . The sampling of the discrete points in space is represented by a sampling function  $S(u, v) = \delta(u - u_k, v - v_k)$ , where  $\delta$  is a Dirac delta function and  $(u_k, v_k)$  are the positions in  $(u, v)$  space at which there is sampling. Equation 3.5 thus becomes

$$I_D(l, m) = \int S(u, v) V'(u, v) \exp(-i2\pi[ul + vm]) dl dm \quad (1.6)$$

Firstly, the original visibilities must be calibrated to obtain  $V(u, v)$  from  $V'(u, v)$ . Calibration usually involves characterising the gain  $G$  of an interferometer and any phase corrections  $P$  that need to be made. This is done by observing a strong radio point source of known flux (known ideal  $V$ ) such that  $G$  and  $P$  may be characterised in the equation

$$V'(u, v) = G[P[V(u, v)]] \quad (1.7)$$

NRH instrument phase and gain calibration is performed by observing Cygnus A. Phase and gain accuracy for these measurements are  $5^\circ$  and 5%, respectively, with only 1 calibration per week necessary because of good system stability (Avignon *et al.*, 1989)

### 1.3 Radio Observations

---

Calibrated visibilities are then used in Equation 3.6. If we represent the Fourier transform by  $\mathfrak{F}[\cdot]$ , and using the convolution theorem then Equation 3.6 becomes

$$I(l, m) = \mathfrak{F}[S(u, v)V(u, v)] = \mathfrak{F}[S(u, v)] * \mathfrak{F}[V(u, v)] \quad (1.8)$$

Given that the Fourier transform of the sampling function is the beam of the instrument  $\mathfrak{F}[S(u, v)] = B(l, m)$  i.e., its point spread function, and as shown above  $\mathfrak{F}[V(u, v)] = I(l, m)$ , this gives

$$I_D(l, m) = \mathfrak{F}[S(u, v)] * \mathfrak{F}[V(u, v)] = B(l, m) * I(l, m) \quad (1.9)$$

Hence the result of Equation 3.6 is the sky brightness distribution convolved with the instrument beam, this image is known as the dirty map  $I_D(l, m)$ . The dirty map will contain the sources in the actual sky brightness distribution but they are contaminated with the side lobes of the instrument beam (Figure 3.15). In order to obtain  $I(l, m)$  from  $I_D(l, m)$  we must ‘deconvolve’ the beam from the dirty map. The main deconvolution algorithm used to obtain  $I(l, m)$  from  $I_D(l, m)$  is known as CLEAN. CLEAN works by locating the peak emission in the dirty map  $I_{D,max}(l_i, m_i)$ , subtracting the dirty beam  $B(l, m)$  from the peak, and placing a point source at a corresponding location  $(l_i, m_i)$  in an ‘empty’ clean image. It then finds the next peak in  $I_D$  and repeats the process. The result is a clean image of point sources at locations that correspond to the peak locations in the dirty map. The clean image is then convolved with a ‘clean beam’ i.e., a beam without sidelobes (a 2D gaussian in the simplest case). After all sources are subtracted from  $I_D(l, m)$ , we are left with a ‘residual’ map. This residual map is added to the clean image to take into account that the sources in the image have different intensities. The result is an image of the sky-brightness distribution

### 1.3 Radio Observations

---

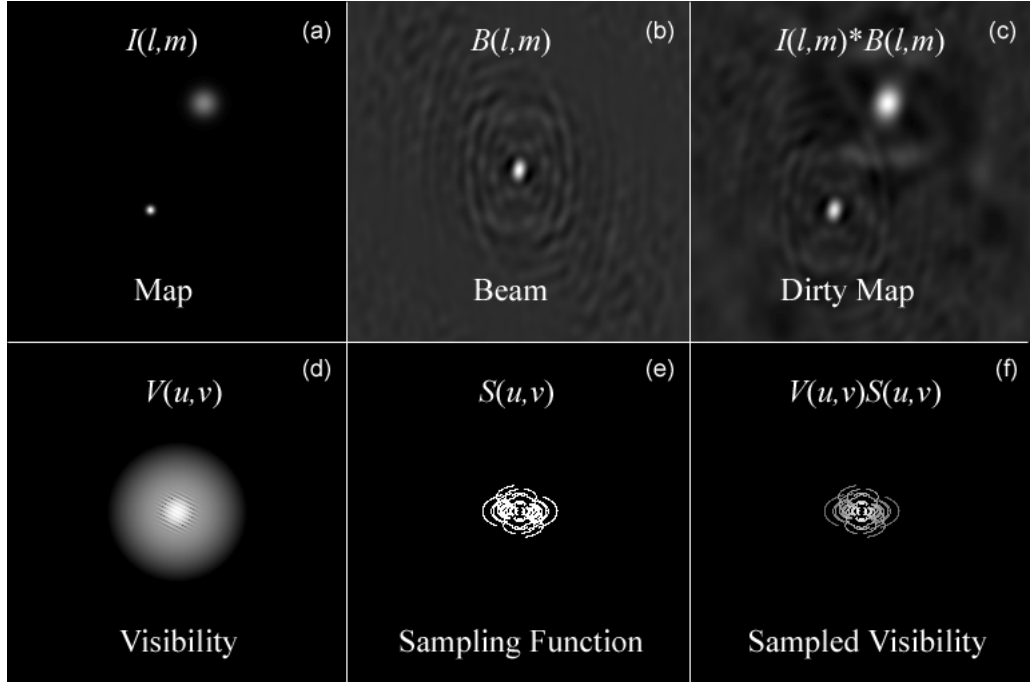


**Figure 1.15:** Relationship between sky brightness distribution  $I(l, m)$ , visibility  $V(u, v)$ , instrument beam  $B(l, m)$ , and sampling function  $S(u, v)$ . Panel (c) shows the dirty map, showing the original sky brightness distribution convolved with the instrument beam. *Image courtesy of Dale Gary (<http://web.njit.edu/gary/728/>).*

without contamination from the beam sidelobes.

CLEAN works best when all sources in the image have the same spatial scale, however it performs poorly when sources in the image exhibit size structure on a variety of scales (Wakker & Schwarz, 1988). When observing the Sun there are multiple size scales on which sources occur in the image, therefore NRH uses a custom Multiscale-CLEAN algorithm that operates on the dirty map at different scales (Mercier *et al.*, 2006). Some examples of NRH images are given in Figure 3.16. The NRH instrument properties are summarised in Table 3.1

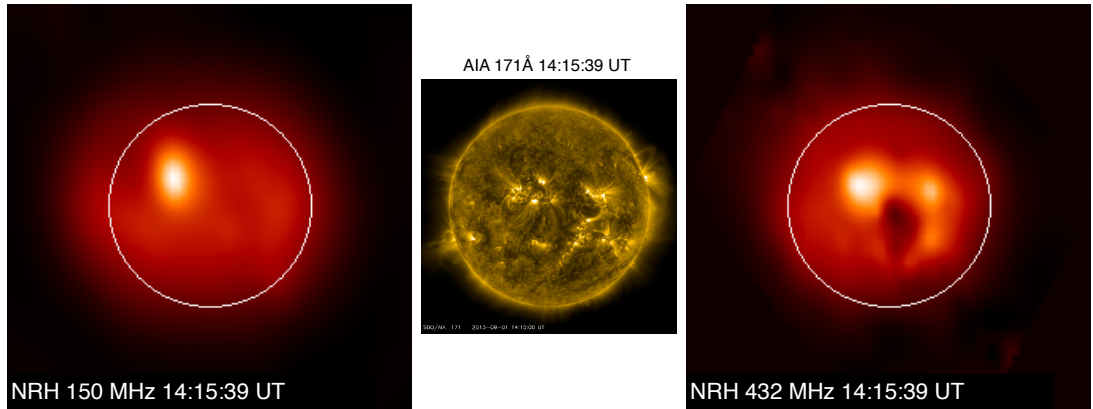


**Figure 1.16:** Observations from NRH at 150 MHz and 432 MHz, with AIA 171 Å for comparison. All three images were taken at the same time at 14:15 UT on 01 September 2013.

Nancay Radioheliograph Properties	
No. of Antennas	19 EW, 24 NS ('T' shape)
Time resolution	5 ms (integrated to 0.1–1 s for 2D images)
Spatial Resolution	0.3 – 6 ″, depending on freq. and direction
Dynamic range	> 45 dB
Observing frequencies	10 frequencies between 150–450 MHz
Bandwidth	700 kHz
Polarization	Stokes I and V
Observing time	7.5 hr centered around 12 UT

**Table 1.1:** NRH properties compiled from (Kerdraon & Delouis, 1997)

### 1.3.2 Nançay Decametric Array

The Nançay Decametric Array consists of 72 (6 east  $\times$  12 west) conical antennas, with each antenna consisting of a left-handed helically wound component and a right handed helical component – this makes the array contain 144 antennas in total, with  $8000 \text{ m}^2$  effective aperture at 30 MHz (Lecacheux, 2000). Each helix antenna is made of eight copper-steel wires wound on the surface of a cone and connected to the output coaxial cable by diode switches; only six wires are used at a time to form the antenna; the other two, diametrically opposite, are

### 1.3 Radio Observations

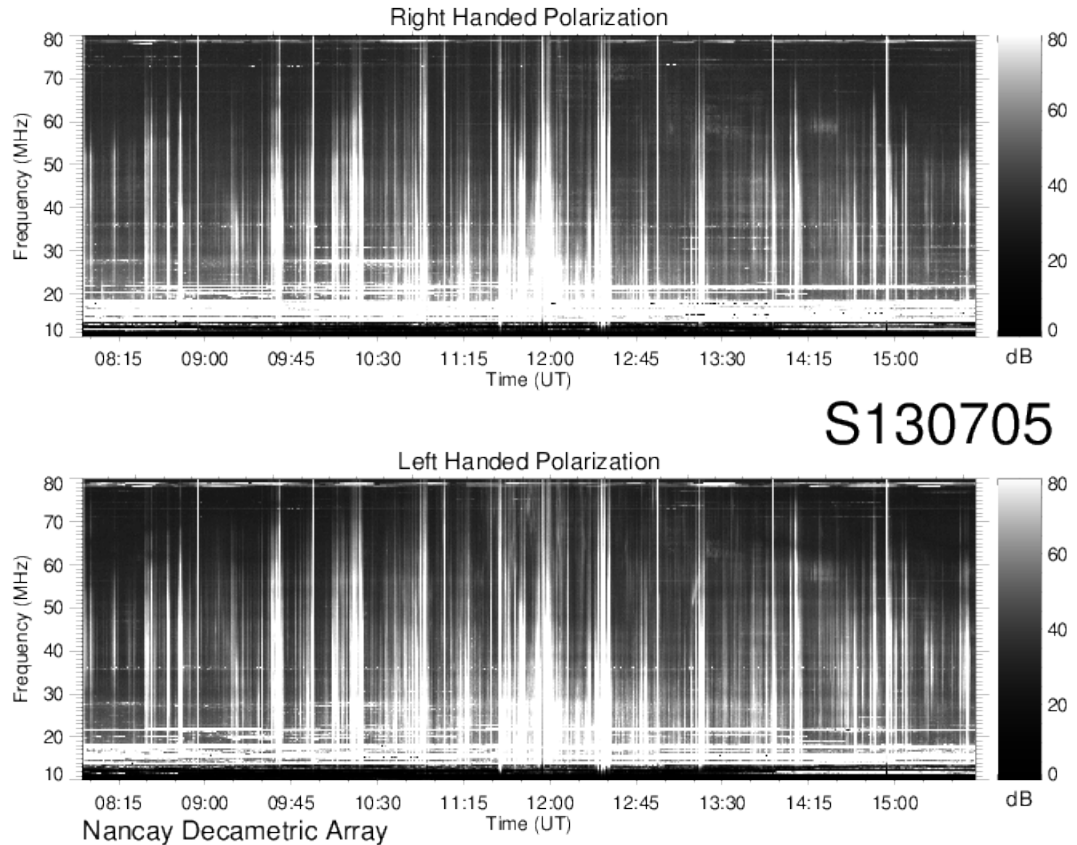


**Figure 1.17:** Nançay Decametric Array observations of an active period of type III radio bursts on 07 May 2013. Image courtesy of the <http://secchirh.obspm.fr/survey.php>

left disconnected. By changing the connections through the diode switches, the antenna can be electrically rotated around the cone axis, corresponding to a phase change of the antenna by steps of  $45^\circ$ . The antennas are broadband (20–120 MHz), low gain (low directivity) with a half power beam width of  $90^\circ$  centered on the cone axis (Boischot *et al.*, 1980). The entire array is steerable by phase delays within the  $90^\circ$  beam width of the individual antennas resulting in a possible tracking time of  $\pm 4$  hr around the meridian, within a declination range of  $-20^\circ$  to  $+50^\circ$ .

The backend of the array consists of three possible receivers: a wide-band

swept-frequency analyzer which operates 400 channels between 20-90 MHz. Left and right hand circular polarization are alternately sampled every 0.5 seconds from the left and right hand helical feeds of the antennas. The nominal operations for solar radio burst monitoring use this swept frequency receiver but there are other more sophisticated receivers available such as a spectro-polarimeter with 1 ms time sampling over 1024 channels and with a 60 dB dynamic range. However, it has only a 12.5 MHz instantaneous band, which is not so useful for solar radio burst monitoring. Some sample data from the decametric array is shown in Figure 3.17

### **1.3.3 STEREO WAVES**

Below  $\sim$ 10 MHz the Earth's ionosphere prevents the propagation of radio waves, hence radio emission below this frequency cannot be observed from ground-based observatories. To overcome this problem, there are a number of space based instruments that observe frequencies in the deca and kilometric wavelength ranges; the STEREO Ahead and Behind spacecraft each carry such an instrument, known as STEREO WAVES or S/WAVES (Bougeret *et al.*, 2008). This instrument directly inherits its design from the Ulysees (Stone *et al.*, 1992), Wind (Bougeret *et al.*, 1995), and Cassini (Gurnett *et al.*, 2004) spacecraft.

The antenna system on each STEREO spacecraft consists of three mutually orthogonal 6-meter Beryllium-Copper monopole elements (Bale *et al.*, 2008), Figure 3.18. The elements' diameter at the base is 1 inch and tapers to 0.6 inches at the tip. The three monopoles are each connected to low noise and high impedance preamplifier, each feeding a number of receiving systems including the Fixed Frequency Receiver (FFR), the Time Domain Analyzer (TDS), and two frequency domain analyzers known as the Low Frequency Receiver (LFR) and High Fre-

### 1.3 Radio Observations

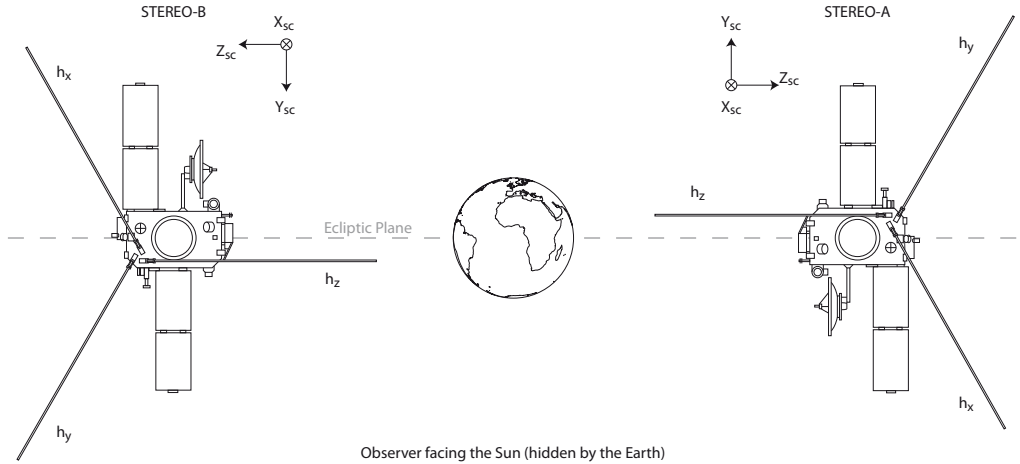


**Figure 1.18:** Configuration of the STEREO/WAVES antennas as seen from the Sun-Earth line, facing the Earth. Each monopole is 6 m long and feeds a number of receiving instruments. *Image courtesy of B. Cecconi, <http://typhon.obspm.fr/stereo/antenna.php>.*

quency Receiver (HFR); only the LFR and HFR are described here.

The LFR is a direct conversion receiver that performs dynamic spectral analysis in the 2.5–160 kHz band. The signal feed from the antennas and pre-amp is passed through a wavelet-like transform to perform digital spectral analysis in three 2-octave bands which each have 16 logarithmically spaced frequency channels (resulting in 48 log spaced channels in the 2.5–160 kHz range). Receiver automatic gain control (AGC) ensures a high dynamic range of 120 dB. Various combinations of the three antenna elements can be made to produce pseudo-dipole or monopole configurations. The signal is then 12-bit digitized and sent to a Digital Processing Unit (DPU)

The HFR is a dual sweeping receiver operating in the frequency range 125 kHz–16.025 MHz. It uses a super-heterodyne technique to down-convert the signal frequencies to odd multiples of 25 kHz that specifically avoid lines of noise generated by the spacecraft power supply, which may produce harmonic multiples of 50 kHz. Due to the down-conversion process the HFR frequency range is cov-

ered in multiple steps of 50 kHz increments, thus the highest spectral resolution is 50 kHz. It has a dynamic range of 80 dB. Like the LFR, it can receive various combinations of the three antenna elements in dipole or monopole modes. The signal is digitized by the same DPU as the LFR.

The time domain resolution for both the LFR and HFR is determined by the DPU. Nominal time resolution of the dynamic spectra produced by both receivers is 1 minute. Sample dynamic spectra of the LFR and HFR from both Ahead and Behind spacecraft is shown in Figure 3.18

#### 1.3.4 Rosse Solar Terrestrial Observatory

##### 1.3.4.1 Antennas and Spectrometers

The Rosse Solar Terrestrial Observatory was established in 2010 at Birr Castle, Co. Offaly, Ireland ( $53^{\circ} 05' 38.9''$ ,  $7^{\circ} 55' 12.7''$ ) (Zucca *et al.*, 2012). The primary objective of the observatory is to observe low frequency radio bursts occurring in the solar atmosphere and the ionospheric and geomagnetic response following this radio activity. To date, three *Compound Astronomical Low-cost Low-frequency Instrument for Spectroscopy and Transportable Observatory* (CALLISTO; Benz *et al.*, 2005) spectrometers have been installed, with the capability of observing in the frequency range 10–870 MHz. The receivers are fed simultaneously by biconical and log-periodic antennas. Nominally, frequency spectra in the range 10–400 MHz are obtained with 4 sweeps per second over 600 channels. The instrumental set-up is described here.

RSTO employs three callisto receivers that cover the ranges of 10–100, 100–200, 200–400 MHz, respectively. The 10–100 MHz receiver (Callisto-1), is fed (via frequency up-converter) by a biconical Schwarzbeck antenna, model number VHBD 9134. The antenna elements are 4 m long allowing a nominal frequency

### 1.3 Radio Observations

#### STEREO/WAVES Daily Summary - 22-Sep-2011 (DOY 265)

Ahead source file = swaves\_ahead\_2011-265\_1\_04.fin  
Ahead PSE Angle = xxx.x

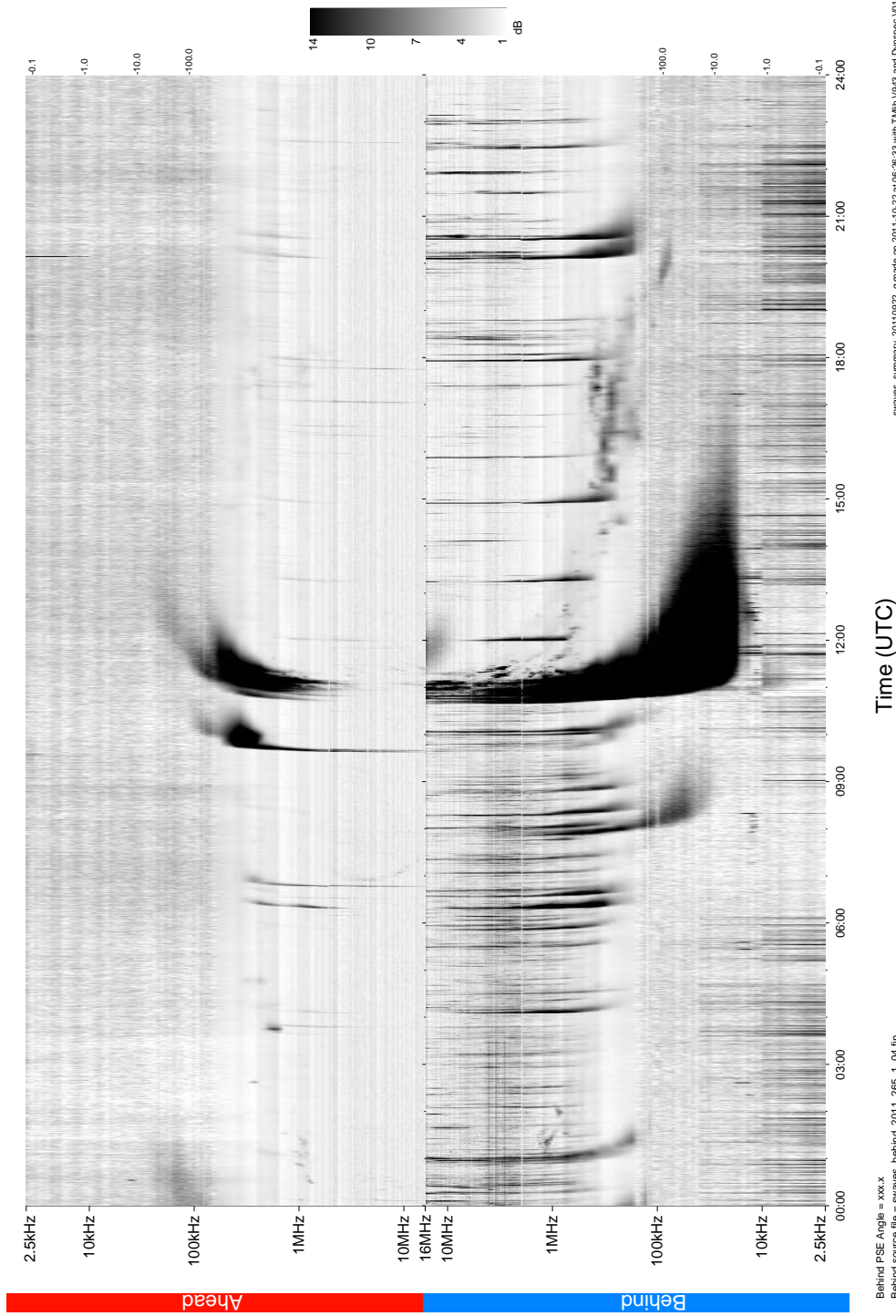


**Figure 1.19:** STEREO WAVES observations from the Ahead and Behind spacecraft from 22 September 2011. A strong type III and interplanetary type II burst were observed by the Behind spacecraft. *Image courtesy of the STEREO Waves team <http://swaves.gsfc.nasa.gov/>.*

### **1.3 Radio Observations**

---

bandwidth of 20–200 MHz. Signal feed from the bicone to Callisto-1 is via  $70\Omega$  coaxial cable,  $\sim 20$  meters in length (Figure 3.20). The bicone is mounted on a Yaesu-1 motor that permits solar tracking in the azimuth direction only (the antenna beam is symmetric in elevation).

The 100–200 and 200–400 MHz (Callisto-2 and -3, respectively) are fed by a Tennadyne T28 log-periodic antenna. The antenna has a frequency band of 50–1300 MHz with a  $\sim 50$  degree half-power beam width (HPBW). Signal from the antenna is fed into a 10 dB pre-amplifier followed by a signal splitter which feeds Callisto-2 and Callisto-3, see Figure 3.20. The digitized data for these two receivers is sent to the control PC via four RS422 conversion units. RS422 is used because of the high baud-rate and length of the cables ( $\sim 30$  m) i.e., there may be interrupts and losses over this path length so the signal is sent differentially. The log-periodic antenna is fixed to an Eiges Alt-Az motor with an EPS-103 control unit, allowing tracking of the Sun throughout the day.

Callisto spectrometers were designed and built in ETH Zurich to monitor solar radio bursts in a frequency range of 10–870 MHz (Benz *et al.*, 2005). The receiver is composed of standard electronic components, employing a Digital Video Broadcasting-Terrestrial (DVB-T) tuner assembled on a single printed circuit board. The number of channels per frequency sweep can vary between 1 and 400, with a maximum of 800 measurements per second. An individual channel has a 300 kHz bandwidth during a typical frequency sweep of 250 ms, and can be tuned by the control software in steps of 62.5 kHz to obtain a more detailed spectrum of the radio environment. The narrow channel width allows for the measurement of selected channels that avoid known bands of radio interference from terrestrial sources.

### 1.3 Radio Observations

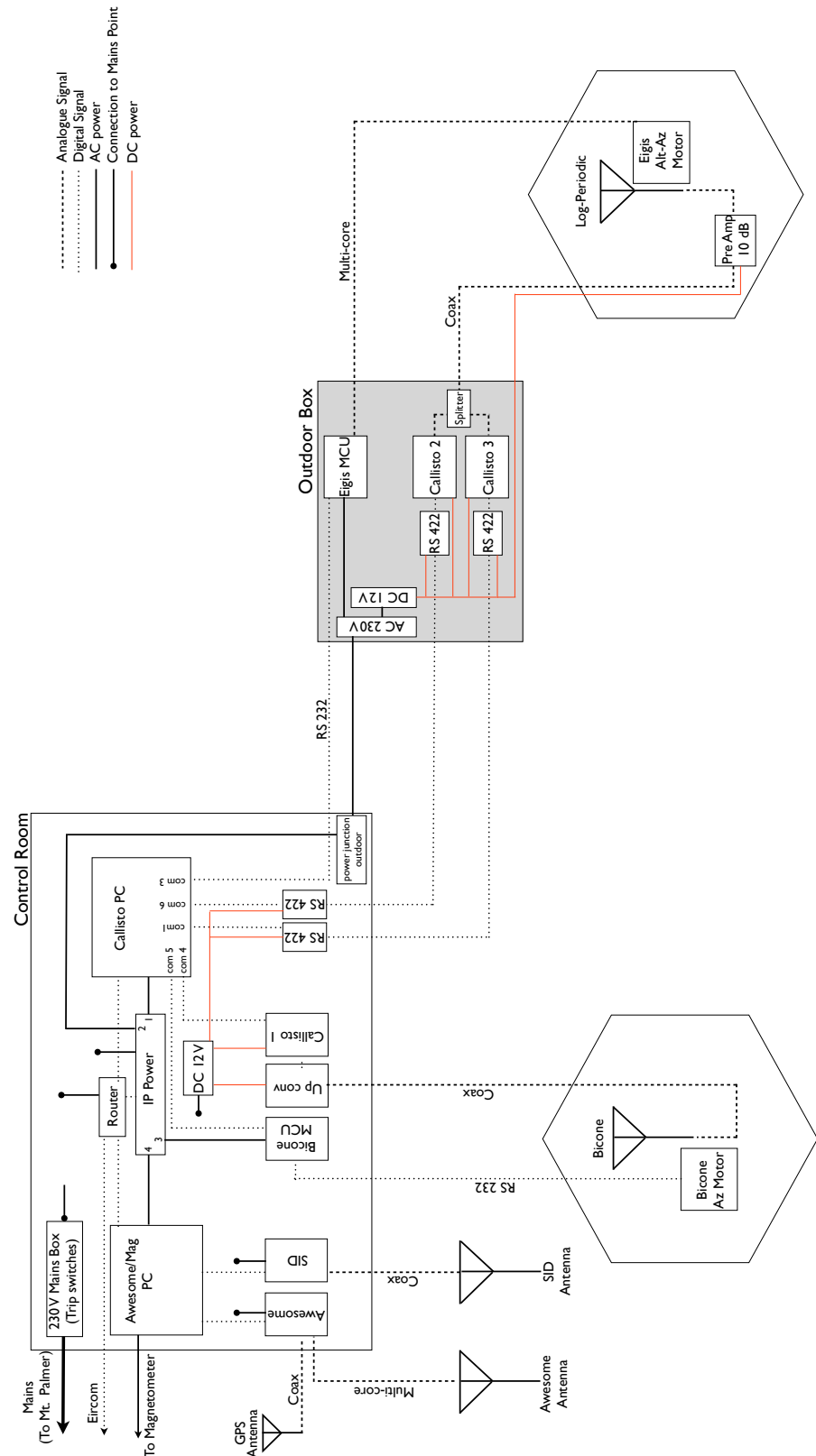


Figure 1.20: The Rosse Solar Terrestrial Observatory instrument and communications lay-out.

### 1.3.4.2 Nominal Operations

The system is controlled by a Dell Vostro, Intel core i5, allowing the system to be completely automated and stand alone, without the need for an on-site observer. Automatic nominal daily operations include (i) commence data recording of all three Callistas at 04:00 UT, (ii) begin antenna solar tracking at sunrise, (iii) at 10 minutes past every hour the data is processed, background subtracted, and images are produced for online display at [www.rosseobservatory.ie](http://www.rosseobservatory.ie), (iv) at mid-day a high frequency resolution (62.5 kHz) spectrum is taken, (v) stop solar tracking at sunset, (vi) archive the data products of the entire day (archive accessible online). The entire automated process is carried out by a combination of Callisto (Graphical USer Interfaces) GUIs, dedicated solar tracking GUIs, Microsoft Disk Operating System (MS-DOS) Shell scripts, and Interactive Data Language (IDL) scripts. This fully automated system is stable and requires maintenance or check up only every 6 or more months. If the system stops recording data, remote recovery can be achieved via a virtual desktop. The entire system is remotely accessible from Trinity College Dublin via a virtual desktop ‘VNC’ software. The system may be remotely configured and nominal operations changed at any time. Should the system crash, a remote power recycling facility is available using an IP power board with its own web address, accessible from any web browser. Automated steps (i)-(vi) are recovered and begin automatically upon power recycling.

### 1.3.4.3 eCallisto Network

RSTO is part of the e-Callisto network<sup>1</sup>. The network consists of a number of spectrometers located around the globe, and designed to monitor solar radio

---

<sup>1</sup>[www.e-callisto.org](http://www.e-callisto.org)

### 1.3 Radio Observations

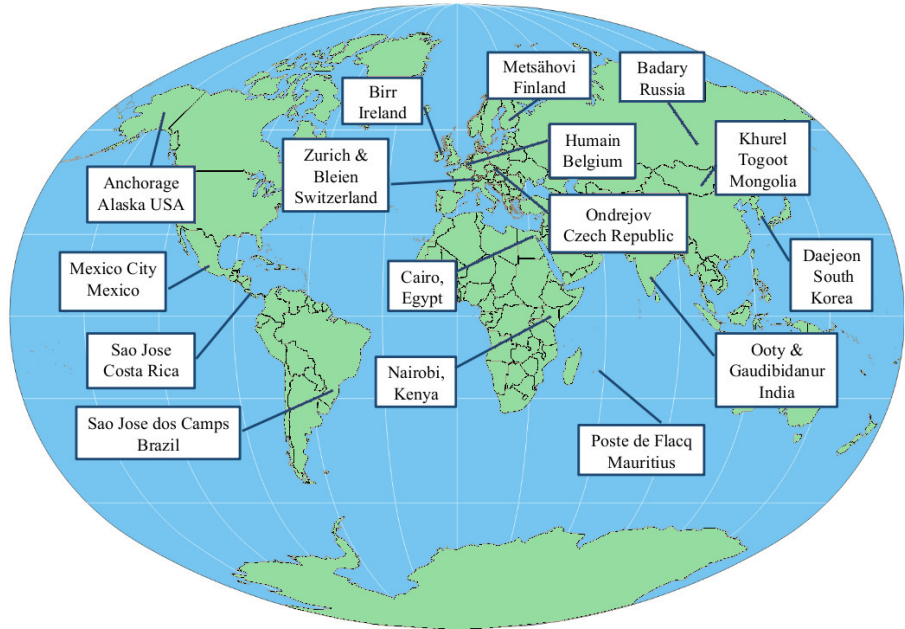


**Figure 1.21:** Worldwide distribution of Callisto sites, offering almost 24 coverage of solar radio activity at most latitudes (Zucca *et al.*, 2012).

emission in the meter and decameter bands (Benz *et al.* 2009; Figure 3.21). Each of the instruments observes automatically, and data is collected each day via the Internet and stored in a central database at Fachhochschule Nordwestschweiz (FHNW), and operated by ETH Zurich<sup>1</sup>. One of the important features of RSTO is the particularly low radio frequency interference (RFI) of the site.

To compare RSTO to other radio observing sites, a survey of RFI at RSTO was performed in June 2009. The detected spectrum is shown in Figure 3.22. A commercial DVB-T antenna covering the range from 20 MHz up to 900 MHz was used for the survey, which was directly connected via a low-loss coaxial cable to a Callisto receiver with a sensitivity of 25 mV/dB. The channel resolution was 62.5 kHz, while the radiometric bandwidth was about 300 kHz. The sampling

<sup>1</sup>[soleil.i4ds.ch/solarradio/CALLISTOQuicklooks/](http://soleil.i4ds.ch/solarradio/CALLISTOQuicklooks/)

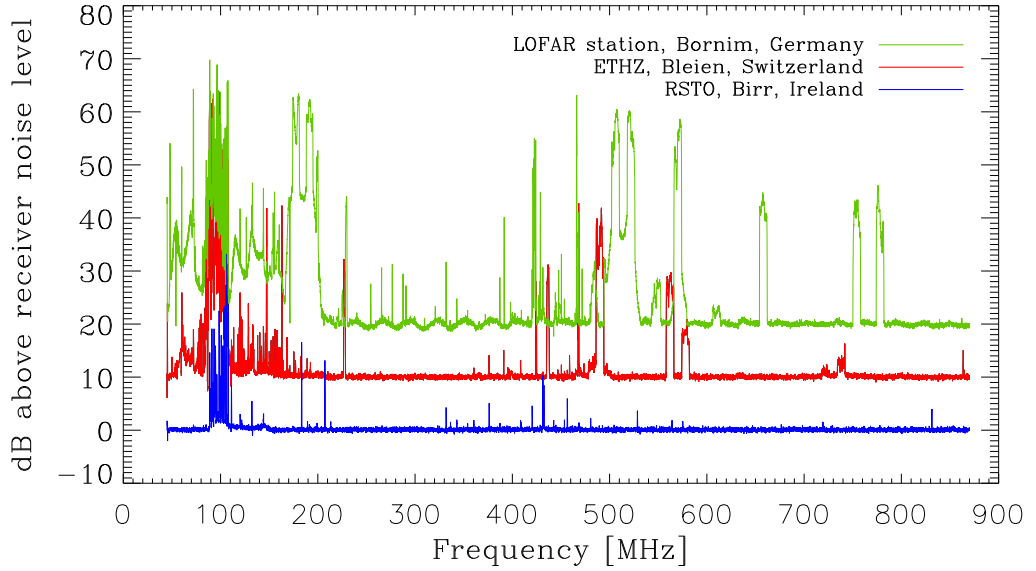


**Figure 1.22:** Radio frequency survey from the RSTO in Birr Castle Demesne (blue), Bleien Radio Observatory in Switzerland (red; offset by 10 dB) and Potsdam Bornim (green; offset by 20 dB). The RSTO spectrum is quiet at all frequencies that were tested, except for the FM band covering 88–108 MHz. The surveys were conducted using the same equipment (Zucca *et al.*, 2012).

time was 1.25 ms per frequency interval, while the integration time was about 1 ms. Figure 3.22 shows the RFI radio surveys of RSTO, Bleien Observatory in Switzerland, and the Potsdam LOFAR station in Germany. There is an high level of interference at 20–200 MHz for the Bleien and Potsdam sites, while the RSTO site has a low level of RFI.

#### 1.3.4.4 Dynamic spectra from RSTO

Since the installation of RSTO in September 2010 there has been a number radio bursts detected. The burst vary in their type, duration, and level of fine structure. The observatory has been successful in picking up type I storms, type IIs, type IIIs, a number of herringbone observations, and type IV and V. Some samples of

### 1.3 Radio Observations

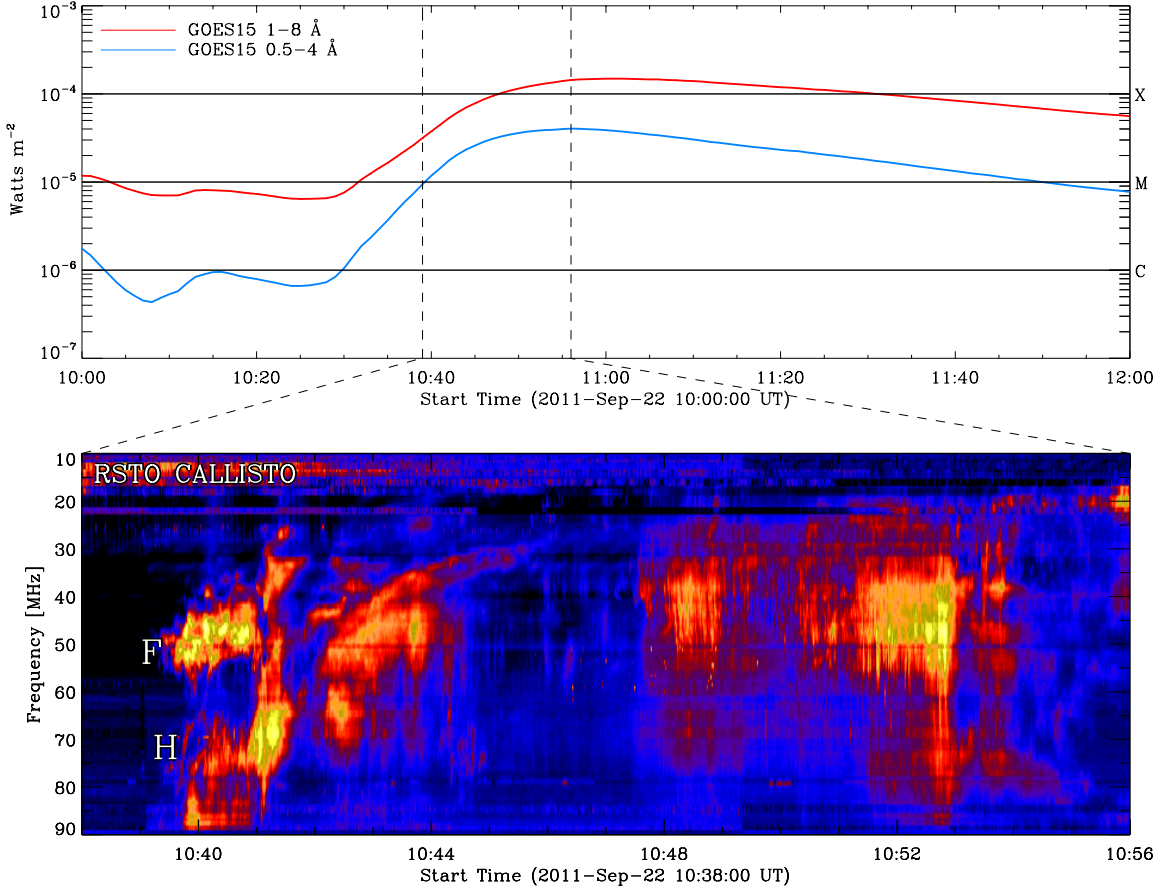


**Figure 1.23:** A radio burst from 22 September 2011 observed at RSTO. This radio burst was detected by the 10–100 MHz Callisto fed by the bicone antenna. The radio burst was quite complex, consisting of the fundamental and harmonic of a type II burst followed by herringbone fine structures. The top plot shows the GOES light curves for comparison, with the dashed vertical line indicating start and end times of the dynamic spectra. Adapted from (Zucca *et al.*, 2012)

these are given in Figures 3.23–3.25, and Appendix A.3.

#### 1.3.5 Dynamic Spectra Data Reduction

The Nançay Decametric Array, STEREO WAVES, and the Callisto spectrometers each have basic data reduction techniques in common. The most basic of these is background subtraction. Analogous to the dark current on a CCD, there will be

### 1.3 Radio Observations

---

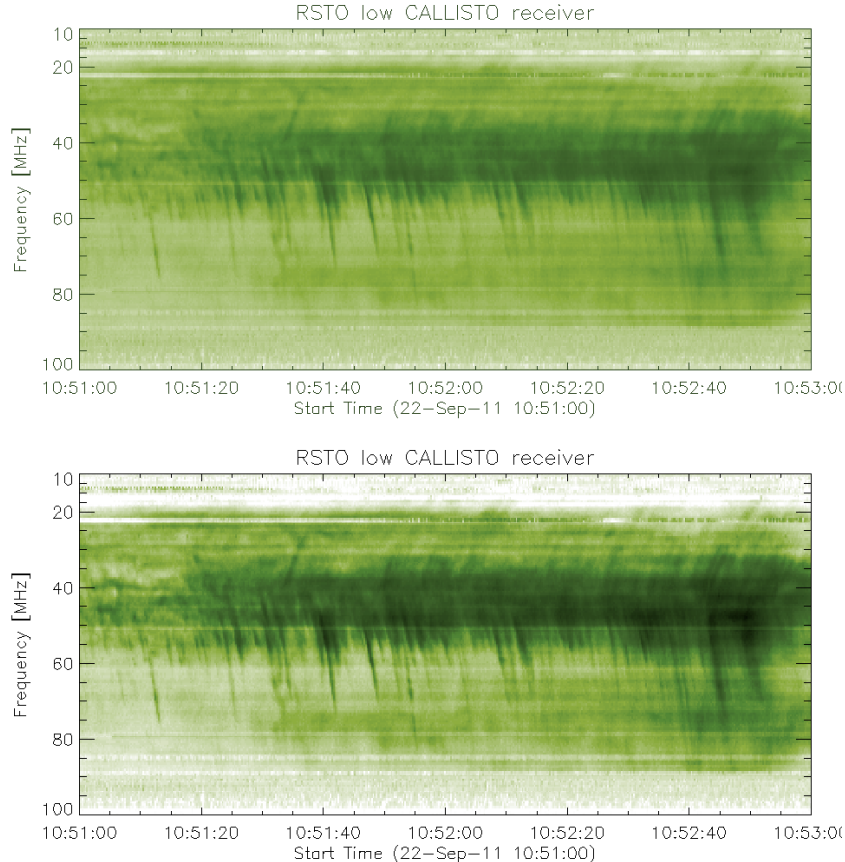


**Figure 1.24:** (Top) A zoom of the herringbone structure shown in Figure 3.23. The time sampling of the Callisto spectrometers (0.25 s) is fast enough to catch such herringbone features. (Bottom) Same spectrum but background subtracted, the herringbones have a much better contrast in this spectrum.

some background signal detected due to any DC bias or noise produced by the system thermal properties. This background may be subtracted by a variety of techniques, such as averaging the dynamic spectrum through time and using this as a background, subtracting a spectrum occurring just before a detected radio burst, or automatically detecting a spectra with no radio burst and using this as a background. The last type is the one implemented on the dynamic spectra used in this thesis work. The procedure is implemented in the IDL procedure *constbacksub.pro*. This function firstly computes the average of each frequency channel in time and subtracts this from the original dynamic spectrum. It then

### 1.3 Radio Observations

---

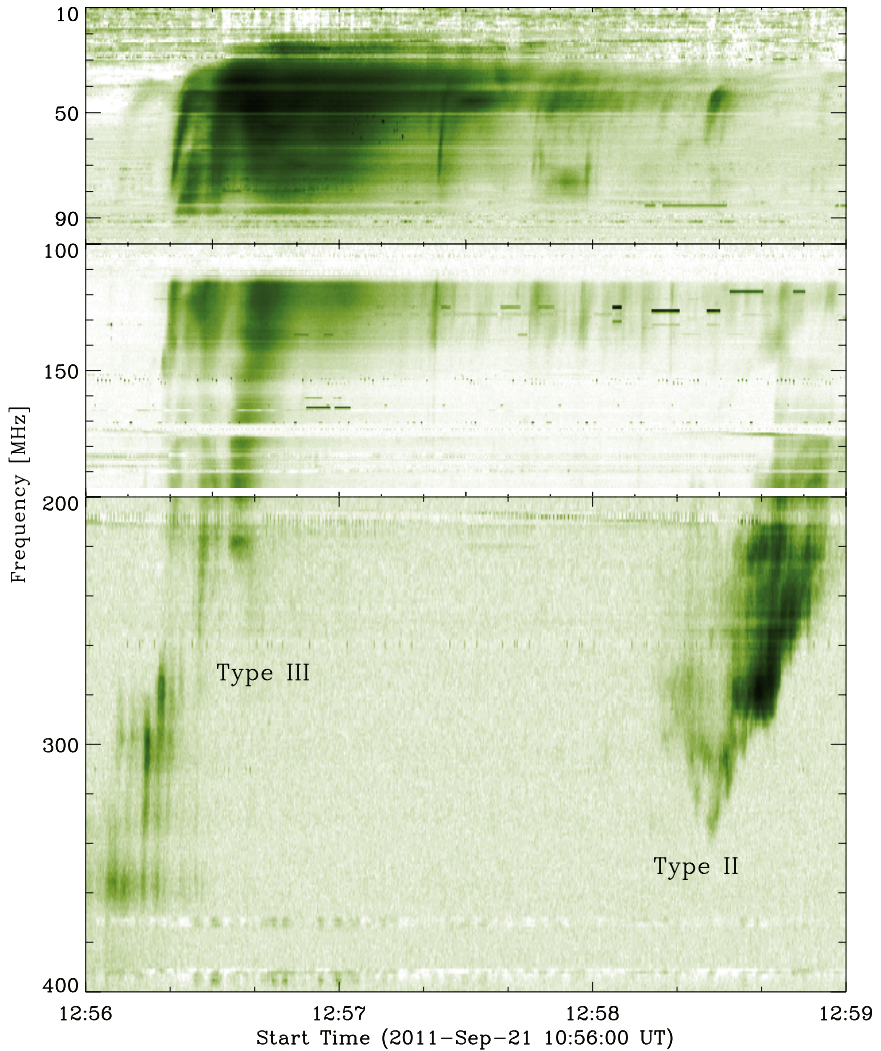


**Figure 1.25:** A type III and II radio burst observed on 21 September 2011. This spectra demonstrates the low levels of RFI at RSTO, especially in the 200–400 MHz range where there is almost no RFI (Zucca *et al.*, 2012).

computes the standard deviation of each time-step. The time-steps containing a radioburst should have the largest standard deviation, while those without a burst will have small standard deviation. By default the smallest 5% of the standard deviations is averaged and used as a background. An example of raw and background subtracted data is shown in Figure 3.24.

Dynamic spectra may also be contaminated by radio frequency interference (RFI). This may be sporadic, periodic and regular, or continuous in time. RFI is

### **1.3 Radio Observations**

---

generally very difficult to remove from a dynamic spectra while still maintaining the desired signal (radio burst). The techniques of RFI removal may be a simple smoothing of the data or convolution with a Gaussian to ‘average out’ the signal. Much more sophisticated RFI identification algorithms are based on multiscale filtering of the dynamic spectra image or using a kurtosis estimator (Nita & Gary, 2010; Nita *et al.*, 2007)(RFI is generally much more ‘peaked’ in either frequency or time). Generally, frequency channels which are badly contaminated by RFI are avoided if possible.

# A

## Appendix

### A.1 Radio Burst Emissivity

The full equations for emissivity of EM waves from the stochastic growth theory are

$$j_M(r) \approx \frac{\Phi_M}{\Delta\Omega_M} \frac{n_b m_e v_b^3}{3l(r)} \frac{\Delta v_b}{v_b} \quad (\text{A.1})$$

$$\Phi_F \approx 72\sqrt{3} \frac{\gamma_{L'}}{\gamma_S} \frac{v_e^3}{c^3} \frac{v_b}{\Delta v_b} \frac{e^{-u_c^2}}{u_c \sqrt{\pi}} \zeta_F \quad (\text{A.2})$$

$$\Phi_H \approx \frac{18\sqrt{3}}{5\gamma_t} \sqrt{\frac{m_i}{\gamma_t m_e}} \frac{v_e^3 v_b^3}{c^5} \frac{v_b}{\Delta v_b} \zeta_H \quad (\text{A.3})$$

the expression involving  $u_c$  represent an ‘escape factor’ for the fundamental taking into account absorption and scattering of the radiation.  $\frac{\gamma_{L'}}{\gamma_S}$  is the ratio of the damping rates of the product waves. The  $\zeta$  terms are the fractions of Langmuir waves that are kinematically able to contribute to the fundamental or harmonic

## A.2 EUV and pB Density Measurements

---

emission, given by

$$\zeta_F \approx \exp \left[ -\frac{4\gamma_t m_e}{45m_i} \left( \frac{v_b}{\Delta v_b} \right)^2 \left( \frac{3}{2} \sqrt{\frac{m_i}{\gamma_t m_e}} - \frac{v_b}{v_e} \right)^2 \right] \quad (\text{A.4})$$

$$\zeta_H \approx \frac{c}{2v_b} \sqrt{\frac{\pi}{6}} \frac{\beta \Delta v_b}{v_b} \left[ \operatorname{erf} \left( \frac{\frac{v_e \sqrt{3}}{c} + \frac{2}{3} \sqrt{\frac{\gamma_t m_e}{m_i}}}{\frac{v_e \beta \Delta v_b}{v_b} \sqrt{2}} \right) + \operatorname{erf} \left( \frac{\frac{v_e \sqrt{3}}{c} - \frac{2}{3} \sqrt{\frac{\gamma_t m_e}{m_i}}}{\frac{v_e \beta \Delta v_b}{v_b} \sqrt{2}} \right) \right] \quad (\text{A.5})$$

where  $\operatorname{erf}$  is the error function (Robinson & Cairns, 1993, 1998).

## A.2 EUV and pB Density Measurements

Electron densities were calculated from emission measure maps derived using the SDO/AIAs six coronal filters and the method of (Aschwanden *et al.*, 2013). The method starts by reconstructing the differential emission measure (DEM)  $dEM/dT$ , using the intensity of the six SDO/AIA filters for each pixel. The DEM is a measure of the amount of plasma along the line-of-sight (LOS) that contributes to the emitted radiation in the temperature range  $T$  to  $T + dT$  (Craig & Brown, 1976). Once the EM was obtained, the plasma electron density can be calculated estimating an effective length of the LOS of the emitting plasma. The 2D  $EM(r, \phi)$  map, which is a function of heliocentric distance  $r$  and latitude, can then be written as

$$EM(r, \phi) = \int \left( \frac{dEM(r, \phi)}{dT} \right) dT \quad (\text{A.6})$$

$$= \int < N_e^2 > ds \quad (\text{A.7})$$

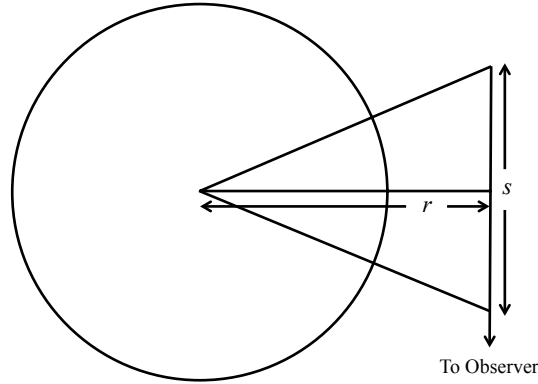


**Figure A.1:** The geometry for the emitting solar atmosphere LOS length. The observer measures the contribution of the plasma emitting along the path  $s$ , which varies with the heliocentric distance  $r$

Knowing the line-of-sight length,  $s$ , the density of the emitting plasma can be obtained from the EM,

$$N_e(r, \phi) = \sqrt{\frac{EM(r, \phi)}{s(r)}} \quad (\text{A.8})$$

The LOS length was calculated using a geometrical method used widely in stellar atmospheres (Menzel, 1936). The LOS length  $s$  changes at different distance  $r$  and contributes to the intensity of the emitting plasma measured by the observer (Figure A.1). This gives the LOS using an asymptotic series expansion in the form

$$S \approx \sqrt{H\pi r} \quad (\text{A.9})$$

where  $H$  is the scale height. Using a typical coronal temperature of 2 MK the scale height  $H$  is of the order of  $9 \times 10^9$  cm and the LOS is in the order of  $4 \times 10^{10}$  cm. The LOS length does not change significantly in the  $1-1.3 R_\odot$  range.

### A.3 June 7th 2011 Radio Burst from RSTO

---

As for the polarized brightness measurements, the density diagnostic is through the use of coronagraph images and the Thomson scattering theory outlined in Chapter 4. The method involves using the coronagraph data to extract polarized brightness measurements as a function of height i.e., along a radial trace in the coronagraph images. A polynomial is then fit to this data

$$I_t - I_r = \sum_s k_s x^{-s} \quad (\text{A.10})$$

where  $I_t - I_r$  is the polarized brightness, and  $x$  is the radial position in the corona,  $r$ , projected onto the plane of sky. van de Hulst (1950) showed that by use of the van de Hulst coefficients the electron density along the same radial trace can be expressed as

$$N(r) = \frac{1}{C\{A(r) - B(r)\}} \sum_s \frac{k_s}{a_{s+1}} r^{-s} \quad \text{where} \quad a_n = \frac{\pi}{2^{n+1}} \frac{n!}{(1/2n!)^2} \quad (\text{A.11})$$

here  $C$  is constant equal to  $\frac{3}{4} \times 1R_\odot \times \sigma_T$ ;  $\sigma_T$  is the Thomson scattering cross section and  $A(r)$  and  $B(r)$  are the van de Hulst coefficients (see Chapter 4). Here, the same  $k_s$  produced from the polarized brightness fit are used to calculate  $N(r)$ .

## A.3 June 7th 2011 Radio Burst from RSTO

The event of 7 June 2011 was an extremely complex eruption with a variety of associated radio activity (Figure A.2). The Callisto receivers at RSTO observed type II, type III, herringbones, and type IV. Also accompanying this activity was interplanetary type III bursts observed by STEREO WAVES in both Ahead and Behind spacecraft.

### A.3 June 7th 2011 Radio Burst from RSTO

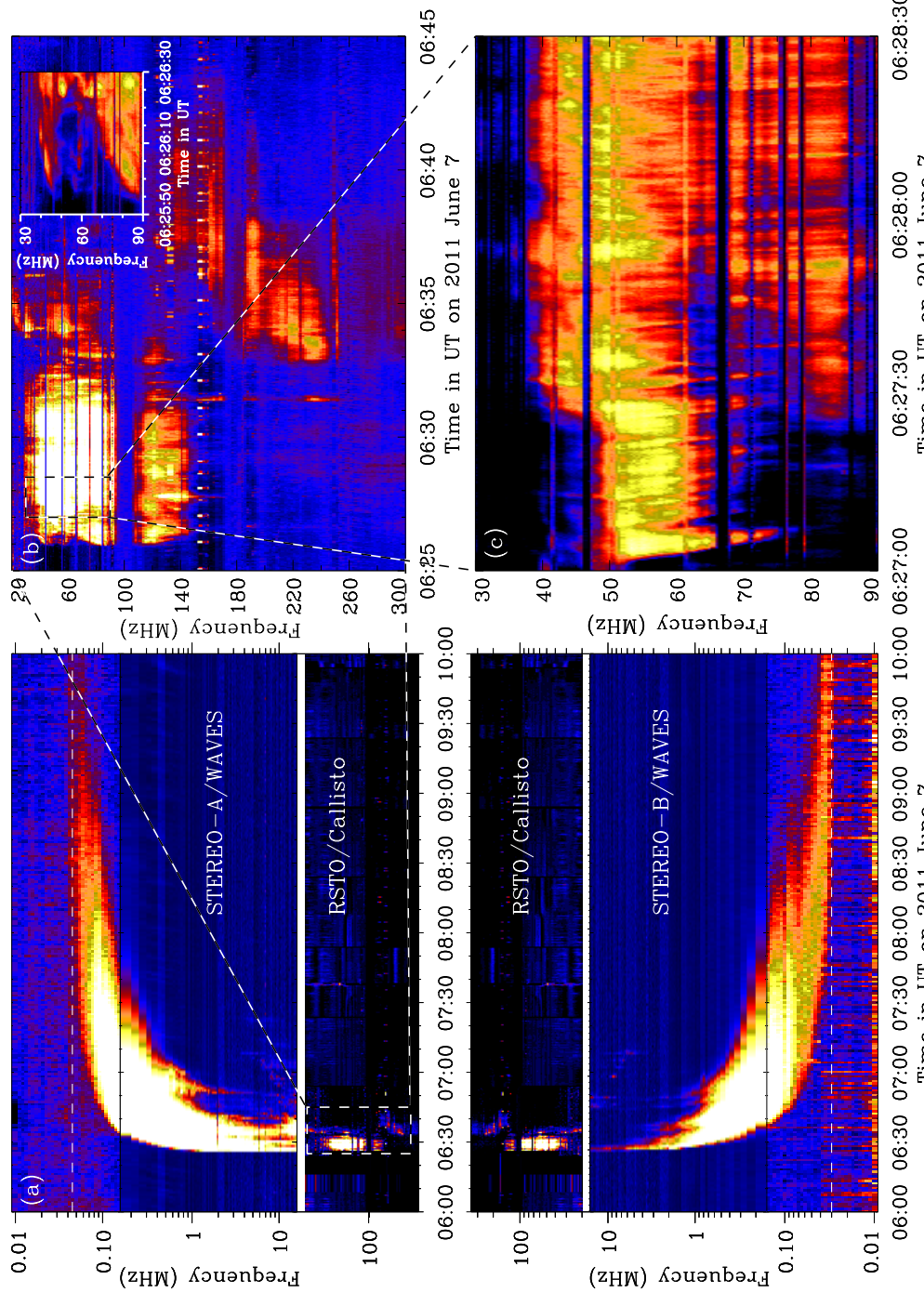


**Figure A.2:** Radio activity detected by STEREO WAVES A and B and RSTO callisto spectrometers, observed on 7 June 2011. The radio activity was complex, with interplanetary type IIIIs (a), a possible type II (inset of b), herringbones (c), and type IV (b).

## References

- ALLEN, C.W. (1947). Solar Radio-Noise of 200 Mc. /s. and its relation to Solar Observations. *Monthly Notices of the Royal Astronomical Society*, **107**, 386. (Cited on pages 37 and 97.)
- ALY, J.J. (1991). How much energy can be stored in a three-dimensional force-free magnetic field? *Astrophysical Journal Letters*, **375**, L61–L64. (Cited on page 70.)
- ANTIOCHOS, S.K., DEVORE, C.R. & KLIMCHUK, J.A. (1999a). A Model for Solar Coronal Mass Ejections. *Astrophysical Journal*, **510**, 485–493. (Cited on pages 65 and 69.)
- ANTIOCHOS, S.K., DEVORE, C.R. & KLIMCHUK, J.A. (1999b). A Model for Solar Coronal Mass Ejections. *Astrophysical Journal*, **510**, 485–493. (Cited on pages 140 and 165.)
- ASCHWANDEN, M.J. (2004). *Physics of the Solar Corona. An Introduction*. Praxis Publishing Ltd. (Cited on pages 13 and 63.)
- ASCHWANDEN, M.J., NITTA, N.V., WUELTER, J.P., LEMEN, J.R., SANDMAN, A., VOURLIDAS, A. & COLANINNO, R.C. (2009). First Measurements of the Mass of Coronal Mass Ejections from the EUV Dimming Observed with STEREO EUVI A+B Spacecraft. *Astrophysical Journal*, **706**, 376–392. (Cited on pages 28, 162, 210, 211, 212 and 213.)
- ASCHWANDEN, M.J., BOERNER, P., SCHRIJVER, C.J. & MALANUSHENKO, A. (2013). Automated Temperature and Emission Measure Analysis of Coronal Loops and Active Regions Observed with the Atmospheric Imaging Assembly on the Solar Dynamics Observatory (SDO/AIA). *Solar Physics*, **283**, 5–30. (Cited on pages 177 and 229.)

## REFERENCES

---

- ATTRILL, G.D.R., HARRA, L.K., VAN DRIEL-GESZTELYI, L. & DÉMOULIN, P. (2007). Coronal “Wave”: Magnetic Footprint of a Coronal Mass Ejection? *Astrophysical Journal Letters*, **656**, L101–L104. (Cited on page 48.)
- AURASS, H. & MANN, G. (2004). Radio Observation of Electron Acceleration at Solar Flare Reconnection Outflow Termination Shocks. *Astrophysical Journal*, **615**, 526–530. (Cited on pages 44 and 196.)
- AURASS, H., VRŠNAK, B. & MANN, G. (2002). Shock-excited radio burst from reconnection outflow jet? *Astronomy & Astrophysics*, **384**, 273–281. (Cited on page 44.)
- AVIGNON, Y., BONMARTIN, J., BOUTEILLE, A., CLAELIER, B. & HULOT, E. (1989). The mark IV Nancay Radioheliograph. *Solar Physics*, **120**, 193–204. (Cited on pages 120 and 121.)
- BABCOCK, H.W. (1961). The Topology of the Sun’s Magnetic Field and the 22-YEAR Cycle. *Astrophysical Journal*, **133**, 572. (Cited on page 9.)
- BAIN, H.M., KRUCKER, S., GLESENER, L. & LIN, R.P. (2012). Radio Imaging of Shock-accelerated Electrons Associated with an Erupting Plasmoid on 2010 November 3. *Astrophysical Journal*, **750**, 44. (Cited on pages 39 and 194.)
- BALE, S.D., ULLRICH, R., GOETZ, K., ALSTER, N., CECCONI, B., DEKKALI, M., LINGNER, N.R., MACHER, W., MANNING, R.E., McCUALEY, J., MONSON, S.J., OSWALD, T.H. & PULUPA, M. (2008). The Electric Antennas for the STEREO/WAVES Experiment. *Space Science Reviews*, **136**, 529–547. (Cited on page 126.)
- BALFOUR, S. (1861). On the Great Magnetic Disturbance Which Extended from August 28 to September 7, 1859, as Recorded by Photography at the Kew Observatory. *Philosophical Transactions of the Royal Society of London*, **151**, 423. (Cited on page 19.)
- BALL, L. & MELROSE, D.B. (2001). Shock Drift Acceleration of Electrons. *Publications of the Astronomical Society of Australia*, **18**, 361–373. (Cited on pages 77, 82, 84, 85 and 194.)
- BASTIAN, T.S., PICK, M., KERDRAON, A., MAIA, D. & VOURLIDAS, A. (2001). The Coronal Mass Ejection of 1998 April 20: Direct Imaging at Radio Wavelengths. *Astrophysical Journal Letters*, **558**, L65–L69. (Cited on page 34.)

---

## REFERENCES

- BEIN, B.M., BERKEBILE-STOISER, S., VERONIG, A.M., TEMMER, M., MUHR, N., KIENREICH, I., UTZ, D. & VRŠNAK, B. (2011). Impulsive Acceleration of Coronal Mass Ejections. I. Statistics and Coronal Mass Ejection Source Region Characteristics. *Astrophysical Journal*, **738**, 191. (Cited on pages 33, 34, 165, 167, 168 and 200.)
- BEMPORAD, A. & MANCUSO, S. (2010). First Complete Determination of Plasma Physical Parameters Across a Coronal Mass Ejection-driven Shock. *Astrophysical Journal*, **720**, 130–143. (Cited on page 42.)
- BENZ, A.O., MONSTEIN, C. & MEYER, H. (2005). Callisto A New Concept for Solar Radio Spectrometers. *Solar Physics*, **226**, 143–151. (Cited on pages 128 and 130.)
- BENZ, A.O., MONSTEIN, C., MEYER, H., MANOHARAN, P.K., RAMESH, R., ALTYNTSEV, A., LARA, A., PAEZ, J. & CHO, K.S. (2009). A World-Wide Net of Solar Radio Spectrometers: e-CALLISTO. *Earth Moon and Planets*, **104**, 277–285. (Cited on page 133.)
- BIESECKER, D.A., MYERS, D.C., THOMPSON, B.J., HAMMER, D.M. & VOURLIDAS, A. (2002). Solar Phenomena Associated with “EIT Waves”. *Astrophysical Journal*, **569**, 1009–1015. (Cited on page 46.)
- BILLINGS, D.E. (1966a). *A guide to the solar corona*. (Cited on pages 114 and 149.)
- BILLINGS, D.E. (1966b). *A guide to the solar corona*. (Cited on page 141.)
- BOISCHOT, A., ROSOLEN, C., AUBIER, M.G., DAIGNE, G., GENOVA, F., LEBLANC, Y., LECACHEUX, A., DE LA NOE, J. & MOLLER-PEDERSEN, B. (1980). A new high-gain, broadband, steerable array to study Jovian decametric emission. *ICARUS*, **43**, 399–407. (Cited on page 125.)
- BONMARTIN, J., BOUTEILLE, A., CLAELIER, B., ISSARTEL, M.P., KERDRAON, A., LANTOS, M.F., LANTOS, P., MERCIER, C., PICK, M. & RAOULT, A. (1983). The Mark III Nancay Radioheliograph. *Solar Physics*, **88**, 383–390. (Cited on page 120.)
- BOUGERET, J.L., KAISER, M.L., KELLOGG, P.J., MANNING, R., GOETZ, K., MONSON, S.J., MONGE, N., FRIEL, L., MEETRE, C.A., PERCHE, C., SITRUK, L. & HOANG, S. (1995). Waves: The Radio and Plasma Wave Investigation on the Wind Spacecraft. *Space Science Reviews*, **71**, 231–263. (Cited on page 126.)

---

## REFERENCES

- BOUGERET, J.L., ZARKA, P., CAROUBALOS, C., KARLICKÝ, M., LEBLANC, Y., MAROULIS, D., HILLARIS, A., MOUSSAS, X., ALISSANDRAKIS, C.E., DUMAS, G. & PERCHE, C. (1998). A shock associated (SA) radio event and related phenomena observed from the base of the solar corona to 1 AU. *Geophysical Research Letters*, **25**, 2513–2516. (Cited on page 44.)
- BOUGERET, J.L., GOETZ, K., KAISER, M.L., BALE, S.D., KELLOGG, P.J., MAKSIMOVIC, M., MONGE, N., MONSON, S.J., ASTIER, P.L., DAVY, S., DEKKALI, M., HINZE, J.J., MANNING, R.E., AGUILAR-RODRIGUEZ, E., BONNIN, X., BRIAND, C., CAIRNS, I.H., CATTELL, C.A., CECCONI, B., EASTWOOD, J., ERGUN, R.E., FAINBERG, J., HOANG, S., HUTTUNEN, K.E.J., KRUCKER, S., LECACHEUX, A., MACDOWALL, R.J., MACHER, W., MANGENEY, A., MEETRE, C.A., MOUSSAS, X., NGUYEN, Q.N., OSWALD, T.H., PULUPA, M., REINER, M.J., ROBINSON, P.A., RUCKER, H., SALEM, C., SANTOLIK, O., SILVIS, J.M., ULLRICH, R., ZARKA, P. & ZOGANELIS, I. (2008). S/WAVES: The Radio and Plasma Wave Investigation on the STEREO Mission. *Space Science Reviews*, **136**, 487–528. (Cited on page 126.)
- BOURSIER, Y., LAMY, P., LLEBARIA, A., GOUDAIL, F. & ROBELUS, S. (2009). The ARTEMIS Catalog of LASCO Coronal Mass Ejections. Automatic Recognition of Transient Events and Marseille Inventory from Synoptic maps. *Solar Physics*, **257**, 125–147. (Cited on page 201.)
- BOUVIER, A. & WADHWA, M. (2010). The age of the Solar System redefined by the oldest Pb-Pb age of a meteoritic inclusion. *Nature Geoscience*, **3**, 637–641. (Cited on page 2.)
- BRUECKNER, G.E., HOWARD, R.A., KOOMEN, M.J., KORENDYKE, C.M., MICHELS, D.J., MOSES, J.D., SOCKER, D.G., DERE, K.P., LAMY, P.L., LLEBARIA, A., BOUT, M.V., SCHWENN, R., SIMNETT, G.M., BEDFORD, D.K. & EYLES, C.J. (1995). The Large Angle Spectroscopic Coronagraph (LASCO). *Solar Physics*, **162**, 357–402. (Cited on pages 102, 103, 104, 105 and 112.)
- BURGESS, D. (2006). Simulations of Electron Acceleration at Collisionless Shocks: The Effects of Surface Fluctuations. *Astrophysical Journal*, **653**, 316–324. (Cited on pages 189, 195 and 196.)

## REFERENCES

---

- BURKEPILE, J.T., HUNDHAUSEN, A.J., STANGER, A.L., ST. CYR, O.C. & SEIDEN, J.A. (2004). Role of projection effects on solar coronal mass ejection properties: 1. A study of CMEs associated with limb activity. *Journal of Geophysical Research (Space Physics)*, **109**, 3103. (Cited on pages 21 and 22.)
- BYRNE, J.P., MALONEY, S.A., MCATEER, R.T.J., REFOJO, J.M. & GALLAGHER, P.T. (2010). Propagation of an Earth-directed coronal mass ejection in three dimensions. *Nature Communications*, **1**. (Cited on pages 22, 141, 157, 158, 162, 163, 165, 166, 168, 192 and 193.)
- BYRNE, J.P., MORGAN, H., HABBAL, S.R. & GALLAGHER, P.T. (2012). Automatic Detection and Tracking of Coronal Mass Ejections. II. Multiscale Filtering of Coronagraph Images. *Astrophysical Journal*, **752**, 145. (Cited on page 202.)
- CAIRNS, I.H. & ROBINSON, R.D. (1987). Herringbone bursts associated with type II solar radio emission. *Solar Physics*, **111**, 365–383. (Cited on pages 43 and 226.)
- CAIRNS, I.H., KNOCK, S.A., ROBINSON, P.A. & KUNCIC, Z. (2003). Type II Solar Radio Bursts: Theory and Space Weather Implications. *Space Science Reviews*, **107**, 27–34. (Cited on page 93.)
- CANE, H.V. & ERICKSON, W.C. (2005). Solar Type II Radio Bursts and IP Type II Events. *Astrophysical Journal*, **623**, 1180–1194. (Cited on page 41.)
- CANE, H.V. & WHITE, S.M. (1989). On the source conditions for herringbone structure in type II solar radio bursts. *Solar Physics*, **120**, 137–144. (Cited on page 43.)
- CARGILL, P.J. (2004). On the Aerodynamic Drag Force Acting on Interplanetary Coronal Mass Ejections. *Solar Physics*, **221**, 135–149. (Cited on page 32.)
- CARLEY, E.P., MCATEER, R.T.J. & GALLAGHER, P.T. (2012). Coronal Mass Ejection Mass, Energy, and Force Estimates Using STEREO. *Astrophysical Journal*, **752**, 36. (Cited on pages 144, 145, 160 and 163.)
- CARLSSON, M. & STEIN, R.F. (1997). Formation of Solar Calcium H and K Bright Grains. *Astrophysical Journal*, **481**, 500. (Cited on page 13.)

## REFERENCES

---

- CARMICHAEL, H. (1964). A Process for Flares. *NASA Special Publication*, **50**, 451. (Cited on page 44.)
- CARRINGTON, R.C. (1859). Description of a Singular Appearance seen in the Sun on September 1, 1859. *Monthly Notices of the Royal Astronomical Society*, **20**, 13–15. (Cited on page 19.)
- CHAPMAN, S. & FERRARO, V.C.A. (1930). A New Theory of Magnetic Storms. *Nature*, **126**, 129–130. (Cited on page 19.)
- CHARBONNEAU, P. (2010). Dynamo Models of the Solar Cycle. *Living Reviews in Solar Physics*, **7**, 3. (Cited on page 9.)
- CHEN, J. (1989). Effects of toroidal forces in current loops embedded in a background plasma. *Astrophysical Journal*, **338**, 453–470. (Cited on pages 65, 71, 72 and 74.)
- CHEN, J. (1996). Theory of prominence eruption and propagation: Interplanetary consequences. *Journal of Geophysical Research*, **1012**, 27499–27520. (Cited on pages 140, 166 and 201.)
- CHEN, J., MARQUÉ, C., VOURLIDAS, A., KRALL, J. & SCHUCK, P.W. (2006). The Flux-Rope Scaling of the Acceleration of Coronal Mass Ejections and Eruptive Prominences. *Astrophysical Journal*, **649**, 452–463. (Cited on page 140.)
- CHEN, P.F., WU, S.T., SHIBATA, K. & FANG, C. (2002). Evidence of EIT and Moreton Waves in Numerical Simulations. *Astrophysical Journal Letters*, **572**, L99–L102. (Cited on page 48.)
- CHENG, X., ZHANG, J., OLMEDO, O., VOURLIDAS, A., DING, M.D. & LIU, Y. (2012). Investigation of the Formation and Separation of an Extreme-ultraviolet Wave from the Expansion of a Coronal Mass Ejection. *Astrophysical Journal Letters*, **745**, L5. (Cited on page 185.)
- CHO, K.S., LEE, J., MOON, Y.J., DRYER, M., BONG, S.C., KIM, Y.H. & PARK, Y.D. (2007). A study of CME and type II shock kinematics based on coronal density measurement. *Astronomy & Astrophysics*, **461**, 1121–1125. (Cited on page 40.)
- CHO, K.S., BONG, S.C., MOON, Y.J., SHANMUGARAJU, A., KWON, R.Y. & PARK, Y.D. (2011). Relationship between multiple type II solar radio bursts and CME observed by STEREO/SECCHI. *Astronomy & Astrophysics*, **530**, A16. (Cited on page 40.)

## REFERENCES

---

- CLASSEN, H.T. & AURASS, H. (2002). On the association between type II radio bursts and CMEs. *Astronomy & Astrophysics*, **384**, 1098–1106. (Cited on page 39.)
- COHEN, O., ATTRILL, G.D.R., MANCHESTER, W.B., IV & WILLS-DAVEY, M.J. (2009). Numerical Simulation of an EUV Coronal Wave Based on the 2009 February 13 CME Event Observed by STEREO. *Astrophysical Journal*, **705**, 587–602. (Cited on page 185.)
- COLANINNO, R.C. & VOURLIDAS, A. (2009). First Determination of the True Mass of Coronal Mass Ejections: A Novel Approach to Using the Two STEREO Viewpoints. *Astrophysical Journal*, **698**, 852–858. (Cited on pages 28, 142 and 161.)
- CRAIG, I.J.D. & BROWN, J.C. (1976). Fundamental limitations of X-ray spectra as diagnostics of plasma temperature structure. *Astronomy & Astrophysics*, **49**, 239–250. (Cited on page 229.)
- DAVIS, R., HARMER, D.S. & HOFFMAN, K.C. (1968). Search for Neutrinos from the Sun. *Physical Review Letters*, **20**, 1205–1209. (Cited on pages 3 and 4.)
- DE HOFFMANN, F. & TELLER, E. (1950). Magneto-Hydrodynamic Shocks. *Physical Review*, **80**, 692–703. (Cited on page 81.)
- DE KONING, C.A., PIZZO, V.J. & BIESECKER, D.A. (2009). Geometric Localization of CMEs in 3D Space Using STEREO Beacon Data: First Results. *Solar Physics*, **256**, 167–181. (Cited on page 22.)
- DE PONTIEU, B., ERDÉLYI, R. & JAMES, S.P. (2004). Solar chromospheric spicules from the leakage of photospheric oscillations and flows. *Nature*, **430**, 536–539. (Cited on page 13.)
- DELANNÉE, C., TÖRÖK, T., AULANIER, G. & HOCHÉDEZ, J.F. (2008). A New Model for Propagating Parts of EIT Waves: A Current Shell in a CME. *Solar Physics*, **247**, 123–150. (Cited on pages 48, 172 and 193.)
- DOMINGO, V., FLECK, B. & POLAND, A.I. (1995). The SOHO Mission: an Overview. *Solar Physics*, **162**, 1–37. (Cited on pages 20 and 102.)
- DOWNS, C., ROUSSEV, I.I., VAN DER HOLST, B., LUGAZ, N. & SOKOLOV, I.V. (2012). Understanding SDO/AIA Observations of the 2010 June 13 EUV Wave Event: Direct Insight

---

## REFERENCES

- from a Global Thermodynamic MHD Simulation. *Astrophysical Journal*, **750**, 134. (Cited on pages 183 and 185.)
- DUDA, R.O. & HART, P.E. (1972). Use of the hough transformation to detect lines and curves in pictures. *Commun. ACM*, **15**, 11–15. (Cited on page 218.)
- EMSLIE, A.G., KUCHAREK, H., DENNIS, B.R., GOPALSWAMY, N., HOLMAN, G.D., SHARE, G.H., VOURLIDAS, A., FORBES, T.G., GALLAGHER, P.T., MASON, G.M., METCALF, T.R., MEWALDT, R.A., MURPHY, R.J., SCHWARTZ, R.A. & ZURBUCHEN, T.H. (2004). Energy partition in two solar flare/CME events. *Journal of Geophysical Research (Space Physics)*, **109**, A10104. (Cited on pages 35, 164 and 168.)
- EMSLIE, A.G., DENNIS, B.R., SHIH, A.Y., CHAMBERLIN, P.C., MEWALDT, R.A., MOORE, C.S., SHARE, G.H., VOURLIDAS, A. & WELSCH, B.T. (2012). Global Energetics of Thirty-eight Large Solar Eruptive Events. *Astrophysical Journal*, **759**, 71. (Cited on page 35.)
- FAN, Y. (2005). Coronal Mass Ejections as Loss of Confinement of Kinked Magnetic Flux Ropes. *Astrophysical Journal*, **630**, 543–551. (Cited on page 65.)
- FAN, Y. (2009). Magnetic Fields in the Solar Convection Zone. *Living Reviews in Solar Physics*, **6**, 4. (Cited on page 10.)
- FELDMAN, W.C., ANDERSON, R.C., BAME, S.J., GARY, S.P., GOSLING, J.T., MCCOMAS, D.J., THOMSEN, M.F., PASCHMANN, G. & HOPPE, M.M. (1983). Electron velocity distributions near the earth's bow shock. *Journal of Geophysical Research*, **88**, 96–110. (Cited on page 83.)
- FENG, S.W., CHEN, Y., KONG, X.L., LI, G., SONG, H.Q., FENG, X.S. & LIU, Y. (2012). Radio Signatures of Coronal-mass-ejection-Streamer Interaction and Source Diagnostics of Type II Radio Burst. *Astrophysical Journal*, **753**, 21. (Cited on page 194.)
- FENG, S.W., CHEN, Y., KONG, X.L., LI, G., SONG, H.Q., FENG, X.S. & GUO, F. (2013). Diagnostics on the Source Properties of a Type II Radio Burst with Spectral Bumps. *Astrophysical Journal*, **767**, 29. (Cited on page 194.)
- FITZPATRICK, R. (2000). *The Physics of Plasmas*. (Not cited.)

## REFERENCES

---

- FONTENLA, J., REICHMANN, E.J. & TANDBERG-HANSSEN, E. (1988). The Lyman-alpha line in various solar features. I - Observations. *Astrophysical Journal*, **329**, 464–481. (Cited on pages 12, 13 and 14.)
- FORBES, T.G. & ISENBERG, P.A. (1991). A catastrophe mechanism for coronal mass ejections. *Astrophysical Journal*, **373**, 294–307. (Cited on pages 66, 140 and 165.)
- FORBES, T.G. & PRIEST, E.R. (1995). Photospheric Magnetic Field Evolution and Eruptive Flares. *Astrophysical Journal*, **446**, 377. (Cited on pages 65, 66, 67, 140 and 165.)
- FORBUSH, S.E. (1946). Three Unusual Cosmic-Ray Increases Possibly Due to Charged Particles from the Sun. *Physical Review*, **70**, 771–772. (Cited on page 19.)
- FOUKAL, P.V. (2004). *Solar Astrophysics, 2nd, Revised Edition*. Wiley-VCH. (Cited on pages 2 and 5.)
- GABRIEL, A.H. (1976). A magnetic model of the solar transition region. *Royal Society of London Philosophical Transactions Series A*, **281**, 339–352. (Cited on pages 12, 13 and 14.)
- GALLAGHER, P.T. & LONG, D.M. (2011). Large-scale Bright Fronts in the Solar Corona: A Review of "EIT waves". *Space Science Reviews*, **158**, 365–396. (Cited on pages 171 and 193.)
- GALLAGHER, P.T., LAWRENCE, G.R. & DENNIS, B.R. (2003). Rapid Acceleration of a Coronal Mass Ejection in the Low Corona and Implications for Propagation. *Astrophysical Journal Letters*, **588**, L53–L56. (Cited on pages 24, 25, 164 and 168.)
- GINZBURG, V.L. & ZHELEZNIAKOV, V.V. (1958). On the Possible Mechanisms of Sporadic Solar Radio Emission (Radiation in an Isotropic Plasma). *Soviet Astronomy*, **2**, 653. (Cited on page 92.)
- GOLD, T. (1962). Magnetic Storms. *Space Science Reviews*, **1**, 100–114. (Cited on page 20.)
- GOOSSENS, M., ed. (2003). *An introduction to plasma astrophysics and magnetohydrodynamics*, vol. 294 of *Astrophysics and Space Science Library*. (Cited on page 57.)
- GOPALSWAMY, N. & KUNDU, M.R. (1992). Estimation of the mass of a coronal mass ejection from radio observations. *Astrophysical Journal Letters*, **390**, L37–L39. (Cited on page 28.)

## REFERENCES

---

- GOPALSWAMY, N. & THOMPSON, B.J. (2000). Early life of coronal mass ejections. *Journal of Atmospheric and Solar-Terrestrial Physics*, **62**, 1457–1469. (Cited on pages 19, 22 and 24.)
- GOPALSWAMY, N., YASHIRO, S., MICHALEK, G., STENBORG, G., VOURLIDAS, A., FREELAND, S. & HOWARD, R. (2009a). The SOHO/LASCO CME Catalog. *Earth Moon and Planets*, **104**, 295–313. (Cited on page 201.)
- GOPALSWAMY, N., YASHIRO, S., TEMMER, M., DAVILA, J., THOMPSON, W.T., JONES, S., MCATEER, R.T.J., WUELTER, J.P., FREELAND, S. & HOWARD, R.A. (2009b). EUV Wave Reflection from a Coronal Hole. *Astrophysical Journal Letters*, **691**, L123–L127. (Cited on pages 46 and 171.)
- GOPALSWAMY, N., NITTA, N., AKIYAMA, S., MÄKELÄ, P. & YASHIRO, S. (2012). Coronal Magnetic Field Measurement from EUV Images Made by the Solar Dynamics Observatory. *Astrophysical Journal*, **744**, 72. (Cited on page 50.)
- GOSLING, J.T. (1993). The solar flare myth. *Journal of Geophysical Research*, **98**, 18937–18950. (Cited on page 66.)
- GOSLING, J.T., HILDNER, E., MACQUEEN, R.M., MUNRO, R.H., POLAND, A.I. & ROSS, C.L. (1976). The speeds of coronal mass ejection events. *Solar Physics*, **48**, 389–397. (Cited on page 39.)
- GRECHNEV, V.V., AFANASYEV, A.N., URALOV, A.M., CHERTOK, I.M., ESELEVICH, M.V., ESELEVICH, V.G., RUDENKO, G.V. & KUBO, Y. (2011a). Coronal Shock Waves, EUV Waves, and Their Relation to CMEs. III. Shock-Associated CME/EUV Wave in an Event with a Two-Component EUV Transient. *Solar Physics*, **273**, 461–477. (Cited on pages 47, 48 and 194.)
- GRECHNEV, V.V., URALOV, A.M., CHERTOK, I.M., KUZMENKO, I.V., AFANASYEV, A.N., MESHALKINA, N.S., KALASHNIKOV, S.S. & KUBO, Y. (2011b). Coronal Shock Waves, EUV Waves, and Their Relation to CMEs. I. Reconciliation of "EIT Waves", Type II Radio Bursts, and Leading Edges of CMEs. *Solar Physics*, **273**, 433–460. (Cited on pages 46, 171, 172 and 193.)

## REFERENCES

---

- GUO, F. & GIACALONE, J. (2010). The Effect of Large-scale Magnetic Turbulence on the Acceleration of Electrons by Perpendicular Collisionless Shocks. *Astrophysical Journal*, **715**, 406–411. (Cited on pages 43, 171, 189, 196 and 197.)
- GUO, F. & GIACALONE, J. (2012). Particle Acceleration at a Flare Termination Shock: Effect of Large-scale Magnetic Turbulence. *Astrophysical Journal*, **753**, 28. (Cited on page 195.)
- GURNETT, D.A., KURTH, W.S., KIRCHNER, D.L., HOSPODARSKY, G.B., AVERKAMP, T.F., ZARKA, P., LECACHEUX, A., MANNING, R., ROUX, A., CANU, P., CORNILLEAU-WEHRLIN, N., GALOPEAU, P., MEYER, A., BOSTRÖM, R., GUSTAFSSON, G., WAHLUND, J.E., ÅHLEN, L., RUCKER, H.O., LADREITER, H.P., MACHER, W., WOOLLISCROFT, L.J.C., ALLEYNE, H., KAISER, M.L., DESCH, M.D., FARRELL, W.M., HARVEY, C.C., LOUARN, P., KELLOGG, P.J., GOETZ, K. & PEDERSEN, A. (2004). The Cassini Radio and Plasma Wave Investigation. *Space Science Reviews*, **114**, 395–463. (Cited on page 126.)
- HEY, J.S. (1946). Solar Radiations in the 4-6 Metre Radio Wave-Length Band. *Nature*, **157**, 47–48. (Cited on page 37.)
- HIRAYAMA, T. (1974). Theoretical Model of Flares and Prominences. I: Evaporating Flare Model. *Solar Physics*, **34**, 323–338. (Cited on page 44.)
- HOLMAN, G.D. & PESSES, M.E. (1983). Solar type II radio emission and the shock drift acceleration of electrons. *Astrophysical Journal*, **267**, 837–843. (Cited on pages 81, 85 and 194.)
- HOUGH, P.V.C. (1961). A Method for Faster Analysis of Bubble Chamber Photographs (Hough and Powell). In *Instrumentation for High-Energy Physics*, 242. (Cited on page 218.)
- HOWARD, R.A., MOSES, J.D., VOURLIDAS, A., NEWMARK, J.S., SOCKER, D.G., PLUNKETT, S.P., KORENDYKE, C.M., COOK, J.W., HURLEY, A., DAVILA, J.M., THOMPSON, W.T., ST CYR, O.C., MENTZELL, E., MEHALICK, K., LEMEN, J.R., WUELTER, J.P., DUNCAN, D.W., TARBELL, T.D., WOLFSON, C.J., MOORE, A., HARRISON, R.A., WALTHAM, N.R., LANG, J., DAVIS, C.J., EYLES, C.J., MAPSON-MENARD, H., SIMNETT, G.M., HALAIN, J.P., DEFISE, J.M., MAZY, E., ROCHUS, P., MERCIER, R., RAVET, M.F., DELMOTTE, F., AUCHERE, F., DELABOUDINIÈRE, J.P., BOTHMER, V.,

## REFERENCES

---

- DEUTSCH, W., WANG, D., RICH, N., COOPER, S., STEPHENS, V., MAAHS, G., BAUGH, R., McMULLIN, D. & CARTER, T. (2008). Sun Earth Connection Coronal and Heliospheric Investigation (SECCHI). *Space Science Reviews*, **136**, 67–115. (Cited on pages 106, 108 and 109.)
- HOWARD, T.A. & TAPPIN, S.J. (2009). Interplanetary Coronal Mass Ejections Observed in the Heliosphere: 1. Review of Theory. *Space Science Reviews*, **147**, 31–54. (Cited on pages 148, 149 and 150.)
- HOWARD, T.A., FRY, C.D., JOHNSTON, J.C. & WEBB, D.F. (2007). On the Evolution of Coronal Mass Ejections in the Interplanetary Medium. *Astrophysical Journal*, **667**, 610–625. (Cited on page 141.)
- HUNDHAUSEN, A. (1999). Coronal Mass Ejections. In K.T. Strong, J.L.R. Saba, B.M. Haisch & J.T. Schmelz, eds., *The many faces of the sun: a summary of the results from NASA's Solar Maximum Mission.*, 143. (Cited on page 20.)
- HUNDHAUSEN, A.J. (1972). Coronal Expansion and Solar Wind. *Physics and Chemistry in Space*, **5**. (Cited on page 39.)
- ILLING, R.M.E. & HUNDHAUSEN, A.J. (1985). Observation of a coronal transient from 1.2 to 6 solar radii. *Journal of Geophysical Research*, **90**, 275–282. (Cited on page 21.)
- INAN, U. & GOLKOWSKI, M. (2011). *Principles of Plasma Physics for Engineers and Scientists*. (Cited on page 57.)
- JACKSON, J.D. (1975). *Classical electrodynamics*. (Cited on page 147.)
- KAHLER, S.W. (2007). Solar Sources of Heliospheric Energetic Electron Events - Shocks or Flares? *Space Science Reviews*, **129**, 359–390. (Cited on page 172.)
- KAISER, M.L., KUCERA, T.A., DAVILA, J.M., ST. CYR, O.C., GUHATHAKURTA, M. & CHRISTIAN, E. (2008). The STEREO Mission: An Introduction. *Space Science Reviews*, **136**, 5–16. (Cited on pages 20 and 106.)
- KERDRAON, A. & DELOUIS, J.M. (1997). The Nançay Radioheliograph. In G. Trottet, ed., *Coronal Physics from Radio and Space Observations*, vol. 483 of *Lecture Notes in Physics*, Berlin Springer Verlag, 192. (Cited on pages 118, 120 and 124.)

## REFERENCES

---

- KHAN, J.I. & AURASS, H. (2002). X-ray observations of a large-scale solar coronal shock wave. *Astronomy & Astrophysics*, **383**, 1018–1031. (Cited on pages 37 and 47.)
- KIM, R.S., GOPALSWAMY, N., MOON, Y.J., CHO, K.S. & YASHIRO, S. (2012). Magnetic Field Strength in the Upper Solar Corona Using White-light Shock Structures Surrounding Coronal Mass Ejections. *Astrophysical Journal*, **746**, 118. (Cited on page 50.)
- KLASSEN, A., AURASS, H., MANN, G. & THOMPSON, B.J. (2000). Catalogue of the 1997 SOHO-EIT coronal transient waves and associated type II radio burst spectra. *Astronomy & Astrophysics Supplemental*, **141**, 357–369. (Cited on pages 46 and 215.)
- KLASSEN, A., BOTHMER, V., MANN, G., REINER, M.J., KRUCKER, S., VOURLIDAS, A. & KUNOW, H. (2002). Solar energetic electron events and coronal shocks. *Astronomy & Astrophysics*, **385**, 1078–1088. (Cited on pages 44, 47 and 171.)
- KLEIN, K.L., KHAN, J.I., VILMER, N., DELOUIS, J.M. & AURASS, H. (1999). X-ray and radio evidence on the origin of a coronal shock wave. *Astronomy & Astrophysics*, **346**, L53–L56. (Cited on page 40.)
- KLIEM, B. & TÖRÖK, T. (2006). Torus Instability. *Physical Review Letters*, **96**, 255002–+. (Cited on pages 140 and 166.)
- KNOCK, S.A., CAIRNS, I.H., ROBINSON, P.A. & KUNCIC, Z. (2001). Theory of type II radio emission from the foreshock of an interplanetary shock. *Journal of Geophysical Research*, **106**, 25041–25052. (Cited on page 93.)
- KNOCK, S.A., CAIRNS, I.H., ROBINSON, P.A. & KUNCIC, Z. (2003). Theoretically predicted properties of type II radio emission from an interplanetary foreshock. *Journal of Geophysical Research (Space Physics)*, **108**, 1126. (Cited on page 93.)
- KONTAR, E.P. (2001). Dynamics of electron beams in the inhomogeneous solar corona plasma. *Solar Physics*, **202**, 131–149. (Cited on pages 87, 88 and 92.)
- KOPP, R.A. & PNEUMAN, G.W. (1976). Magnetic reconnection in the corona and the loop prominence phenomenon. *Solar Physics*, **50**, 85–98. (Cited on page 44.)

## REFERENCES

---

- KOSUGI, T. (1976). Type II-IV radio bursts and compact and diffuse white-light clouds in the outer corona of December 14, 1971. *Solar Physics*, **48**, 339–356. (Cited on page 38.)
- KOZAREV, K.A., KORRECK, K.E., LOBZIN, V.V., WEBER, M.A. & SCHWADRON, N.A. (2011). Off-limb Solar Coronal Wavefronts from SDO/AIA Extreme-ultraviolet Observations - Implications for Particle Production. *Astrophysical Journal Letters*, **733**, L25. (Cited on pages 47, 171 and 194.)
- KRALL, J. & ST. CYR, O.C. (2006). Flux-Rope Coronal Mass Ejection Geometry and Its Relation to Observed Morphology. *Astrophysical Journal*, **652**, 1740–1746. (Cited on page 158.)
- KRALL, J., CHEN, J., DUFFIN, R.T., HOWARD, R.A. & THOMPSON, B.J. (2001). Erupting Solar Magnetic Flux Ropes: Theory and Observation. *Astrophysical Journal*, **562**, 1045–1057. (Cited on pages 65, 72 and 73.)
- KRUCKER, S., LARSON, D.E., LIN, R.P. & THOMPSON, B.J. (1999). On the Origin of Impulsive Electron Events Observed at 1 AU. *Astrophysical Journal*, **519**, 864–875. (Cited on pages 44 and 47.)
- LANTOS, P. (1999). Low Frequency Observations of the Quiet Sun: a Review. In T.S. Bastian, N. Gopalswamy & K. Shibasaki, eds., *Proceedings of the Nobeyama Symposium*, 11–24. (Cited on page 17.)
- LECACHEUX, A. (2000). The Nançay Decameter Array: A Useful Step Towards Giant, New Generation Radio Telescopes for Long Wavelength Radio Astronomy. *Washington DC American Geophysical Union Geophysical Monograph Series*, **119**, 321. (Cited on page 124.)
- LEMEN, J.R., TITLE, A.M., AKIN, D.J., BOERNER, P.F., CHOU, C., DRAKE, J.F., DUNCAN, D.W., EDWARDS, C.G., FRIEDLAENDER, F.M., HEYMAN, G.F., HURLBURT, N.E., KATZ, N.L., KUSHNER, G.D., LEVAY, M., LINDGREN, R.W., MATHUR, D.P., MCFEATERS, E.L., MITCHELL, S., REHSE, R.A., SCHRIJVER, C.J., SPRINGER, L.A., STERN, R.A., TARBELL, T.D., WUELTER, J.P., WOLFSON, C.J., YANARI, C., BOOKBINDER, J.A., CHEIMETS, P.N., CALDWELL, D., DELUCA, E.E., GATES, R., GOLUB, L., PARK, S., PODGORSKI, W.A., BUSH, R.I., SCHERRER, P.H., GUMMIN, M.A., SMITH, P., AUKER, G., JERRAM, P., POOL, P., SOUFLI, R., WINDT, D.L., BEARDSLEY, S., CLAPP,

## REFERENCES

---

- M., LANG, J. & WALTHAM, N. (2012). The Atmospheric Imaging Assembly (AIA) on the Solar Dynamics Observatory (SDO). *Solar Physics*, **275**, 17–40. (Cited on pages 114, 115, 117 and 118.)
- LEVER, E.L., QUEST, K.B. & SHAPIRO, V.D. (2001). Shock surfing vs. shock drift acceleration. *Geophysical Research Letters*, **28**, 1367–1370. (Cited on page 84.)
- LEWIS, D.J. & SIMNETT, G.M. (2002). Bulk flow velocities in the solar corona at solar maximum. *Monthly Notices of the Royal Astronomical Society*, **333**, 969–976. (Cited on page 31.)
- LIN, C.H., GALLAGHER, P.T. & RAFTERY, C.L. (2010). Investigating the driving mechanisms of coronal mass ejections. *Astronomy & Astrophysics*, **516**, A44. (Cited on page 140.)
- LIN, J. & FORBES, T.G. (2000). Effects of reconnection on the coronal mass ejection process. *Journal of Geophysical Research*, **105**, 2375–2392. (Cited on pages 66, 140 and 165.)
- LIN, R.P., LEVEDAHL, W.K., LOTKO, W., GURNETT, D.A. & SCARF, F.L. (1986). Evidence for nonlinear wave-wave interactions in solar type III radio bursts. *Astrophysical Journal*, **308**, 954–965. (Cited on page 92.)
- LINDEMANN, F. (1919). Note on the Theory of Magnetic Storms. *Philosophical Magazine Series 6*, **38**, 669. (Cited on page 19.)
- LONG, D.M., DELUCA, E.E. & GALLAGHER, P.T. (2011a). The Wave Properties of Coronal Bright Fronts Observed Using SDO/AIA. *Astrophysical Journal Letters*, **741**, L21. (Cited on page 176.)
- LONG, D.M., GALLAGHER, P.T., MCATEER, R.T.J. & BLOOMFIELD, D.S. (2011b). Deceleration and dispersion of large-scale coronal bright fronts. *Astronomy & Astrophysics*, **531**, A42. (Cited on pages 46 and 171.)
- LOWE, R.E. & BURGESS, D. (2003). The properties and causes of rippling in quasi-perpendicular collisionless shock fronts. *Annales Geophysicae*, **21**, 671–679. (Cited on page 195.)
- LYNCH, B.J., ANTIOCHOS, S.K., MACNEICE, P.J., ZURBUCHEN, T.H. & FISK, L.A. (2004). Observable Properties of the Breakout Model for Coronal Mass Ejections. *Astrophysical Journal*, **617**, 589–599. (Cited on pages 70 and 71.)

## REFERENCES

---

- LYNCH, B.J., ANTIOCHOS, S.K., DEVORE, C.R., LUHMANN, J.G. & ZURBUCHEN, T.H. (2008). Topological Evolution of a Fast Magnetic Breakout CME in Three Dimensions. *Astrophysical Journal*, **683**, 1192–1206. (Cited on pages 70, 71, 140 and 165.)
- LYOT, B. (1939). The study of the solar corona and prominences without eclipses (George Darwin Lecture, 1939). *Monthly Notices of the Royal Astronomical Society*, **99**, 580. (Cited on page 101.)
- MACNEICE, P., ANTIOCHOS, S.K., PHILLIPS, A., SPICER, D.S., DEVORE, C.R. & OLSON, K. (2004). A Numerical Study of the Breakout Model for Coronal Mass Ejection Initiation. *Astrophysical Journal*, **614**, 1028–1041. (Cited on page 71.)
- MACQUEEN, R.M., CSOEKE-POECKH, A., HILDNER, E., HOUSE, L., REYNOLDS, R., STANGER, A., TEPOEL, H. & WAGNER, W. (1980). The High Altitude Observatory Coronagraph/Polarimeter on the Solar Maximum Mission. *Solar Physics*, **65**, 91–107. (Cited on page 20.)
- MAGDALENIĆ, J., MARQUÉ, C., ZHUKOV, A.N., VRŠNAK, B. & VERONIG, A. (2012). Flare-generated Type II Burst without Associated Coronal Mass Ejection. *Astrophysical Journal*, **746**, 152. (Cited on page 41.)
- MAIA, D., PICK, M., VOURLIDAS, A. & HOWARD, R. (2000). Development of Coronal Mass Ejections: Radio Shock Signatures. *Astrophysical Journal Letters*, **528**, L49–L51. (Cited on pages 38 and 39.)
- MAIA, D.J.F. & PICK, M. (2004). Revisiting the Origin of Impulsive Electron Events: Coronal Magnetic Restructuring. *Astrophysical Journal*, **609**, 1082–1097. (Cited on pages 48, 172 and 215.)
- MALONEY, S.A. & GALLAGHER, P.T. (2010). Solar Wind Drag and the Kinematics of Interplanetary Coronal Mass Ejections. *Astrophysical Journal Letters*, **724**, L127–L132. (Cited on pages 32, 141 and 166.)
- MALONEY, S.A. & GALLAGHER, P.T. (2011). STEREO Direct Imaging of a Coronal Mass Ejection-driven Shock to 0.5 AU. *Astrophysical Journal Letters*, **736**, L5. (Cited on pages 50 and 193.)

---

## REFERENCES

- MANCUSO, S. (2011). Combined Analysis of Ultraviolet and Radio Observations of the 7 May 2004 CME/Shock Event. *Solar Physics*, **273**, 511–523. (Cited on page 40.)
- MANCUSO, S. & RAYMOND, J.C. (2004). Coronal transients and metric type II radio bursts. I. Effects of geometry. *Astronomy & Astrophysics*, **413**, 363–371. (Cited on pages 40 and 41.)
- MANN, G. & CLASSEN, H.T. (1995). Electron acceleration to high energies at quasi-parallel shock waves in the solar corona. *Astronomy & Astrophysics*, **304**, 576. (Cited on pages 43 and 226.)
- MANN, G. & KLASSEN, A. (2005). Electron beams generated by shock waves in the solar corona. *Astronomy & Astrophysics*, **441**, 319–326. (Cited on pages 43, 85, 171 and 188.)
- MANN, G., CLASSEN, T. & AURASS, H. (1995). Characteristics of coronal shock waves and solar type II radio bursts. *Astronomy & Astrophysics*, **295**, 775. (Cited on page 36.)
- MANN, G., KLASSEN, A., CLASSEN, H.T., AURASS, H., SCHOLZ, D., MACDOWALL, R.J. & STONE, R.G. (1996). Catalogue of solar type II radio bursts observed from September 1990 to December 1993 and their statistical analysis. *Astronomy & Astrophysics Supplemental*, **119**, 489–498. (Cited on pages 36 and 171.)
- MANN, G., JANSEN, F., MACDOWALL, R.J., KAISER, M.L. & STONE, R.G. (1999). A heliospheric density model and type III radio bursts. *Astronomy & Astrophysics*, **348**, 614–620. (Cited on pages 166, 167 and 186.)
- MANN, G., KLASSEN, A., AURASS, H. & CLASSEN, H.T. (2003). Formation and development of shock waves in the solar corona and the near-Sun interplanetary space. *Astronomy & Astrophysics*, **400**, 329–336. (Cited on pages 75 and 76.)
- MANN, G., WARMUTH, A. & AURASS, H. (2009). Generation of highly energetic electrons at reconnection outflow shocks during solar flares. *Astronomy & Astrophysics*, **494**, 669–675. (Cited on page 44.)
- MANOHARAN, P.K. & KUNDU, M.R. (2003). Coronal Structure of a Flaring Region and Associated Coronal Mass Ejection. *Astrophysical Journal*, **592**, 597–606. (Cited on page 140.)

---

## REFERENCES

- MAXWELL, A. & THOMPSON, A.R. (1962). Spectral Observations of Solar Radio Bursts. II. Slow-Drift Bursts and Coronal Streamers. *Astrophysical Journal*, **135**, 138. (Cited on page 38.)
- MELROSE, D.B. (1986). *Instabilities in Space and Laboratory Plasmas*. Cambridge University Press. (Cited on page 90.)
- MELROSE, D.B. (1989). *Instabilities in Space and Laboratory Plasmas*. (Cited on pages 87 and 88.)
- MENZEL, D.H. (1936). The Structure of the Atmosphere of  $\zeta$  Aurigae. *Harvard College Observatory Circular*, **417**, 1–9. (Cited on page 230.)
- MERCIER, C., SUBRAMANIAN, P., KERDRAON, A., PICK, M., ANANTHAKRISHNAN, S. & JANARDHAN, P. (2006). Combining visibilities from the giant meterwave radio telescope and the Nancay radio heliograph. High dynamic range snapshot images of the solar corona at 327 MHz. *Astronomy & Astrophysics*, **447**, 1189–1201. (Cited on page 123.)
- MIERLA, M., INHESTER, B., MARQUÉ, C., RODRIGUEZ, L., GISSOT, S., ZHUKOV, A.N., BERGHMANS, D. & DAVILA, J. (2009). On 3D Reconstruction of Coronal Mass Ejections: I. Method Description and Application to SECCHI-COR Data. *Solar Physics*, **259**, 123–141. (Cited on page 22.)
- MINNAERT, M. (1930a). On the continuous spectrum of the corona and its polarisation. With 3 figures. (Received July 30, 1930). *Zeitschrift fur Astrophysik*, **1**, 209–+. (Cited on page 141.)
- MINNAERT, M. (1930b). On the continuous spectrum of the corona and its polarisation. With 3 figures. (Received July 30, 1930). *Zeitschrift fur Astrophysik*, **1**, 209. (Cited on pages 148 and 149.)
- MITALAS, R. & SILLS, K.R. (1992). On the photon diffusion time scale for the sun. *Astrophysical Journal*, **401**, 759. (Cited on page 4.)
- MITEVA, R. & MANN, G. (2007). The electron acceleration at shock waves in the solar corona. *Astronomy & Astrophysics*, **474**, 617–625. (Cited on pages 43 and 45.)

---

## REFERENCES

- MONTMERLE, T., AUGEREAU, J.C., CHAUSSIDON, M., GOUNELLE, M., MARTY, B. & MORBIDELLI, A. (2006). From Suns to Life: A Chronological Approach to the History of Life on Earth 3. Solar System Formation and Early Evolution: the First 100 Million Years. *Earth Moon and Planets*, **98**, 39–95. (Cited on page 2.)
- MOON, Y.J., CHOUE, G.S., WANG, H., PARK, Y.D., GOPALSWAMY, N., YANG, G. & YASHIRO, S. (2002). A Statistical Study of Two Classes of Coronal Mass Ejections. *Astrophysical Journal*, **581**, 694–702. (Cited on page 24.)
- MORAN, T.G. & DAVILA, J.M. (2004). Three-Dimensional Polarimetric Imaging of Coronal Mass Ejections. *Science*, **305**, 66–71. (Cited on page 22.)
- MOSES, D., CLETTE, F., DELABOUDINIÈRE, J.P., ARTZNER, G.E., BOUGNET, M., BRUNAUD, J., CARABETIAN, C., GABRIEL, A.H., HOCHEDEZ, J.F., MILLIER, F., SONG, X.Y., AU, B., DERE, K.P., HOWARD, R.A., KREPLIN, R., MICHELS, D.J., DEFISE, J.M., JAMAR, C., ROCHUS, P., CHAUVINEAU, J.P., MARIOGE, J.P., CATURA, R.C., LEMEN, J.R., SHING, L., STERN, R.A., GURMAN, J.B., NEUPERT, W.M., NEWMARK, J., THOMPSON, B., MAUCHERAT, A., PORTIER-FOZZANI, F., BERGHMANS, D., CUGNON, P., VAN DESSEL, E.L. & GABRYL, J.R. (1997). EIT Observations of the Extreme Ultraviolet Sun. *Solar Physics*, **175**, 571–599. (Cited on page 45.)
- MÜLLER-MELLIN, R., BÖTTCHER, S., FALENSKI, J., RODE, E., DUVET, L., SANDERSON, T., BUTLER, B., JOHLANDER, B. & SMIT, H. (2008). The Solar Electron and Proton Telescope for the STEREO Mission. *Space Science Reviews*, **136**, 363–389. (Cited on page 188.)
- MUNRO, R.H., GOSLING, J.T., HILDNER, E., MACQUEEN, R.M., POLAND, A.I. & ROSS, C.L. (1979). The association of coronal mass ejection transients with other forms of solar activity. *Solar Physics*, **61**, 201–215. (Cited on pages 27 and 141.)
- NELSON, G.J. & MELROSE, D.B. (1985). *Type II bursts*, 333–359. (Cited on page 36.)
- NEWKIRK, G., JR. (1961). The Solar Corona in Active Regions and the Thermal Origin of the Slowly Varying Component of Solar Radio Radiation. *Astrophysical Journal*, **133**, 983. (Cited on page 97.)

---

## REFERENCES

- NITA, G.M. & GARY, D.E. (2010). The generalized spectral kurtosis estimator. *Monthly Notices of the Royal Astronomical Society*, **406**, L60–L64. (Cited on page 138.)
- NITA, G.M., GARY, D.E., LIU, Z., HURFORD, G.J. & WHITE, S.M. (2007). Radio Frequency Interference Excision Using Spectral-Domain Statistics. *Publications of the Astronomical Society of the Pacific*, **119**, 805–827. (Cited on page 138.)
- OLMEDO, O., ZHANG, J., WECHSLER, H., POLAND, A. & BORNE, K. (2008). Automatic Detection and Tracking of Coronal Mass Ejections in Coronagraph Time Series. *Solar Physics*, **248**, 485–499. (Cited on page 201.)
- ONTIVEROS, V. & VOURLIDAS, A. (2009). Quantitative Measurements of Coronal Mass Ejection-Driven Shocks from LASCO Observations. *Astrophysical Journal*, **693**, 267–275. (Cited on page 50.)
- PARKER, E.N. (1963). The Solar-Flare Phenomenon and the Theory of Reconnection and Annihilation of Magnetic Fields. *Astrophysical Journal Supplemental Series*, **8**, 177. (Cited on page 62.)
- PAYNE-SCOTT, R., YABSLEY, D.E. & BOLTON, J.G. (1947). Relative Times of Arrival of Bursts of Solar Noise on Different Radio Frequencies. *Nature*, **160**, 256–257. (Cited on page 37.)
- PESNELL, W.D., THOMPSON, B.J. & CHAMBERLIN, P.C. (2012). The Solar Dynamics Observatory (SDO). *Solar Physics*, **275**, 3–15. (Cited on page 172.)
- PETSCHEK, H.E. (1964). Magnetic Field Annihilation. *NASA Special Publication*, **50**, 425. (Cited on page 64.)
- PHILLIPS, K.J.H. (1995). *Guide to the Sun*. (Cited on page 100.)
- PICK, M. & VILMER, N. (2008). Sixty-five years of solar radioastronomy: flares, coronal mass ejections and Sun Earth connection. *Astronomy & Astrophysics Review*, **16**, 1–153. (Cited on page 44.)
- PICK, M., FORBES, T.G., MANN, G., CANE, H.V., CHEN, J., CIARAVELLA, A., CREMADES, H., HOWARD, R.A., HUDSON, H.S., KLASSEN, A., KLEIN, K.L., LEE, M.A., LINKER,

## REFERENCES

---

- J.A., MAIA, D., MIKIC, Z., RAYMOND, J.C., REINER, M.J., SIMNETT, G.M., SRIVASTAVA, N., TRIPATHI, D., VAINIO, R., VOURLIDAS, A., ZHANG, J., ZURBUCHEN, T.H., SHEELEY, N.R. & MARQUÉ, C. (2006). Multi-Wavelength Observations of CMEs and Associated Phenomena. Report of Working Group F. *Space Science Reviews*, **123**, 341–382. (Cited on page 21.)
- POLAND, A.I., HOWARD, R.A., KOOMEN, M.J., MICHELS, D.J. & SHEELEY, N.R., JR. (1981). Coronal transients near sunspot maximum. *Solar Physics*, **69**, 169–175. (Cited on pages 27 and 141.)
- PRIEST, E. & FORBES, T. (2000). *Magnetic Reconnection*. (Cited on pages 66, 67, 68 and 79.)
- PRIEST, E.R. & FORBES, T.G. (1986). New models for fast steady state magnetic reconnection. *Journal of Geophysical Research*, **91**, 5579–5588. (Cited on page 65.)
- RATCLIFFE, H., BIAN, N.H. & KONTAR, E.P. (2012). Density Fluctuations and the Acceleration of Electrons by Beam-generated Langmuir Waves in the Solar Corona. *Astrophysical Journal*, **761**, 176. (Cited on pages 88 and 92.)
- REID, H.A.S. & KONTAR, E.P. (2010). Solar Wind Density Turbulence and Solar Flare Electron Transport from the Sun to the Earth. *Astrophysical Journal*, **721**, 864–874. (Cited on pages 88 and 92.)
- REINER, M.J., KAISER, M.L., GOPALSWAMY, N., AURASS, H., MANN, G., VOURLIDAS, A. & MAKSIMOVIC, M. (2001). Statistical analysis of coronal shock dynamics implied by radio and white-light observations. *Journal of Geophysical Research*, **106**, 25279–25290. (Cited on pages 40 and 41.)
- RICHARDSON, I.G. (2013). Astrophysics: An unexpected shock. *Nature Physics*, **9**, 131–132. (Cited on page 83.)
- ROBBRECHT, E. & BERGHMANS, D. (2004). Automated recognition of coronal mass ejections (CMEs) in near-real-time data. *Astronomy & Astrophysics*, **425**, 1097–1106. (Cited on page 201.)
- ROBINSON, P.A. & CAIRNS, I.H. (1993). Stochastic Growth Theory of Type III Solar Radio Emission. *Astrophysical Journal*, **418**, 506. (Cited on pages 92, 93 and 229.)

## REFERENCES

---

- ROBINSON, P.A. & CAIRNS, I.H. (1998). Fundamental and Harmonic Emission in Type III Solar Radio Bursts - II. Dominant Modes and Dynamic Spectra. *Solar Physics*, **181**, 395–428. (Cited on pages 93 and 229.)
- ROBINSON, P.A., WILLES, A.J. & CAIRNS, I.H. (1993). Dynamics of Langmuir and ion-sound waves in type III solar radio sources. *Astrophysical Journal*, **408**, 720–734. (Cited on page 89.)
- ROBINSON, P.A., CAIRNS, I.H. & WILLES, A.J. (1994). Dynamics and efficiency of type III solar radio emission. *Astrophysical Journal*, **422**, 870–882. (Cited on pages 89, 90 and 91.)
- ROBINSON, R.D. & STEWART, R.T. (1985). A positional comparison between coronal mass ejection events and solar type II bursts. *Solar Physics*, **97**, 145–157. (Cited on page 39.)
- RUSSELL, C.T. & MULLIGAN, T. (2002). On the magnetosheath thicknesses of interplanetary coronal mass ejections. *Planet. Space Sci.*, **50**, 527–534. (Cited on page 50.)
- RUST, D.M. (1972). Flares and Changing Magnetic Fields. *Solar Physics*, **25**, 141–157. (Cited on page 66.)
- SACKMANN, I.J., BOOTHROYD, A.I. & KRAEMER, K.E. (1993). Our Sun. III. Present and Future. *Astrophysical Journal*, **418**, 457. (Cited on page 3.)
- SAITO, K., POLAND, A.I. & MUNRO, R.H. (1977). A study of the background corona near solar minimum. *Solar Physics*, **55**, 121–134. (Cited on page 97.)
- SCHERRER, P.H., SCHOU, J., BUSH, R.I., KOSOVICHEV, A.G., BOGART, R.S., HOEKSEMA, J.T., LIU, Y., DUVALL, T.L., ZHAO, J., TITLE, A.M., SCHRIJVER, C.J., TARBELL, T.D. & TOMCZYK, S. (2012). The Helioseismic and Magnetic Imager (HMI) Investigation for the Solar Dynamics Observatory (SDO). *Solar Physics*, **275**, 207–227. (Cited on pages 179 and 180.)
- SCHMIDT, J.M. & CAIRNS, I.H. (2012a). Type II radio bursts: 1. New entirely analytic formalism for the electron beams, Langmuir waves, and radio emission. *Journal of Geophysical Research (Space Physics)*, **117**, 4106. (Cited on pages 93, 191 and 196.)

## REFERENCES

---

- SCHMIDT, J.M. & CAIRNS, I.H. (2012b). Type II radio bursts: 2. Application of the new analytic formalism. *Journal of Geophysical Research (Space Physics)*, **117**, 11104. (Cited on pages 85, 93 and 94.)
- SCHRIJVER, C.J. & DE ROSA, M.L. (2003). Photospheric and heliospheric magnetic fields. *Solar Physics*, **212**, 165–200. (Cited on pages 179 and 180.)
- SCHRIJVER, C.J. & ZWAAN, C. (2008). *Solar and Stellar Magnetic Activity*. (Cited on page 11.)
- SCHRIJVER, C.J., ELMORE, C., KLIEM, B., TÖRÖK, T. & TITLE, A.M. (2008a). Observations and Modeling of the Early Acceleration Phase of Erupting Filaments Involved in Coronal Mass Ejections. *Astrophysical Journal*, **674**, 586–595. (Cited on pages 65 and 74.)
- SCHRIJVER, C.J., ELMORE, C., KLIEM, B., TÖRÖK, T. & TITLE, A.M. (2008b). Observations and Modeling of the Early Acceleration Phase of Erupting Filaments Involved in Coronal Mass Ejections. *Astrophysical Journal*, **674**, 586–595. (Cited on page 140.)
- SCHUSTER, A. (1879). on the polarisation of the Solar Corona. *Monthly Notices of the Royal Astronomical Society*, **40**, 35. (Cited on page 148.)
- SHEELEY, N.R., WALTERS, J.H., WANG, Y.M. & HOWARD, R.A. (1999). Continuous tracking of coronal outflows: Two kinds of coronal mass ejections. *Journal of Geophysical Research*, **104**, 24739–24768. (Cited on page 24.)
- SHEELEY, N.R., JR., MICHELS, D.J., HOWARD, R.A. & KOOMEN, M.J. (1980). Initial observations with the SOLWIND coronagraph. *Astrophysical Journal Letters*, **237**, L99–L101. (Cited on page 20.)
- SHEELEY, N.R., JR., WANG, Y.M., HAWLEY, S.H., BRUECKNER, G.E., DERE, K.P., HOWARD, R.A., KOOMEN, M.J., KORENDYKE, C.M., MICHELS, D.J., PASWATERS, S.E., SOCKER, D.G., ST. CYR, O.C., WANG, D., LAMY, P.L., LLEBARIA, A., SCHWENN, R., SIMNETT, G.M., PLUNKETT, S. & BIESECKER, D.A. (1997). Measurements of Flow Speeds in the Corona between 2 and 30 R sub sun. *Astrophysical Journal*, **484**, 472. (Cited on pages 32 and 73.)

## REFERENCES

---

- SONNERUP, B.U.Ö. (1970). Magnetic-field re-connexion in a highly conducting incompressible fluid. *Journal of Plasma Physics*, **4**, 161. (Cited on page 65.)
- SPITZER, L. (1962). *Physics of Fully Ionized Gases*. (Cited on page 61.)
- SPREITER, J.R., SUMMERS, A.L. & ALKSNE, A.Y. (1966). Hydromagnetic flow around the magnetosphere. *Planet. Space Sci.*, **14**, 223. (Cited on page 50.)
- STEELE, C.D.C., HOOD, A.W., PRIEST, E.R. & AMARI, T. (1989). Non-equilibrium of a cylindrical magnetic arcade. *Solar Physics*, **123**, 127–141. (Cited on page 69.)
- STERLING, A.C. & HUDSON, H.S. (1997). YOHKOH SXT Observations of X-Ray "Dimming" Associated with a Halo Coronal Mass Ejection. *Astrophysical Journal Letters*, **491**, L55. (Cited on page 211.)
- STEWART, R.T. & MAGUN, A. (1980). Radio evidence for electron acceleration by transverse shock waves in herringbone Type II solar bursts. *Proceedings of the Astronomical Society of Australia*, **4**, 53–55. (Cited on pages 44, 191 and 194.)
- STEWART, R.T. & MCLEAN, D.J. (1982). Correcting low-frequency solar radio source positions for ionospheric refraction. *Proceedings of the Astronomical Society of Australia*, **4**, 386–389. (Cited on page 176.)
- STEWART, R.T., McCABE, M.K., KOOMEN, M.J., HANSEN, R.T. & DULK, G.A. (1974). Observations of Coronal Disturbances from 1 to 9 R<sub>sun</sub>. I: First Event of 1973, January 11. *Solar Physics*, **36**, 203–217. (Cited on page 39.)
- STONE, R.G., BOUGERET, J.L., CALDWELL, J., CANU, P., DE CONCHY, Y., CORNILLEAU-WEHRLIN, N., DESCH, M.D., FAINBERG, J., GOETZ, K. & GOLDSTEIN, M.L. (1992). The Unified Radio and Plasma wave investigation. *Astronomy & Astrophysics Supplemental*, **92**, 291–316. (Cited on page 126.)
- STURROCK, P.A. (1964). Type III Solar Radio Bursts. *NASA Special Publication*, **50**, 357. (Cited on page 92.)
- STURROCK, P.A. (1966). Model of the High-Energy Phase of Solar Flares. *Nature*, **211**, 695–697. (Cited on page 44.)

## REFERENCES

---

- SURROCK, P.A. (1991). Maximum energy of semi-infinite magnetic field configurations. *Astrophysical Journal*, **380**, 655–659. (Cited on page 70.)
- SU, Y., VERONIG, A.M., HOLMAN, G.D., DENNIS, B.R., WANG, T., TEMMER, M. & GAN, W. (2013). Imaging coronal magnetic-field reconnection in a solar flare. *Nature Physics*, **9**, 489–493. (Cited on page 65.)
- SUBRAMANIAN, P. & VOURLIDAS, A. (2007). Energetics of solar coronal mass ejections. *Astronomy & Astrophysics*, **467**, 685–693. (Cited on page 30.)
- SWEET, P.A. (1958). The Neutral Point Theory of Solar Flares. In B. Lehnert, ed., *Electromagnetic Phenomena in Cosmical Physics*, vol. 6 of *IAU Symposium*, 123. (Cited on page 62.)
- TEMMER, M., VERONIG, A.M., KONTAR, E.P., KRUCKER, S. & VRŠNAK, B. (2010). Combined STEREO/RHESSI Study of Coronal Mass Ejection Acceleration and Particle Acceleration in Solar Flares. *Astrophysical Journal*, **712**, 1410–1420. (Cited on page 25.)
- THE RADIOHELIOGRAPH GROUP (1993). The Nançay multifrequency radioheliograph: New developments and data acquisition for the solar physics community. *Advances in Space Research*, **13**, 411–414. (Cited on page 120.)
- THEJAPPA, G. & MACDOWALL, R.J. (1998). Evidence for Strong and Weak Turbulence Processes in the Source Region of a Local Type III Radio Burst. *Astrophysical Journal*, **498**, 465. (Cited on page 92.)
- THERNISIEN, A.F.R., HOWARD, R.A. & VOURLIDAS, A. (2006). Modeling of Flux Rope Coronal Mass Ejections. *Astrophysical Journal*, **652**, 763–773. (Cited on page 22.)
- THOMPSON, B.J. & MYERS, D.C. (2009). A Catalog of Coronal "EIT Wave" Transients. *Astrophysical Journal Supplemental Series*, **183**, 225–243. (Cited on page 46.)
- THOMPSON, B.J., PLUNKETT, S.P., GURMAN, J.B., NEWMARK, J.S., ST. CYR, O.C. & MICHELS, D.J. (1998). SOHO/EIT observations of an Earth-directed coronal mass ejection on May 12, 1997. *Geophysical Research Letters*, **25**, 2465–2468. (Cited on pages 45 and 46.)

## REFERENCES

---

- THOMPSON, M.J., CHRISTENSEN-DALSGAARD, J., MIESCH, M.S. & TOOMRE, J. (2003). The Internal Rotation of the Sun. *Annual Review of Astronomy & Astrophysics*, **41**, 599–643. (Cited on page 7.)
- THOMPSON, W.T. & REGINALD, N.L. (2008). The Radiometric and Pointing Calibration of SECCHI COR1 on STEREO. *Solar Physics*, **250**, 443–454. (Cited on pages 108 and 113.)
- TOPTYGIN, I.N. (1980). Acceleration of particles by shocks in a cosmic plasma. *Space Science Reviews*, **26**, 157–213. (Cited on page 84.)
- TOUSEY, R. (1973). The solar corona. In M. J. Rycroft & S. K. Runcorn, ed., *Space Research XIII*, Vol. 2, p. 713 - 730, 713–730. (Cited on page 20.)
- TURCK-CHIÈZE, S. & COUVIDAT, S. (2011). Solar neutrinos, helioseismology and the solar internal dynamics. *Reports on Progress in Physics*, **74**, 086901. (Cited on pages 4, 5 and 6.)
- UCHIDA, Y. (1960). On the Exciters of Type II and Type III Solar Radio Bursts. *Publications of the Astronomical Society of Japan*, **12**, 376. (Cited on page 37.)
- UCHIDA, Y. (1974). Behavior of the flare produced coronal MHD wavefront and the occurrence of type II radio bursts. *Solar Physics*, **39**, 431–449. (Cited on page 38.)
- VAN DE HULST, H.C. (1950). The electron density of the solar corona. *Bulletin of the Astronomical Institutes of the Netherlands*, **11**, 135. (Cited on pages 141, 149, 177 and 231.)
- VAN HAARLEM, M.P., WISE, M.W., GUNST, A.W., HEALD, G., MCKEAN, J.P., HESSELS, J.W.T., DE BRUYN, A.G., NIJBOER, R., SWINBANK, J., FALLOWS, R., BRENTJENS, M., NELLES, A., BECK, R., FALCKE, H., FENDER, R., HÖRANDEL, J., KOOPMANS, L.V.E., MANN, G., MILEY, G., RÖTTGERING, H., STAPPERS, B.W., WIJERS, R.A.M.J., ZAROUBI, S., VAN DEN AKKER, M., ALEXOV, A., ANDERSON, J., ANDERSON, K., VAN ARDENNE, A., ARTS, M., ASGEKAR, A., AVRUCH, I.M., BATEJAT, F., BÄHREN, L., BELL, M.E., BELL, M.R., VAN BEMMEL, I., BENNEMA, P., BENTUM, M.J., BERNARDI, G., BEST, P., BÎRZAN, L., BONAFEDE, A., BOONSTRA, A.J., BRAUN, R., BREGMAN, J., BREITLING, F., VAN DE BRINK, R.H., BRODERICK, J., BROEKEMA, P.C., BROUW, W.N., BRÜGGEN, M., BUTCHER, H.R., VAN CAPPELLEN, W., CIARDI, B., COENEN, T., CONWAY, J., COOLEN, A., CORSTANJE, A., DAMSTRA, S., DAVIES, O., DELLER,

---

## REFERENCES

A.T., DETTMAR, R.J., VAN DIEPEN, G., DIJKSTRA, K., DONKER, P., DOORDUIN, A., DROMER, J., DROST, M., VAN DUIN, A., EISLÖFFEL, J., VAN ENST, J., FERRARI, C., FRIESWIJK, W., GANKEMA, H., GARRETT, M.A., DE GASPARIN, F., GERBERS, M., DE GEUS, E., GRIESSMEIER, J.M., GRIT, T., GRUPPEN, P., HAMAKER, J.P., HASSALL, T., HOEFT, M., HOLTIES, H.A., HORNEFFER, A., VAN DER HORST, A., VAN HOUWELINGEN, A., HUIJGEN, A., IACOBELLI, M., INTEMA, H., JACKSON, N., JELIC, V., DE JONG, A., KANT, D., KARASTERGIOU, A., KOERS, A., KOLLEN, H., KONDRATIEV, V.I., KOOISTRA, E., KOOPMAN, Y., KOSTER, A., KUNIYOSHI, M., KRAMER, M., KUPER, G., LAMBROPOULOS, P., LAW, C., VAN LEEUWEN, J., LEMAITRE, J., LOOSE, M., MAAT, P., MACARIO, G., MARKOFF, S., MASTERS, J., MCFADDEN, R.A., MCKAY-BUKOWSKI, D., MEIJERING, H., MEULMAN, H., MEVIUS, M., MILLENAAR, R., MILLER-JONES, J.C.A., MOHAN, R.N., MOL, J.D., MORAWIETZ, J., MORGANTI, R., MULCAHY, D.D., MULDER, E., MUNK, H., NIEUWENHUIS, L., VAN NIEUWPOORT, R., NOORDAM, J.E., NORDEN, M., NOUTSOS, A., OFFRINGA, A.R., OLOFSSON, H., OMAR, A., ORRÚ, E., OVEREEM, R., PAAS, H., PANDEY-POMMIER, M., PANDEY, V.N., PIZZO, R., POLATIDIS, A., RAFERTY, D., RAWLINGS, S., REICH, W., DE REIJER, J.P., REITSMA, J., RENTING, G.A., RIEMERS, P., ROL, E., ROMEIN, J.W., ROOSJEN, J., RUITER, M., SCAIFE, A., VAN DER SCHAAF, K., SCHEERS, B., SCHELLART, P., SCHOENMAKERS, A., SCHOONDERBEEK, G., SERYLAK, M., SHULEVSKI, A., SLUMAN, J., SMIRNOV, O., SOBEY, C., SPREEUW, H., STEINMETZ, M., STERKS, C.G.M., STIEPEL, H.J., STUURWOLD, K., TAGGER, M., TANG, Y., TASSE, C., THOMAS, I., THOUDAM, S., TORIBIO, M.C., VAN DER TOL, B., USOV, O., VAN VEELEN, M., VAN DER VEEN, A.J., TER VEEEN, S., VERBIEST, J.P.W., VERMEULEN, R., VERMAAS, N., VOCKS, C., VOGT, C., DE VOS, M., VAN DER WAL, E., VAN WEEREN, R., WEGGEMANS, H., WELTEVREDE, P., WHITE, S., WIJNHOLDS, S.J., WILHELMSSON, T., WUCKNITZ, O., YATAWATTA, S., ZARKA, P., ZENSUS, A. & VAN ZWieten, J. (2013). LOFAR: The LOw-Frequency ARray. *Astronomy & Astrophysics*, **556**, A2. (Cited on page 197.)

VANDAS, M. & KARLICKÝ, M. (2011). Electron acceleration in a wavy shock front. *Astronomy & Astrophysics*, **531**, A55. (Cited on pages 43 and 195.)

VEDENOV, A.A. (1963). Quasi-Linear Equations for Quantized Plasma. *Soviet Physics Doklady*, **7**, 1008. (Cited on pages 85 and 87.)

## REFERENCES

---

- VERNAZZA, J.E., AVRETT, E.H. & LOESER, R. (1981). Structure of the solar chromosphere. III - Models of the EUV brightness components of the quiet-sun. *Astrophysical Journal Supplemental Series*, **45**, 635–725. (Cited on pages 12, 13 and 14.)
- VERONIG, A.M., MUHR, N., KIENREICH, I.W., TEMMER, M. & VRŠNAK, B. (2010). First Observations of a Dome-shaped Large-scale Coronal Extreme-ultraviolet Wave. *Astrophysical Journal Letters*, **716**, L57–L62. (Cited on page 46.)
- VILMER, N., KRUCKER, S., LIN, R.P. & RHESSI TEAM (2002). Hard x-ray and Metric/Decimetric Radio Observations of the 20 February 2002 Solar Flare. *Solar Physics*, **210**, 261–272. (Cited on page 44.)
- VOURLIDAS, A. & BEMPORAD, A. (2012). A decade of coronagraphic and spectroscopic studies of CME-driven shocks. In J. Heerikhuisen, G. Li, N. Pogorelov & G. Zank, eds., *American Institute of Physics Conference Series*, vol. 1436 of *American Institute of Physics Conference Series*, 279–284. (Cited on pages 49 and 193.)
- VOURLIDAS, A., SUBRAMANIAN, P., DERE, K.P. & HOWARD, R.A. (2000). Large-Angle Spectrometric Coronagraph Measurements of the Energetics of Coronal Mass Ejections. *Astrophysical Journal*, **534**, 456–467. (Cited on pages 28, 29, 141, 153, 154, 164, 168 and 200.)
- VOURLIDAS, A., BUZASI, D., HOWARD, R.A. & ESFANDIARI, E. (2002). Mass and energy properties of LASCO CMEs. In A. Wilson, ed., *Solar Variability: From Core to Outer Frontiers*, vol. 506 of *ESA Special Publication*, 91–94. (Cited on pages 27 and 141.)
- VOURLIDAS, A., WU, S.T., WANG, A.H., SUBRAMANIAN, P. & HOWARD, R.A. (2003). Direct Detection of a Coronal Mass Ejection-Associated Shock in Large Angle and Spectrometric Coronagraph Experiment White-Light Images. *Astrophysical Journal*, **598**, 1392–1402. (Cited on page 50.)
- VOURLIDAS, A., HOWARD, R.A., ESFANDIARI, E., PATSOURAKOS, S., YASHIRO, S. & MICHALEK, G. (2010). Comprehensive Analysis of Coronal Mass Ejection Mass and Energy Properties Over a Full Solar Cycle. *Astrophysical Journal*, **722**, 1522–1538. (Cited on pages 19, 27, 30, 31, 141, 159, 162, 164 and 168.)

---

## REFERENCES

- VOURLIDAS, A., LYNCH, B.J., HOWARD, R.A. & LI, Y. (2013). How Many CMEs Have Flux Ropes? Deciphering the Signatures of Shocks, Flux Ropes, and Prominences in Coronagraph Observations of CMEs. *Solar Physics*, **284**, 179–201. (Cited on pages 49 and 50.)
- VRŠNAK, B. (2006). Forces governing coronal mass ejections. *Advances in Space Research*, **38**, 431–440. (Cited on pages 32, 33 and 167.)
- VRŠNAK, B. & CLIVER, E.W. (2008). Origin of Coronal Shock Waves. Invited Review. *Solar Physics*, **253**, 215–235. (Cited on pages 41 and 171.)
- VRŠNAK, B. & LULIĆ, S. (2000a). Formation Of Coronal Mhd Shock Waves - I. The Basic Mechanism. *Solar Physics*, **196**, 157–180. (Cited on page 41.)
- VRŠNAK, B. & LULIĆ, S. (2000b). Formation of coronal MHD shock waves - II. The Pressure Pulse Mechanism. *Solar Physics*, **196**, 181–197. (Cited on page 41.)
- VRŠNAK, B., MAGDALENIĆ, J. & AURASS, H. (2001). Comparative Analysis of Type ii Bursts and of Thermal and non-Thermal Flare Signatures. *Solar Physics*, **202**, 319–335. (Cited on page 41.)
- VRŠNAK, B., MAGDALENIĆ, J., TEMMER, M., VERONIG, A., WARMUTH, A., MANN, G., AURASS, H. & OTRUBA, W. (2005a). Broadband Metric-Range Radio Emission Associated with a Moreton/EIT Wave. *Astrophysical Journal Letters*, **625**, L67–L70. (Cited on page 215.)
- VRŠNAK, B., SUDAR, D. & RUŽDJAK, D. (2005b). The CME-flare relationship: Are there really two types of CMEs? *Astronomy & Astrophysics*, **435**, 1149–1157. (Cited on pages 24, 46 and 172.)
- VRŠNAK, B., MARIČIĆ, D., STANGER, A.L., VERONIG, A.M., TEMMER, M. & ROŠA, D. (2007). Acceleration Phase of Coronal Mass Ejections: I. Temporal and Spatial Scales. *Solar Physics*, **241**, 85–98. (Cited on page 25.)
- WAKKER, B.P. & SCHWARZ, U.J. (1988). The Multi-Resolution CLEAN and its application to the short-spacing problem in interferometry. *Astronomy & Astrophysics*, **200**, 312–322. (Cited on page 123.)

## REFERENCES

---

- WANG, Y.M. (2000). EIT Waves and Fast-Mode Propagation in the Solar Corona. *Astrophysical Journal Letters*, **543**, L89–L93. (Cited on pages 46 and 171.)
- WARMUTH, A. & MANN, G. (2005). A model of the Alfvén speed in the solar corona. *Astronomy & Astrophysics*, **435**, 1123–1135. (Cited on pages 76 and 181.)
- WARMUTH, A., VRŠNAK, B., MAGDALENIĆ, J., HANSLMEIER, A. & OTRUBA, W. (2004). A multiwavelength study of solar flare waves. II. Perturbation characteristics and physical interpretation. *Astronomy & Astrophysics*, **418**, 1117–1129. (Cited on pages 46, 172 and 194.)
- WEBB, D.F. & HOWARD, T.A. (2012). Coronal Mass Ejections: Observations. *Living Reviews in Solar Physics*, **9**, 3. (Cited on page 23.)
- WEBB, D.F. & HUNDHAUSEN, A.J. (1987). Activity associated with the solar origin of coronal mass ejections. *Solar Physics*, **108**, 383–401. (Cited on page 21.)
- WILD, J.P. (1950). Observations of the Spectrum of High-Intensity Solar Radiation at Metre Wavelengths. III. Isolated Bursts. *Australian Journal of Scientific Research A Physical Sciences*, **3**, 541. (Cited on page 171.)
- WILD, J.P. (1964). Radio Observations of Solar Flares. *NASA Special Publication*, **50**, 161. (Cited on page 44.)
- WILD, J.P., MURRAY, J.D. & ROWE, W.C. (1954). Harmonics in the Spectra of Solar Radio Disturbances. *Australian Journal of Physics*, **7**, 439. (Cited on page 37.)
- WILD, J.P., SHERIDAN, K.V. & TRENT, G.H. (1959). The transverse motions of the sources of solar radio bursts. In R.N. Bracewell, ed., *URSI Symp. 1: Paris Symposium on Radio Astronomy*, vol. 9 of *IAU Symposium*, 176. (Cited on page 19.)
- WILD, J.P., SMERD, S.F. & WEISS, A.A. (1963). Solar Bursts. *Annual Review of Astronomy & Astrophysics*, **1**, 291. (Cited on page 20.)
- WOLFSON, R. & SARAN, S. (1998). Energetics of Coronal Mass Ejections: Role of the Streamer Cavity. *Astrophysical Journal*, **499**, 496. (Cited on page 65.)

## REFERENCES

---

- WU, C.S. (1984). A fast Fermi process - Energetic electrons accelerated by a nearly perpendicular bow shock. *Journal of Geophysical Research*, **89**, 8857–8862. (Cited on pages 85 and 194.)
- YASHIRO, S., GOPALSWAMY, N., MICHALEK, G., ST. CYR, O.C., PLUNKETT, S.P., RICH, N.B. & HOWARD, R.A. (2004). A catalog of white light coronal mass ejections observed by the SOHO spacecraft. *Journal of Geophysical Research (Space Physics)*, **109**, 7105. (Cited on pages 22 and 23.)
- YURCHYSHYN, V., YASHIRO, S., ABRAMENKO, V., WANG, H. & GOPALSWAMY, N. (2005). Statistical Distributions of Speeds of Coronal Mass Ejections. *Astrophysical Journal*, **619**, 599–603. (Cited on pages 23 and 24.)
- ZHANG, J. & DERE, K.P. (2006). A Statistical Study of Main and Residual Accelerations of Coronal Mass Ejections. *Astrophysical Journal*, **649**, 1100–1109. (Cited on pages 24, 26 and 33.)
- ZHANG, J., DERE, K.P., HOWARD, R.A., KUNDU, M.R. & WHITE, S.M. (2001). On the Temporal Relationship between Coronal Mass Ejections and Flares. *Astrophysical Journal*, **559**, 452–462. (Cited on pages 25, 27, 165 and 168.)
- ZHANG, J., DERE, K.P., HOWARD, R.A. & VOURLIDAS, A. (2004). A Study of the Kinematic Evolution of Coronal Mass Ejections. *Astrophysical Journal*, **604**, 420–432. (Cited on pages 25, 165 and 168.)
- ZHUKOV, A.N., RODRIGUEZ, L. & DE PATOUL, J. (2009). STEREO/SECCHI Observations on 8 December 2007: Evidence Against the Wave Hypothesis of the EIT Wave Origin. *Solar Physics*, **259**, 73–85. (Cited on page 172.)
- ZLOBEC, P., MESSEROTTI, M., KARLICKY, M. & URBARZ, H. (1993). Fine structures in time profiles of type II bursts at frequencies above 200 MHz. *Solar Physics*, **144**, 373–384. (Cited on pages 43, 171, 195 and 196.)
- ZUCCA, P., CARLEY, E.P., McCUALEY, J., GALLAGHER, P.T., MONSTEIN, C. & McA-TEER, R.T.J. (2012). Observations of Low Frequency Solar Radio Bursts from the Rosse

---

## REFERENCES

Solar-Terrestrial Observatory. *Solar Physics*, **280**, 591–602. (Cited on pages 128, 133, 134, 135 and 137.)